The Impact Dynamics of Weakly Charged Droplets

Fan Gao

Dissertation submitted to the faculty of the Virginia Polytechnic Institute and State University in partial fulfillment of the requirements for the degree of

Doctor of Philosophy
In
Mechanical Engineering

Rui Qiao Co-Chair
Weiwei Deng Co-Chair
Mark R. Paul
Danesh K. Tafti
Cheng Chen

July 8th, 2019
Blacksburg, VA

Keywords: Droplet and bubble, Lubrication pressure, Maxwell stress, Impact

The Impact Dynamics of Weakly Charged Droplets

Fan Gao

ABSTRACT

Electric charges are often found in naturally or artificially formed droplets, such as raindrops and those generated by Kelvin's water dropper. In contrast to the impact of neutral droplets on a flat solid surface upon which a thin convex lens shape layer of the gas film is typically formed, I show that the delicate gas thin film can be fundamentally altered for even weakly charged droplets both experimentally and numerically. As the charge level is raised above a critical level of about 1% of the Rayleigh limit for representative impact conditions, the Maxwell stress overcomes the gas pressure buildup to deform the droplet bottom surface. A conical liquid tip forms and pierces through the gas film, leading to a circular contact line moving outwards that does not trap any gas. The critical charge level only depends on the capillary number based on the gas viscosity. The deformation applies to common liquids and molten alloy droplets. Even dielectric surfaces can also induce conical deformation. The charged droplets can also deform upon hydrophobic surfaces, and increase the contact time on hydrophobic surfaces or even avoid bouncing.

The Impact Dynamics of Weakly Charged Droplets

Fan Gao

GENERAL AUDIENCE ABSTRACT

Electric charges are often found in naturally or artificially formed droplets, such as raindrops, waterfall, and inkjet printer. Neutral droplets impact on flat surfaces will usually trap a bubble inside because of the viscosity of air. The air bubble entrapped can be ignored if the droplet is water because the air bubble will eventually pinch-off. However, if the droplet is metal or some other viscous liquid, the air bubble will stay inside the liquid. This entrapped air bubble is undesired under some circumstances. For example, the existance of air bubble during metal 3D printing can influence the physical property. I show that the delicate gas thin film can be fundamentally altered for even weakly charged droplets both experimentally and numerically. As the charge level is raised above a critical level of about 1% of the maximum charges a droplet can carry for representative impact conditions, the electric stress will dominate the deformation of droplet. A conical liquid tip forms at the droplet bottom, avoiding the entrapment of air bubble. The critical charge level is experimentally proved to be only dependent on the gas viscosity and impact velocity. The deformation applies to common liquids and molten alloy droplets. Even dielectric surfaces can also induce conical deformation. The charged droplets can also deform upon hydrophobic surfaces, and increase the contact time on hydrophobic surfaces or even avoid bouncing.

Acknowledgments

First, I would like to express my deepest gratitude to my advisor Dr. Rui Qiao. Without his kind support and warm encouragement, I do not think I will be able to finish my Ph.D. study. His profound knowledge, sharp mind, and broad vision inspired me deeply.

I want to express my sincere gratitude to my previous advisor Dr. Weiwei Deng. His continued mentorship and guidance made this dissertation possible. His passion for research and creative mind inspired me profoundly. He also has a kind heart. I feel blessed to be a student of Dr. Deng.

I also want to thank my committee members: Dr. Mark Paul, Dr. Danesh Tafti, and Dr. Cheng Chen for their guidance, support, and encouragement during the course of this research.

Thanks to all my previous and current lab-mates and colleagues for their help and comradery: Ting Yang, Liurui Li, Fan Gao, Dr. Yuanyuan Jiang, and the list goes on.

Last but not least, I would like to express my sincerest gratitude to my parents, Xinjiang Gao and Weiqiao Ye, and my girlfriend, Mengyun Li. Without their support and love, I could not keep moving forward with gratitude and love in all these years.

Table of Contents

List of Figures

List of Tables

Chapter 1 Introduction

1.1 Background of Droplet Impact

The impact of droplets on a solid substrate is a ubiquitous and intriguing phenomenon that is very familiar to everyone in daily life, such as raindrop or pesticide application. In this section, the background of droplet impact is reviewed briefly.

1.1.1 History of Researches on Droplet Impact

Droplet impact has raised many scientists' interests. Back to 140 years ago, Worthington[1] was the first scientist to start the research of droplet impact. Due to the limitation of technology, he could only sketch his experiments results observed by naked eye observation. His sketches of droplet impact show clearly about the splash pattern after water droplet impact on a smooth solid surface. After that, the understanding of droplet impact was barely improved until the recent 60 years due to lack of time-resolved methods to slow down the millisecond impact process. Until the development of high-speed video technology and increased computational power and numerical algorithms, people finally can better, and deeper understand the droplet impact process. A high-speed camera was used for time-resolved observation of this interesting phenomenon by Thoroddsen et al.[2]. The improvements of the sensor enable the study of droplet impact with ever finer details, which took the researches into a new level. A large number of researchers has focused their research on high-speed imaging of drops and bubbles, such as droplet coalescence[3], droplet splash on the dry surface[4], crown breakup[5], bubble pinch-off[6, 7]. Besides droplet impact solid surface, the liquid surface is another topic that triggered many academic ideas[8]. This imaging technology is currently reaching the diffraction limit in the spatial resolution that is about

several hundred nanometers and up to million FPS (Frame Per Second) [9, 10]. These experimental results have been analyzed and verified using numerical tools. Many numerical simulation algorithms have been developed. There are two kinds of modeling methods, one of them is resolved simulations in the axisymmetric configuration[10], while the other is fully three-dimensional (3D) cases[11]. Comparing the numerical simulations and experimental results, scientists have achieved a deeper physical understanding of the whole droplet impact process both before and after the droplet touches substrate. A few reviews related to droplet impact have been concluded[12-14].

The whole droplet impact process often only takes about several hundred milliseconds, but the dynamics behind this short time is complicated. Generally speaking, a droplet impact process can be divided into six different stages, i.e., droplet deformation, spreading, splashing, retracting, jetting, and rebounding. Each of these stages has been studied and analyzed extensively. In the next section, details of these research are reviewed.

1.1.2 Overview of Droplet Impact Process

Based on the previous researches about droplet impact both on the solid and liquid surface, we have already known a lot about the physical phenomena and theory behind them.

For droplet's impact on a solid surface under the atmospheric conditions, experiments[15] show that a drop impacting perpendicularly to a wall will usually trap an air bubble under its center unless when the impact velocity is relatively low. At the early stage of droplet impact on a flat and smooth solid surface, the air lubrication pressure underneath the droplet increases rapidly as the thin layer of air is being squeezed out before the droplet wets the surface. The gas viscosity of the

thin air layer below the droplet causes the air lubrication pressure. For small separation distance, the lubrication pressure in the air layer will be strong enough to overcome the droplet surface. This buildup of air pressure flattens or even dents the droplet, forming a non-equilibrium convex lens shaped air film that involves multiple length scales. This deformation would transform droplet wetting from a point contact into a ring, with a thin disk of air entrapped. The initial average thickness of the air disk in the range of 2-5μm[14, 16, 17]. The air film would retract rapidly into a thicker air layer, and then contract into a toroid later. The contraction speed can be modeled with capillary-inertial dynamics, resulting in an expression for the disc radius versus time, which is in agreement with experimental results.

$$R = R_0 e^{-C\sqrt{\pi\sigma/\rho\Omega_b}t} \qquad \text{Eq.1-1}$$

where C is about 0.94, σ is the surface tension and Ω_b is the bubble volume, R_0 is the initial radius of air film, ρ is the density of droplet, t is the time, and R is the radius of air film.

Finally, a pinch-off of the toroid shape air layer would result in a bubble in the droplet. The evolution of air film into an air bubble is experimentally verified using X-ray by Lee et al.[15]. The early stage of droplet deformation can be observed and measured directly using light interference measurement. Dual-color measurement[18, 19] or color measurement[9] have both been developed in recent 20 years based on high-speed camera technology. The air-layer cushioning theory was firstly numerically modeled with 2D cases by Smith et al.[20], and later modified to axisymmetric model[21]. The lubrication pressure P in the air film and the characteristic thickness H^* for the droplet deformation with Stokes number are expressed by

$$P \sim \mu_g VR/H^2 \qquad \text{Eq.1-2}$$

$$H^* = RSt^{2/3} \qquad \text{Eq.1-3}$$

where the notation "~" means the two variables are proportional related, μ_g is the viscosity of the droplet, V is the impact velocity, R is the radius of the droplet, H is the distance between droplet and substrate and $St = \mu_g/(\rho RV)$ is non-dimensional Stokes number. The Stokes number represents the relationship between viscosity of air layer and inertia of the droplet. The thickness H^* is defined with the largest air film thickness that the droplet starts to deform.

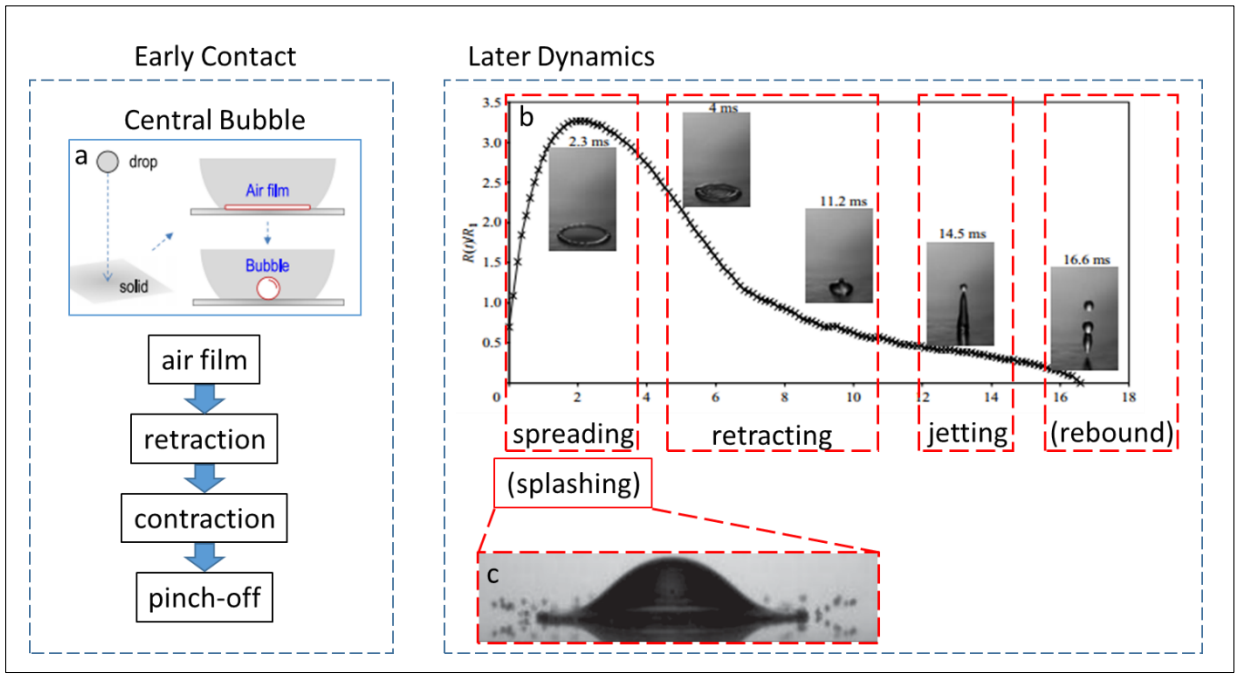

Figure 1-1. The whole process of droplet impact on a solid smooth surface. a) The air film retracts into a bubble. b) The spreading, retracting, jetting, and rebound after droplet impact on the hydrophobic surface. c) Splashing after droplet impact on the smooth solid surface. Figure a) & c) are reproduced from Reference [15] &[22] with permission from APS, Figure a) is reproduced from Reference[23] with permission from CUP.

These models can also be used to do some further analysis, such as the prediction of the initial radius of the contact line[24] or the size of the entrapped bubble[25]. The air bubble was not always observed when a droplet impacts on a smooth flat surface. If the impact velocity is very low, the air film can be unstable and break the axisymmetric structure, which allows the air to escape [21]. According to previous researches, the droplet viscosity can dramatically change the splashing dynamics.

After the droplet touches the substrate, the droplet would perform in many different ways, such as spreading, splashing, retracting, jetting, and rebound. Spreading happens right after the droplet touches the substrate. Droplet usually would spread over the surface until it reaches the maximum radius. The maximum spreading radius is an important parameter that has raised many researchers' interests. Numerous relationships [26-35] between the maximum radius and impact parameters have been modeled based on the balance between inertia, viscosity, and capillary force. Many numerical models match experimental results in the focused regime, and most of them obey the relationship $\beta = \frac{R_{max}}{R_0}$ as a linear relation. To define the value of the ratio β, different papers focused on different circumstances and the results can be different. Basically all of the definition of radius ratios are dependent on Weber number *We,* which is a dimensionless variable of the ratio between fluid inertia and surface tension. For example, Clanet et al.[31] developed an equation of $\beta \sim We^{1/4}$. Or Eggers's[36] expression $\beta = Re^{\frac{1}{5}} f(P)$, where *P* is the impact number defined by $P = We \cdot Re^{-2/5}$, and *Re* is the Reynolds number that represents the relationship between inertial forces and viscous forces.

After reaching the maximum radius, the liquid would retract or rebound and jet depending on the property of the liquid material and the substrate wettability. The work of Rioboo et al. [37] has shown that the surface properties can control whether the spreading droplet to recede or remain close to its maximum radius. Two papers of Bayer et al. [38] and Yokoi et al.[39] have both experimentally and numerically studied the influence of the contact angle on rebounding and jetting. An interesting aspect received attention during droplet impact, spreading, and rebounding is the contact time. Researchers found out that although different droplet impact velocities and surface wettability change the impact and rebounding shape a little bit, the contact time between droplet and substrate are always the same, only depend on the liquid property and droplet size $t_{c,th} = 2.6\sqrt{\frac{\rho D_0^3}{8\gamma}}$, where ρ is the liquid density, D_0 is the droplet diameter, and γ is the surface tension of the droplet.[40] Also, correspondingly, how to change or influence the contact time of bouncing droplet is another popular topic that has been studied.[41]

The splashing was discovered that happen at the same time the droplet spreads on the substrate. The main factor that determines whether droplet would splash is the impact velocity. The splashing threshold was defined by a so-called splashing parameter [42, 43], which is the influence combination of inertia, viscous stress, and surface tension together $K = We\sqrt{Re}$. For impact K>3000, a splash can be expected. Of course, this conclusion was drawn under atmosphere condition. If the surrounding air pressure is changed by changing the surface roughness, it was found to be a way to avoid splash.[44-47] In the real world, substrate and droplet movement can be not perpendicular to each other. A few studies [42, 48, 49] also focused on cases that droplet

splash impact and splash on inclined surfaces. Research has demonstrated that splash would happen in low-Weber number regime when the substrate angle is greater than 85°.[48]

During the whole process of droplet impact, the droplet deformation before impact is an essential part. The deformation of the droplet has also been showed to affect its further dynamics, including splashing and rebounding. This deformation is also a serious problem that needs to be studied and analyzed to deeply understand its principle. In the next section, recent researches related to droplet deformation is introduced in detail.

1.1.3 Recent Researches Related to Droplet Deformation before Impact

As stated in Section 1.1.1, people's understanding of the droplet impact started more than 200 years ago. With the development of technology in recent 60 years, more and more relevant phenomena have been discovered and studied. Air entrapment before impact is also deeply studied by many scientists.

Lee et al.[15] used X-ray to thoroughly observe the formation of an air bubble from air film. Contraction and retraction are shown clearly in Fig. 1-2. As shown, the full formation process would take less than $300\mu s$. He also discovered experimentally that the volume of trapped air is not related to the surface wettability, even though the droplet would be attached to the surface or detached from the surface.

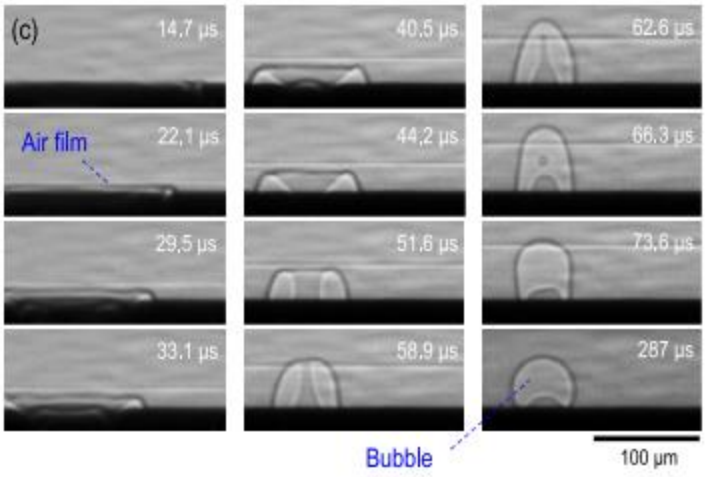

Figure 1-2. X-ray images showing the formation of an air bubble. The figure is reproduced from Reference [15] with permission from APS.

X-ray can undoubtedly give a clear image inside the droplet to study the evolution of the air bubble, but it is not an easy and convenient way. Bouwhuis et al.[50] used the standard high-speed camera, instead of X-ray, to study the development of air film under liquid droplet. He noticed that when the air film between droplet and substrate is very thin, light interference would be observed as colorful fringes shown in Fig. 1-3. The light interference pattern can be utilized via some algorithm to measure the distance (Details are stated in Section 1.3).

When trying to measure the air film thickness, the volume of the entrapped air bubble is found out to be not proportional to the impact velocity. The maximum entrapment of air bubble is determined by the effect of droplet inertia, the surface tension and the viscosity. Weber number introduced previous can be used to describe the relationship of inertia and surface tension. For the relationship between surface tension and viscosity, capillary number $Ca = \mu gU/\gamma$ is a very

important non-dimensional number, where μ is the viscosity, g is the gravitational constant, U is the impact velocity and γ is the surface tension.

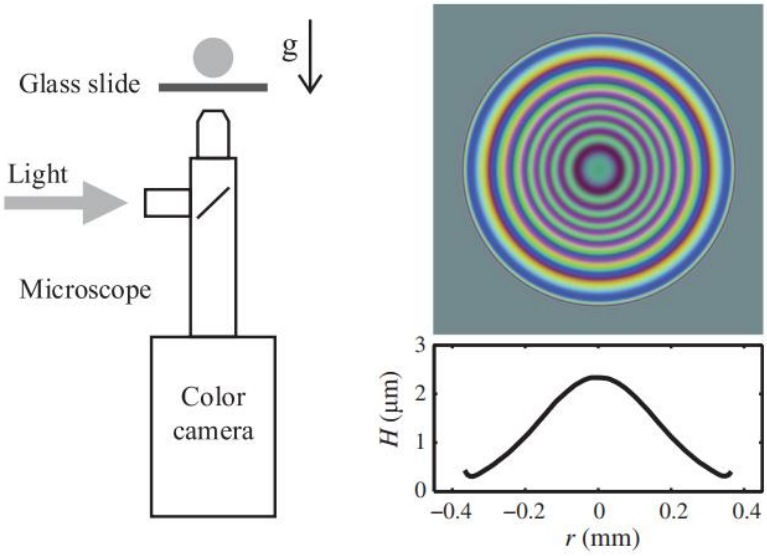

Figure 1-3. Experimental setup to measure air film thickness via a high-speed color camera. The figure is reproduced from Reference [50] with permission from APS.

His work also contributes to a simplified method to numerically study the air film development. Firstly, considering the bottom part of the droplet is relatively flat, lubrication approximation of the Navier-Stokes equation can be used to capture the relationship between pressure and air film height [51-54]:

$$\frac{\partial P_g}{\partial r} \sim \eta_g \frac{\partial^2 u_r}{\partial z^2} \qquad \text{Eq. 1-4}$$

That describes the viscous, incompressible gas flow under the droplet. Here, the notation "~" means the two variables are proportional related, P_g is the air film pressure, r and z are the coordinates in cylindrical coordinate system, u_r is the radially outward velocity of the gas, and η_g

is the viscosity of the gas. Coupling the lubrication equation with BI method (Boundary-Integral method), the numerically simulated results show agreement with the experimental results.

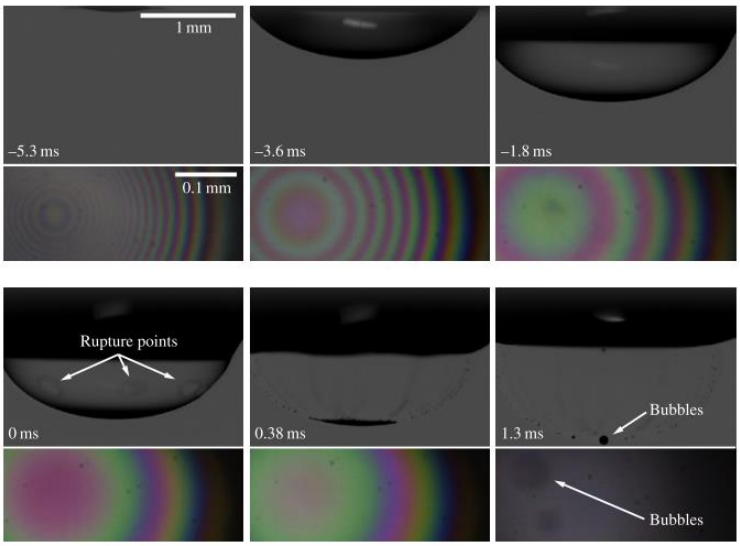

Figure 1-4. Air bubbles observed when a water droplet impacts into water pool simultaneously from side view and bottom view. The droplet diameter is about 3.0mm and the largest air bubble diameter is about 50μm. The figure is reproduced from Reference [55] with permission from CUP.

Figure 1-5. Air bubbles observed when a solid sphere impacts into a liquid pool. The figure is reproduced from Reference [25] with permission from CUP.

As shown in Fig. 1-4 &1-5, this kind of air entrapment not only happens when a liquid droplet impacts on a solid surface but also been observed when a liquid droplet impacts on a liquid surface[54, 55] and when a solid sphere impact into a liquid surface[25]. As long as the impact involves fluid, no matter in fluid or gas, there always would be a lubrication fluid layer between the impacting object and the fluids. The lubrication film will cause a significant increase in the local pressure, which results in liquid deformation and air bubble (if the impact happens in the air).

Ink-jet printing is a method that has been utilized widely in many fields, such as film coating and 3-D printer. However, the air bubble and air film formation sometimes can be pretty annoying. For example, a 3-D printed part can be different in its physical properties because of bubbles inside. Hence, it is necessary to find out a way to eliminate the air bubble. One common way to avoid bubbles is to change the air pressure under droplet. Tsai et al.[47] has shown in his paper that the micropatterns and air pressure would have a significant influence on the structure of air film and the following phenomena of a splash.

In current researches, the reasons causing the droplet deformation and air bubble entrapment have been thoroughly studied. Since it is due to the air pressure build-up, it would be challenging to avoid the air bubble formation without changing the substrate structure or decreasing the environmental pressure. Considering electrical force can also influence the shape of a droplet, there is great chance that electrohydrodynamics can help to eliminate the air film. In Section 1.2, electrohydrodynamics and its influence on droplets will be introduced.

1.2 Electrohydrodynamics and Its Influence on Droplet

Electrohydrodynamics is the study of the dynamics of electrically charged fluids[56]. It focuses on studying the motions of charged particles/molecules, and their interaction with electric fields and influence on the surrounding fluids. The influence on surrounding fluids can be utilized to avoid or reduce the pressure build-up when no charge is involved. This section will introduce basic knowledge about electrohydrodynamics and its influence on a droplet.

1.2.1 Maxwell Equations

Electrical charge is one of the fundamental properties of elementary particles that is responsible for the electro-hydro interaction. The unit of charge is electron charge $e = 1.6 \times 10^{-19}\mathrm{C}$. In most situations, the number of charges is extremely large, and the nearest separation can be ignored in the macroscopic standard. Hence, we can just take the influence of an infinite number of charges as local voltage, local electric field, local magnetic field, and local charge density. The relationship between charge density q and electric field E is governed by Gauss's Law[57]:

$$\varepsilon_0 \nabla \cdot \boldsymbol{E} = q + q_p \qquad \text{Eq. 1-5}$$

where $\varepsilon_0 = 8.8542 \times 10^{-12} F/m$ is the permittivity of free space, q_p is the charge density bounded in the object, which is also known as polarization charge density. For a charged body with a volume of V:

$$\int_V q_p dV = 0 \qquad \text{Eq. 1-6}$$

If define the vector $\boldsymbol{P}$ as the polarization vector, the equation can be rewritten into $q_p = -\nabla \cdot \boldsymbol{P}$. The displacement vector is defined by $\boldsymbol{D} = \varepsilon_0 \boldsymbol{E} + \boldsymbol{P}$. Gauss' Law can be restated as

$$\nabla \cdot \boldsymbol{D} = q \qquad \text{Eq. 1-7}$$

Another important equation is Faraday's Law, which introduces the relationship between the time-dependent magnetic field and electric field:

$$\nabla \cdot \boldsymbol{E} = -\frac{\partial \boldsymbol{B}}{\partial t} \qquad \text{Eq. 1-8}$$

Gauss's Law for magnetism indicates that no scalar source for the magnetic field

$$\nabla \cdot \boldsymbol{B} = 0 \qquad \text{Eq. 1-9}$$

Lastly, the movement of charge, either free charge or bounded in a body would cause current density, which generates a magnetic field. This theory is well-known as Ampere's Law:

$$\nabla \times \boldsymbol{H} = \boldsymbol{J} + \varepsilon \frac{\partial \boldsymbol{E}}{\partial t} \qquad \text{Eq. 1-10}$$

where $\boldsymbol{H}$ is the magnetic intensity field, and $\boldsymbol{J}$ is conduction current density

The combination of Eq. 1-7 to 1-10 are called Maxwell Equations, which are very important equations in electrohydrodynamics. In electrostatics, the electric field has a force effect on the charged body, which depends on the amount of charge and the local electric field. In electrohydrodynamics, the electric field will also cause stress in charged bodies. The electrical stress is defined by the Maxwell stress tensor. In general, the Maxwell stress tensor takes into account the effects of both electric and magnetic fields:

$$\sigma_{ij} = \epsilon_0 E_i E_j + \frac{1}{\mu_0} B_i B_j - \frac{1}{2}\left(\epsilon_0 E^2 + \frac{1}{\mu_0} B^2\right)\delta_{ij} \qquad \text{Eq. 1-11}$$

where ϵ_0 is the electric constant and μ_0 is the magnetic constant, *E* is the electric field, B is the magnetic field and δ_{ij} is Kronecker's delta, which is defined by

$$\delta_{ij} = \begin{cases} 0 & if \;\; i \neq j \\ 1 & if \;\; i = j \end{cases} \qquad \text{Eq. 1-12}$$

The electric field or magnectic field with index notation represents its component in a certain direction along *i*th axis or *j*th axis. The Maxwell stress tensor with notation of *ij* gives the flux of momentum parallel to the *i*th axis crossing a surface normal to the *j*th axis (in the negative direction) per unit of time.

For the situation where there is no magnetic effect or magnetic effect can be negligible (e.g., a charged body floating in an external electric field), the surface stress can be simplified to

$$\sigma = \frac{1}{2}\epsilon_0 E^2 \qquad \text{Eq. 1-13}$$

To calculate the Maxwell stress, electric field or electric displacement is necessary. For a charged body, the electric field is determined by the free charged distribution inside the body and the external electric field. It is easy to know the charge distribution in the conductor because the conductor always needs to be an equipotential body. However, for insulator or semiconductor, it is more complicated. Instead of free charges in a conductor, the electric field is generated by polarization in insulators and semiconductors. Detailed information about polarization is given in the next section.

1.2.2 Polarization

When charge transport in a body, based on the movability of free charges, the material can be divided into two kinds, conductor and insulator. For insulators, even though there is no free charge inside, but charge density would appear when positioned under an electrical field. The charge density change is caused by a polarization described above in Eq. 1-14. Because of the internal force between the atoms within a molecule, the center of the positive charge distribution is not at the same location as the center of the negative charge. If they are at the same location, the molecule is nonpolar. If they are not at the same location, the molecule has a permanent electric dipole which is called polar. In both cases, when the molecule is subject to an external electric field, their charge location will be redistributed to achieve a new balance of the electrical forces and internal forces. This charge redistribution would result in an internal electric field that is polarization field. The induced dipole is related to the external electric field:

$$\boldsymbol{P_m} = \alpha \boldsymbol{E} \qquad \text{Eq. 1-14}$$

where α is the polarizability of the molecule.

There are two different mechanisms that contribute to polarization. First is the electronic polarization, which is caused by the positive and negative charges, not at the same geometric center. Assuming electrons as a charge density cloud and nucleus placed a small distance from its center, the equation to calculate the induced dipole is $\boldsymbol{P_m} = 4\pi\varepsilon_0 a^2 \boldsymbol{E}$. The other kind of polarization is called the ionic polarization, which is caused by atoms that were ionized before applying the electric field. The induced electric moment is $\boldsymbol{P_m} = \frac{q^2}{m\omega_0^2}\boldsymbol{E}$, where m is the reduced mass of the molecule, ω_0 is the angular vibration frequency of the diatomic molecule. Summarizing the effect

of these two kinds of polarization and taking into account of the permanent dipole in the molecule, the polarizability of the molecule is $\alpha = \alpha_e + \alpha_i + \alpha_{or}$.

In a macroscopic view, the polarization vector $\boldsymbol{P}$ is dependent on the molecule density *N*, the polarizability α and the electric field *E*:

$$\boldsymbol{P} = N\alpha\boldsymbol{E} \qquad \text{Eq. 1-15}$$

For the classical relations with electric displacement

$$\mathbf{D} = \varepsilon_0\boldsymbol{E} + \mathbf{P} \qquad \text{Eq. 1-16}$$

Polarization is a common phenomenon in our daily life when electricity is involved. In research, it is also very important, especially when the electric field is relatively strong or the polarization of the material is large.

For conductor, semiconductor, or insulator, there is always some electric field on their surface. This results in electrical stress applied on the surface of their body. When the body is fluid, the fluid might be forced to deform. Next section will demonstrate the electrical effect on liquids.

1.2.3 Electrical Effect on Liquids

Liquids containing some charges might perform differently than the neutral ones. Assuming liquids as a conductor or at least a semiconductor, the charge a liquid body can hold is an interesting topic. Unlike the solid body, liquid bodies, such as water droplet or water jet, can have much smaller maximum charges. Back to 1882, Rayleigh[58] showed theoretically that an isolated charged liquid droplet would become unstable and break into smaller drops when the charge in it is large enough compared to the effect of surface tension which can stabilize the droplet

as an object. It is a pressure balance between the Laplace pressure and Maxwell stress shown in Fig. 1-6. As the charge in the droplet increases, the electric field increases proportionally. Theoretically, the electric stress does not have a limit as long as the charge amount increase, but the Laplace pressure does have an upper bound as the liquid volume is a constant (assuming the liquid is incompressible). Hence, there is a critical charge related to the surface tension. This critical charge of a stable droplet is called the Rayleigh limit. In his study, if the droplet is an ideal sphere, the Laplace pressure of the droplet would be

$$\mathrm{p} = \frac{2\gamma}{R} \qquad \text{Eq. 1-17}$$

where R is the radius of droplet and γ is the surface tension of droplet.

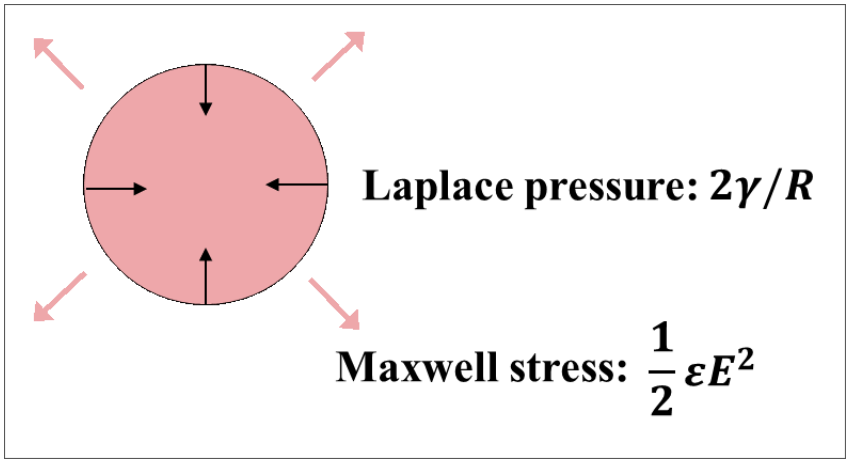

Figure 1-6. Rayleigh limit showing the balance between Maxwell stress and Laplace pressure.

Considering the electric field E is dependent on the charge q in the drop,

$$E = \frac{q}{4\pi\epsilon_0 R^2} \qquad \text{Eq. 1-18}$$

Hence, the critical charge of a single droplet, the so-called Rayleigh limit, can be calculated with

$$q^2 = 64\pi^2\epsilon_0\gamma R^3 \qquad \text{Eq. 1-19}$$

Rayleigh limit is a crucial parameter in electrohydrodynamics. Its essential role has been experimentally proved by Rayleigh and further discussed by many scientists later. [59-61]

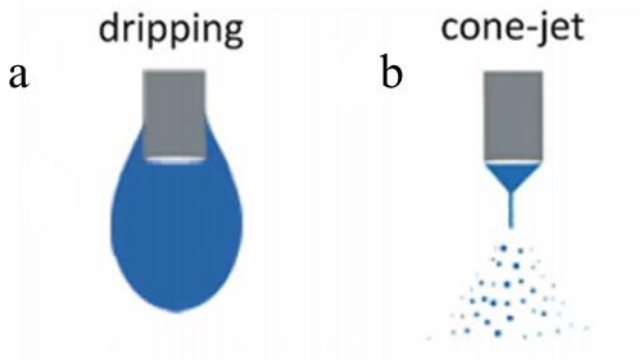

Figure 1-7. Taylor cone formed on the wettable nozzle. a) Liquid rises the wettable nozzle outer wall in the dripping mode. b) The cone is formed with its base connected to the nozzle when applied electric field, which is known as Taylor cone. The figure is adapted from Reference [62] with open access from Nature research.

Taylor was one of them, and he has made great contributions to electrohydrodynamics. About 80 years later, Melcher and Taylor[63] firstly defined the field of electrohydrodynamics in a review letter in 1969. This work was followed by Taylor's discovery of Taylor cone [64] and his model of LDM (Leaky dielectric model)[65]. As shown in Fig. 1-7, Taylor cone is a phenomenon discovered and analyzed by Taylor that liquid forming cone shape around the needle under the effect of electrical forces. The cone-shape liquid is also formed as a force balance of the surface tension and electrical stress [64]. An electrified fine jet will emit from the Taylor-cone, which undergoes the Rayleigh-Plateau instability and breaks up into droplets[66]. This is the fundamental

theory of electrospray. People have been using electrospray as a tool to coat a thin film on a substrate or to deliver drugs.

In the traditional electromechanical model, materials are divided into two kinds: perfect conductors and perfect dielectrics. With perfect conductors or dielectrics, the electric stress is perpendicular to the interface, and the deformation of interface shape serves a balance with electric stress. This is a kind of simplification of real materials. In the real world, all materials should be considered as dielectrics that have different permittivities and conductivities. Hence, Leaky-dielectric Model is introduced to explain physical phenomena. Taylor firstly introduced Leaky-dielectric model, which was further developed by many scientists.

An impressive example of recent work is done by Collins et al.[67]. His idea is to apply a voltage difference between a needle and a liquid pool, as shown in Fig. 1-8. In the leaky-dielectric model, the liquid would form a tip and a pinch-off droplet driven by electrical stress. He also built a mathematical model based on the Navier-Stokes equations to numerically verify the experiments:

$$\frac{\partial \boldsymbol{v}}{\partial t} + \boldsymbol{v} \cdot \nabla \boldsymbol{v} = Oh(-\nabla \mathrm{p} + \nabla^2 \boldsymbol{v}) \qquad \text{Eq. 1-20}$$

$$\nabla \cdot \boldsymbol{v} = \mathbf{0} \qquad \text{Eq. 1-21}$$

where $\boldsymbol{v}$ is velocity, p is pressure and Oh is Ohnesorge number. Ohnesorge number is a dimensionless number that relates the viscous forces to the inertial and surface forces defined by $Oh = \mu/\sqrt{\rho\sigma L}$

For the electrical system, Laplace's equation is:

$$\boldsymbol{E} = -\nabla \Phi \qquad \text{Eq. 1-22}$$

$$\nabla^2 \Phi = 0 \qquad \text{Eq. 1-23}$$

In the leaky-dielectric model used, the bulk density of free charge is zero, but the density of surface charge on the interface is governed by a charge transport equation:

$$\frac{\partial q}{\partial t} + \nabla_s \cdot (q\boldsymbol{v}) - \frac{1}{Pe}\nabla_s^2 q = \frac{1}{\alpha}\boldsymbol{n} \cdot \boldsymbol{E}_L \qquad \text{Eq. 1-24}$$

where q is charge density, $\boldsymbol{E}$ is the electric field. $Pe = \breve{R}\sigma_l/\varepsilon_l D_d$ is a non-dimensional constant called the Péclet number, where $\breve{R}$ is the radius of needle in Fig 1-8a, σ_l is the conductivity of the liquid, ε_l is the permittivity of the liquid, and D_d is the surface diffusion coefficient. Coupling the equations, he succeeded in numerically simulated the results that shows decent agreement with experiments.

Researches have shown that under some circumstances, electrical stress can significantly change the shape of fluid. Cone-shape deformation has been noticed and theoretically analyzed. It is reasonable to believe that the cone-shape deformation can also happen on the droplet. The following section gives some examples of droplet deformation under the effect of electrical stress.

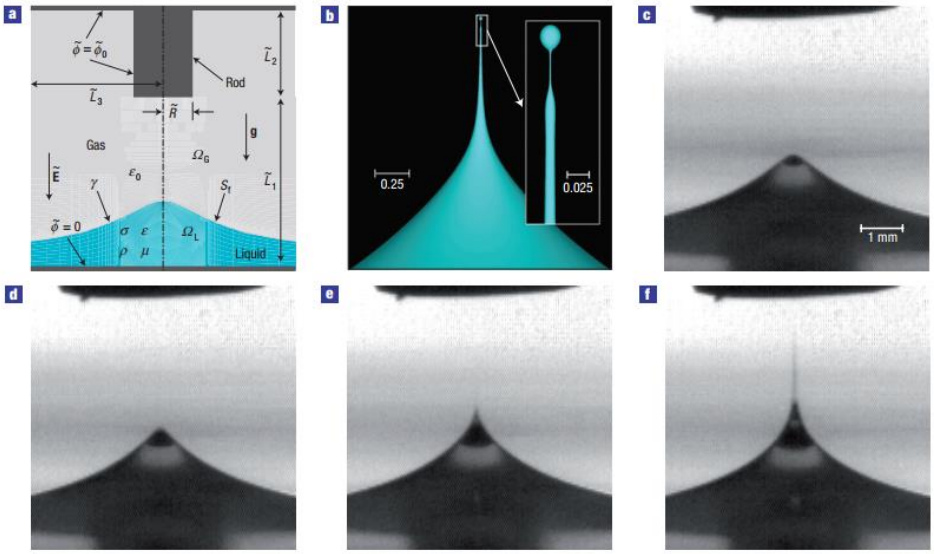

Figure 1-8. Electrohydrodynamics tip streaming. Voltage is applied between the needle and liquid pool. a) Definition sketch. b) Simulated tip streaming from a film of a leaky-dielectric liquid at the incipience of pinch-off: cone-jet(main image) and magnified view of the jet's tip (inset). c)–f) Experimental time sequence of tip streaming from a film of canola oil. The figure is reproduced from Reference[67] with permission from Springer Nature

1.2.4 Droplet Deformation under the Effect of Electric Fields

The electric forces can fundamentally change the shape of liquid objects has been demonstrated by Rayleigh[58]. Taylor extended Rayleigh's work to focus on electric stress applied on droplets. His research was done in two different cases: 1) charged droplet with a given charge amount sustained in an external electric field. 2) An uncharged droplet in a given electrical field. As shown in Fig. 1-9a, under the effect of the electric field, the neutral droplet would deform symmetrically along the direction of the electric field from a sphere into an ellipse and eventually a spindle shape with fission at its two tips. The deformation is caused by ionization, one kind of

polarization, that positive and negative charge would move towards opposite sides of the droplet resulting in increasing electrical field. Since the droplet is neutral before applying the electric field, the positive and negative charge density polarized must be the same, so the deformation is symmetrical along the direction of the electric field. For charged droplet, the deformation would become different like Fig. 1-9b. Based on the charge positive or negative, the charges inside the droplet would gather to one side of the drop, forcing the droplet to deform. The initial deformation would cause charge distribution again, which will increase the Maxwell stress. Finally, a cone shape or even fission appears. Because the droplet is initially charged, the polarization effect would be negligible compared to the effect of existing charges. The charge distribution is induced by applying the external electric field. As a result, the cone shape direction will be in the same or opposite direction based on positive or negative charge the droplet original contains.

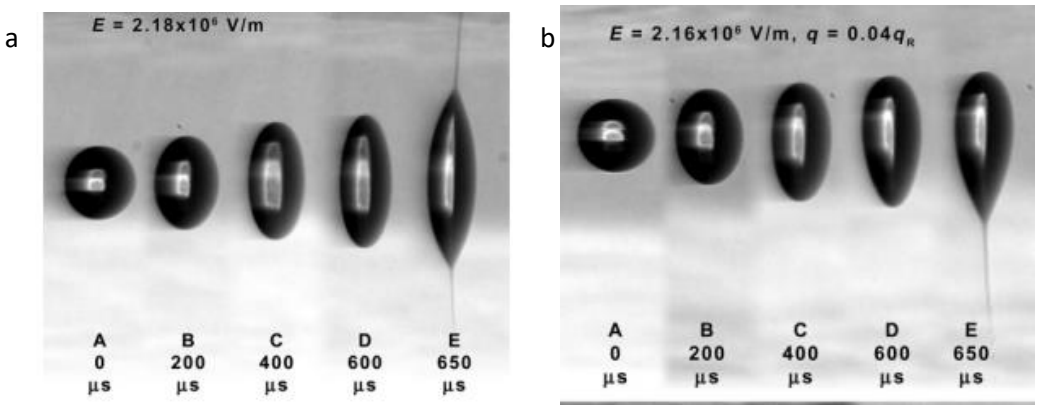

Figure 1-9. Droplet deformation under an electric field. a) neutral droplets b) charged droplets. The figure is reproduced from Reference [68] with permission from ACS.

After Taylor's research on electrical effect causing droplet deformation, more and more scientists raised their interest in this topic. Fig. 1-10 shows the deformation of a pair of droplets under an electric field.[69] A sharp and visible cone is observed between droplets tending to coalescence. Once the two droplets touch each other, there is no voltage difference between the two drops so that there is no electrical stress. Then the droplet would recoil to original shape like Fig. 1-10(c) or coalesce to a whole structure because of surface tension. The main factor that determines coalescence or recoil depends on the liquid volume. Similar to Taylor's droplet theory, electrical stress causes the cone-shaped deformation. The cone angle β is dependent on the voltage and size of the droplet. Roughly speaking, a higher voltage would result in sharper cone angle.

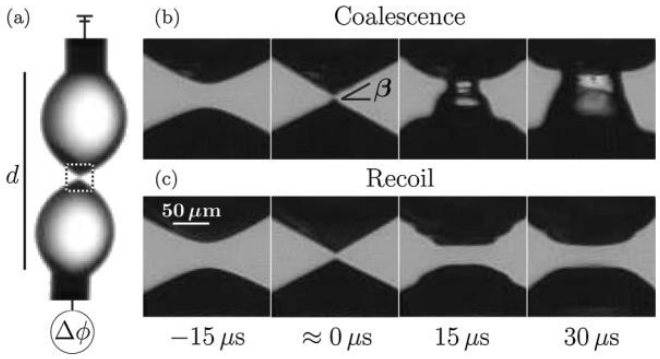

Figure 1-10. A pair of droplets applied with a voltage forming a cone-shape. The figure is reproduced from Reference [69] with permission from APS.

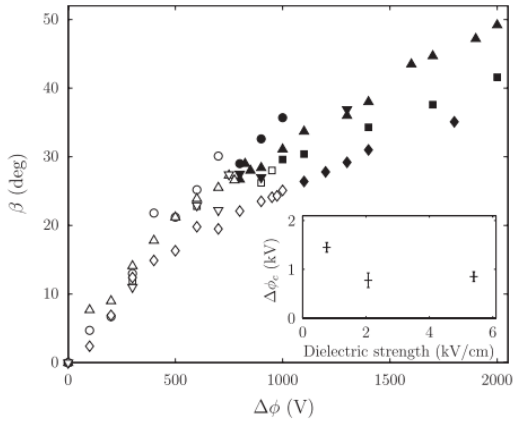

Figure 1-11. The relationship between voltage and cone angle. The figure is reproduced from Reference [69] with permission from APS.

1.3 Light Interference Measurement

As introduced in Section 1.1.2, light interference has been used to measure the thickness of thin films. The droplet deformation before impact would also form a thin air film which is difficult to be directly measured. Light interference can be a good option for measurement. In this section, the technology of light interference measurement is introduced in detail.

1.3.1 Background of Light Interference

Light interference is a common phenomenon in our life. In physics, interference is defined as a phenomenon in which two waves superpose to form a wave of higher, lower, or the same amplitude. It is usually referred to as the interaction of correlated waves or coherent waves, either because they come from the same light source or because the frequency is the same or nearly the same. Because of the wave-particle duality of light, interference of light can be observed.

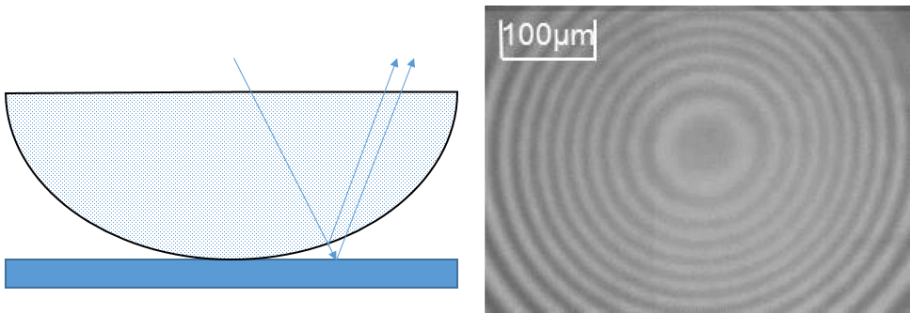

Figure 1-12. The experimental setup of Newton's ring.

A well-known example is Newton's ring shown in Fig 1-12. The convex lens and substrate glass are both transparent but can reflect part of the light. The air film between the two objects is the key to form the patterns of Newton's ring. A wave of light is reflected by the upper and lower boundaries of the thin film. The reflected lights would enhance or reduce the light intensity based on the air film thickness. The relationship between light intensity and air film thickness is demonstrated in Eq.1-25 and 1-26.[70] When the thickness of the film is an odd multiple of one quarter-wavelength of the light on it, the reflected light will cancel each other result in a destructive fringe. When the thickness of the film is an even multiple of the one quarter-wavelength of the light on it, the reflected light will enhance each other, forming the so-called constructive fringes.

For constructive fringes: $2n_{film}d\cos(\theta) = \left(m - \frac{1}{2}\right)\lambda$ $m = 1,2,3 \ldots$ Eq. 1-25

For destructive fringes: $2n_{film}d\cos(\theta) = m\lambda$ $m = 0,1,2,3 \ldots$ Eq. 1-26

where d is the film thickness, θ is the angle of incidence of light on the lower surface, n_{film} is the refractive index of the film, m is an integer greater than 0, and λ is the wavelength of the light.

Figure 1-13. Light interference fringes showing droplet deformation. The figure is reproduced from Reference [18] with permission from APS.

During droplet impact, the air film is also thin enough to form light interference patterns if a proper experimental setup is built. Fig. 1-13 is an example showing the air film development. This provides a new, cheaper, and easier way to measure the air film thickness [18]. Based on the equations above, the air film profile can be calculated according to a picture of light interference fringes. However, there is no way to distinguish the value of *m* from a signal picture. Hence, the thin film shape can be predicted, but the absolute value is challenging to determine from single interference patterns alone.

1.3.2 Measurement with Light Interference

To measure the absolute thickness of air film when liquid droplet impacts on a solid smooth surface. Light interference of a single wavelength light is not sufficient. Therefore, Van der Veen et al.[16] developed a new method using a high-speed color camera to obtain color fringes from white light.

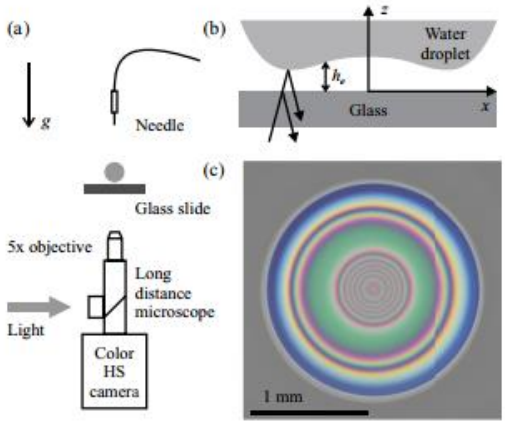

Figure 1-14. The experimental setup of color interference measurement. The figure is reproduced from Reference [16] with permission from APS

The main idea of extracting the absolute thickness of the air layer is to use the sRGB model to represent colors, and the values of color vectors (R_i, G_i, B_i) represent values of thickness. To realize this, the first step is to construct a set of reference colors by using a known convex lens to get Newton's ring similar pattern. Based on the sRGB(standard Red Green Blue) model, a few profile candidates can be generated that meet the color vectors. After that, the sRGB model needs to be converted into CIELAB model(a color space specified by the International Commission on Illumination) with three components: L for lightness information, a and b for color information. Eq. 1-27 shown below is used to calculate color difference that can determine the most appropriate air profile among the profile candidates.

$$dE^{ij} = [\left(a_e^j - a_r^i\right)^2 + \left(b_e^j - b_r^i\right)^2]^{1/2} \qquad \text{Eq. 1-27}$$

where dE^{ij} is the color difference for each color(a_e^j, b_e^j) in the sample and each color in reference color sample(a_r^j, b_r^j). For all the samples, the smallest sum of dE^{ij} indicates the most closest answer.

Even though Van der Veen introduced a method to determine the absolute air film profile, it requires a high-speed color camera. Actually, as an alternative way, the black-white high-speed camera is enough to do the same work. De Ruiter et al.[19] developed a dual-wavelength measurement to measure the air film thickness. Instead of using white light, he used lights with two different wavelengths. From each light interference fringes respectively, only intensity can be extracted as information to measure the air film thickness.

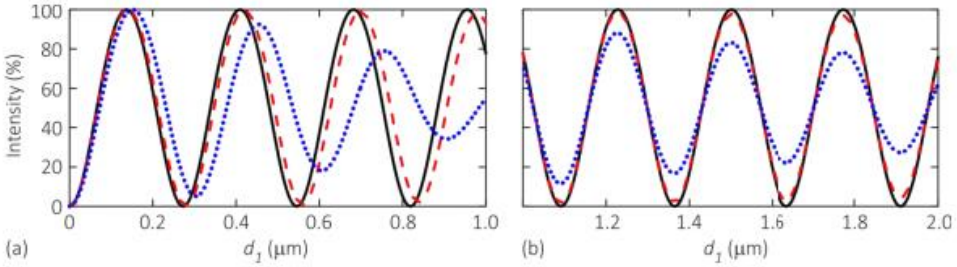

Figure 1-15. Light intensity versus air film thickness. Red dash(red light), blue dotted(blue light) and black solid(summary of the red dash and blue dotted). The figure is reproduced from Reference [19] with permission from APS.

Like the direct measurement, the film thickness should be derived from the interference fringes, with no reference point of known film thickness. In this case, the film thickness can only be derived to several options with the same relative shape. Even though the absolute film thickness cannot be extracted directly, the shape of the film can be extracted based on the interference fringes

and known profile. To find the absolute film thickness, standard film profiles with known thickness are created. The standard film profile can be compared with a family of profile candidates. Calculating the sum of SSE(squared errors) for each pair of profiles to find the minimum value, which indicates a unique solution for the absolute film thickness and exact film shape.

1.4 Outline of This Dissertation

In this dissertation, the dynamics of a charged liquid droplet impacting on the solid surface are studied experimentally and numerically. These works are based on the understanding of the neutral droplet deformation and air bubble entrapment before impact introduced in Section 1.1, as well as charged droplet deformation under electrical effect mentioned in Section 1.2. The central line of the dissertation is to understand the influence of charges in a droplet during the impact process. The goal of the work is to provide an alternative way to avoid air bubble entrapment by experimentally and numerically investigating the influence of charges on droplet impact. The rest of the dissertation is organized as follows.

In Chapter 2, the experimental setup and procedure are introduced in detail. The experimental setup includes a droplet generation part and impact observation part. Both parts involve some measurements/methods to realize the designed target. Results of these measurements and methods are also introduced.

In Chapter 3, I present the experimental results obtained using the setup and methods detailed in Chapter 2, focusing on how charges in droplet affect the droplet. The results indicate that weak charges could fundamentally change the impact dynamics of the liquid droplet. Analysis

brought a critical dimensionless parameter to define the dynamics change further. Based on the electrical effect, the droplet impact on insulator substrate and hydrophobic surfaces are also studied.

In Chapter 4, a numerical model is built to simulate the experimental processes and validate their results. Simplified governing equations are used to track the droplet surface evolution with the elapsed time. The numerical results show decent agreement with experimental results, also extend to some conditions that are hard to study experimentally.

In Chapter 5, the major contributions of this dissertation are summarized. Possible future research directions are also discussed.

Chapter 2 Experimental Setup and Methods

Chapter 2 will describe the experimental techniques utilized to observe the droplet impact process, especially to observe the droplet bottom deformation before touching the substrate. This chapter is divided into four parts: droplet generation, high-speed visualization, metal droplet generation, and charge measurement.

2.1 Droplet Generation

2.1.1 Droplet Generated from Capillary

I expected to have a broad range of droplet size so that I can easily change the Weber number and observe the influence of size on the impact dynamics. Herein, I designed two kinds of droplet generation devices to generate droplets with diameter varying from about 100μm to more than 4.0mm.

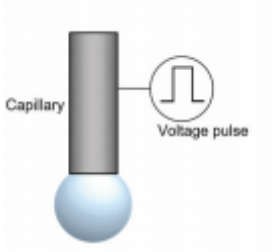

Figure 2-1. Schematic of droplet generation from a capillary.

One standard droplet generation device that has been widely used is to drive liquids out of a capillary needle with a syringe pump. To avoid intense oscillation, the pumping rate is usually set to be very slow so that the initial velocity of droplet is about zero when it detaches from the

needle. A signal generator that can generate pulse signal is connected to a precise pump to push the syringe. Every time a pulse signal sent to the pump, a single droplet is generated from the needle.

Pumping liquid through a capillary needle is the easiest way to generate single droplet. However, the size of the generated droplets is limited by Laplace pressure, which is caused by the surface tension. The minimum diameter of the droplet that can be generated from the capillary needle is determined by capillary length. Assuming liquid is attached to a needle like shown in Fig. 2-1, there is a pressure balance between Laplace pressure and inertia[71], which makes the droplet size could not be smaller than the critical value of capillary length. For water droplet in air, the capillary length is 2.71mm, which means the minimum diameter of water droplet generated from the needle could not be smaller than 2.71mm.

2.1.2 Droplet-on-Demand Generator

To generate droplets with 1mm diameter or even smaller ones, a structure called DoD(Droplet-on-Demand) device was designed and built. As shown in Fig 2-2, a standard speaker is used as an actuator, connected to a signal generator. Displacement and force can be adjusted by changing the voltage of the pulse signal. A 3D-printed PLA(Polylactic Acid) holder is fixed on the speaker for more stable performance. At the bottom of PLA holder, a cylinder-shape silicone pad is attached at the center. The silicone pad is the most important part for the DoD device to generate droplet. The diameter of the silicone pad needs to be much larger than the nozzle in the nozzle plate to ensure the generated droplets to be the same size. The nozzle plate is made of stainless steel blade. Laser marker (RGL-FM-10W Portable Fiber Laser Marker) upgraded to higher energy is used to drill nozzle on the stainless steel blade. The picture of the nozzle drilled by laser under

a microscope is shown below in Fig. 2-3. The advantage of using a laser marker is that the size of the drill nozzle can be adjusted easier according to requirement of experiments. In my experiments, the nozzle diameter changes from 75μm to about 800μm.

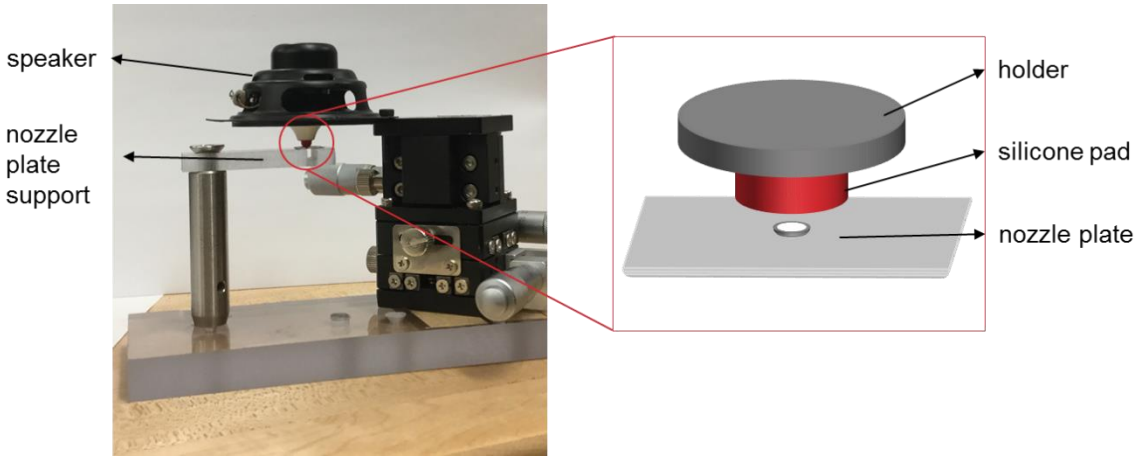

Figure 2-2. Photos of the real experimental setup with the schematic structure.

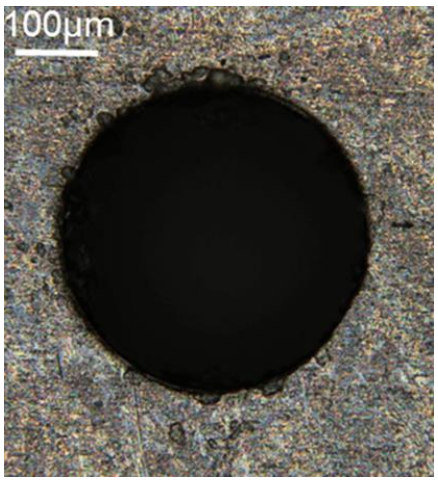

Figure 2-3. Laser drilled hole in the stainless steel blade.

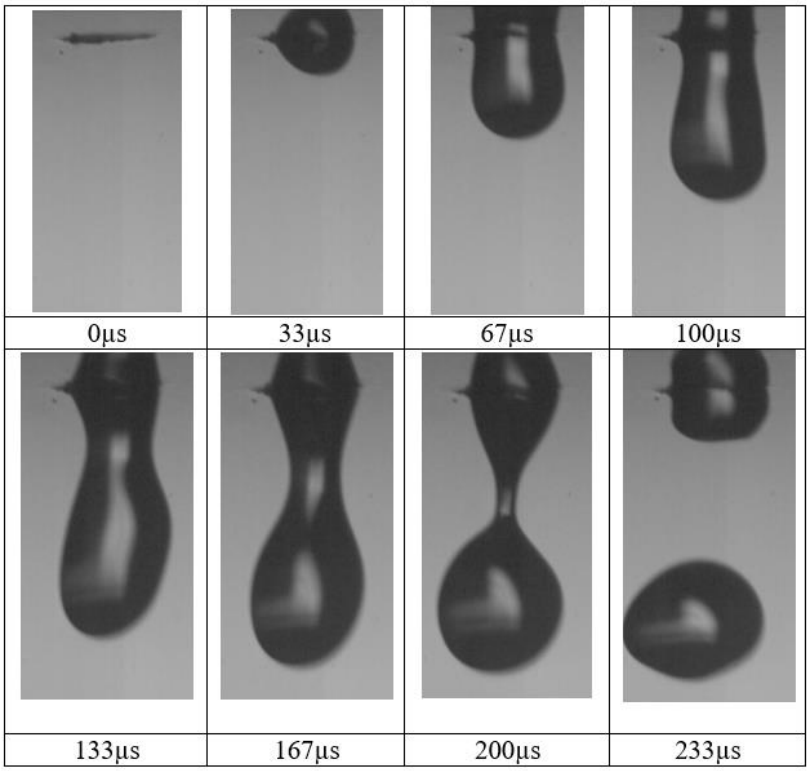

Figure 2-4. Water droplet generated from DoD. The diameter of the droplet is 280μm and the initial velocity is 0.12m/s

To generate a droplet, a pulse signal is sent from a signal generator to the speaker. The speaker is actuated to make the connected silicone pad move downward, pushing liquid on the nozzle plate out of the nozzle. The liquid pushed out of the nozzle will form a jet, which will eventually break up into a droplet. The diameter of the nozzle as well as the impact velocity of the silicone pad influence the droplet size. Pads made of aluminum and plastic are also tested to figure out the influence of flexibility. The results indicate that the flexibility of the impact pad does not

influence much on the initial velocity and size of the generated droplets. However, repeated experiments shows that the dimension of the generated droplets is very sensitive to the moving velocity of the silicone pad. Hence, the voltage of the pulse signal needs to be limited in a small range to ensure the DoD device has enough power to generate droplet and the initial velocity is very slow. The whole process of jet formation and droplet detachment is shown in Fig. 2-4. The detached droplet is comparable to the size of the nozzle. Nozzle size was changed to investigate the relationship between nozzle size and droplet size. In Table 2-1, the experimental results show clearly that the droplet size is comparable to the nozzle size.

Table 2-1. Nozzle Diameter and Droplet Diameter are comparable

Nozzle Diameter(μm)	75μm	218μm	438μm	514μm	632μm	789μm
Droplet Diameter(μm)	100μm	280μm	430μm	488μm	612μm	793μm

The DoD generator has been tested repeatedly, verifying that it can consistently generate droplets in the same size as designed. Based on this capability, Weber number of droplets can be adjusted by changing the diameter of the nozzle.

2.1.3 Applying Charges in Droplet

As mentioned in Chapter 1, droplet under the electric effect maybe will perform differently during the process of droplet impact. To investigate this problem, I need to apply charges into the droplet.

Firstly, applying electric field requires a reference location as the electrical ground. As shown in Fig. 2-5, I added a shielding electrode below the original droplet generator. The shielding

electrode can also ensure that there is no external electrical field applied on the droplet during the process of droplet impact on the substrate. The shielding electrode works both for capillary needle and DoD device. The shielding electrode is made of a stainless steel blade with a drilled nozzle in it. Since both the capillary needle and the nozzle plate are conductive, electrical potential difference is directly applied between the capillary needle or nozzle plate and the shielding electrode. Droplets generated from both of the droplet generators carries the same voltage as the potential difference applied on droplet generation device. The charges applied in droplets is dependent on the size of the droplet and the voltage applied on it.

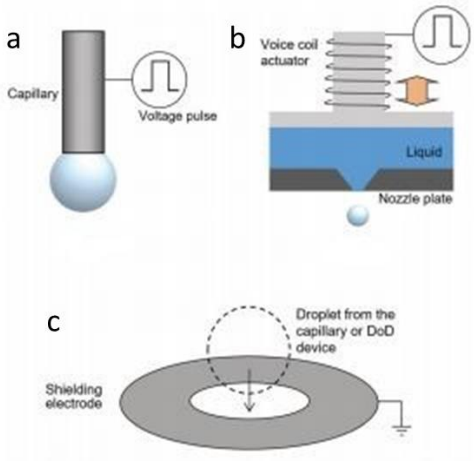

Figure 2-5. Schematic of droplet generator with charges applied. a) droplet generated from capillary needle. b) droplet generated from DoD. c) shielding electrode for applying charges in droplet.

2.2 High-Speed Visualization

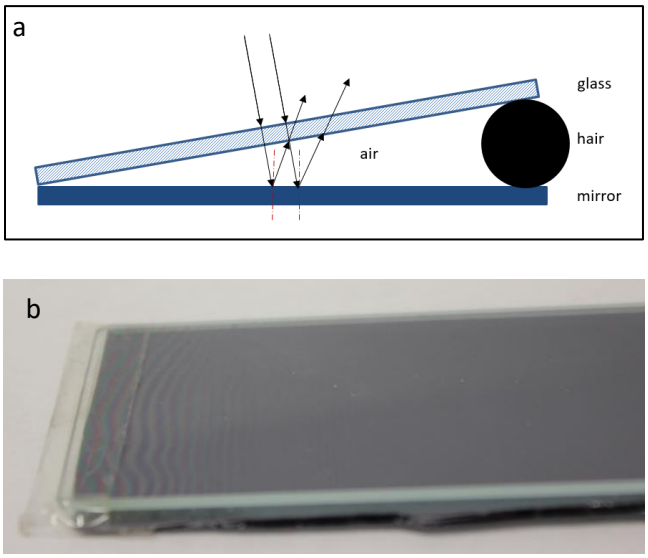

Figure 2-6. Wedge light interference a) schematic of air wedge and b) interference fringes.

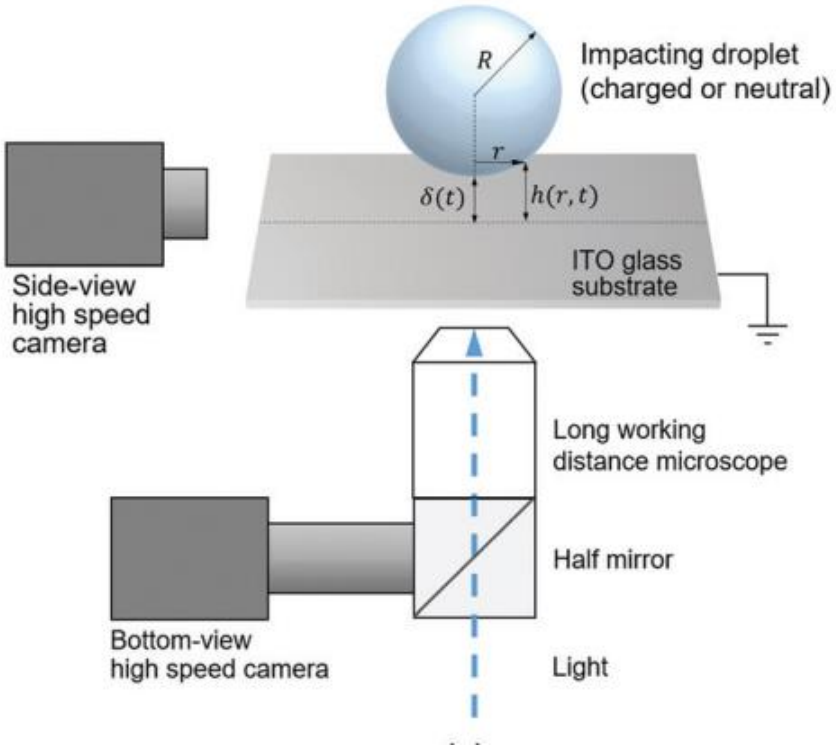

Figure 2-7. Experimental setup of impact high-speed visualization.

As stated in Section 1-3, light interference can be used to measure the air film profile. I started from observing light interference fringes with an air wedge, to verify the light condition is capable of forming interference fringes. A hair is put between a clean glass and a flat mirror to build an air wedge (Fig. 2-6a). As shown in Fig. 2-6b, the interference fringes are pretty obvious to be observed, which proved that the light condition is good enough for light interference measurement.

According to previous research[16, 18, 19, 50], when a droplet impacting substrate, instead of forming interference fringes like shown in Fig. 2-6b, it is more like a Newton Ring (Fig. 1-12), which is a light interference fringes between a convex lens and a smooth flat surface. For a droplet, light interference measurement is an excellent method to be utilized to measure the air film thickness. To observe the development of air film, the experimental setup is built as shown in Fig. 2-7. ITO coated glass is chosen as the substrate because it is transparent and conductive. Side camera and bottom camera are capable of observing impacting process simultaneously. The model of the high-speed camera used here is Photron SA5. The frame rate of this camera can reach up to 1.5 million fps (Frame Per Second), while the most frequently used frame rate for both cameras are 50,000 fps. Considering the high-speed camera is a black-white camera, direct measurement using colorful images introduced by Van der veen et al.[16] is not suitable. Instead, dual-wavelength measurement [18, 19] is more appropriate for this equipment. Blue and red LEDs (light-emitting diode) were used for lighting. The wavelength of blue light is 440 nm while the red light is 600nm. Due to the different wavelengths of lights, the interference fringes are different (Fig. 2-8). The plot in Fig. 2-9 shows the relationship between light intensities and air film thickness. As shown, one cycle represents the thickness of 0-900nm. This means for a pair of

intensities from blue and red LEDs, the thickness is unique if the thickness is under 900nm. For fringes under a neutral droplet, the air film thickness at the outer fringe is about zero. This outer fringe can be used as a reference point. The measurement results will be shown later in Section 3.2.

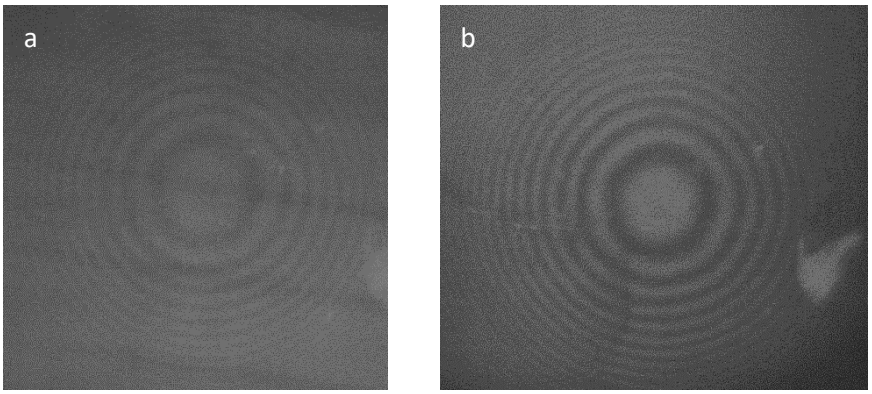

Figure 2-8. Interference fringes with under different lights. a) blue light. b) red light

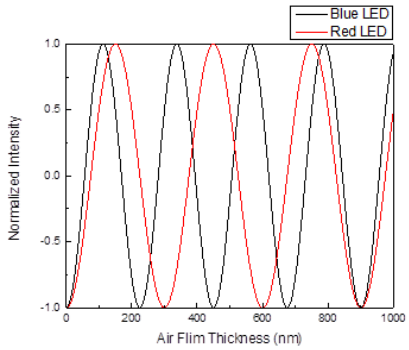

Figure 2-9. Light intensity versus air film thickness

2.3 Metal Droplet Generation

To experimentally study the impact dynamics of droplet, liquids such as water, ethanol, or methanol were usually used in previous research[4, 9, 14-16, 27, 28, 42, 43, 72-76]. Considering metal droplet is different in many physical properties compared to common liquid, I expected to

study the impact dynamics of the metal droplet. To prevent oxidation and ensure the metal droplet in liquid status during the whole impact process, Hao et al.[77] built a chamber full of nitrogen and heated it up to about 200°C. Instead of using this complicated experimental setup, a low melting point alloy is used in my experiments. The alloy is a lead-bismuth (Pb–Bi) based eutectic alloy (Roto 117) with a low melting temperature of 47.2 °C(117 °F). To melt the Pb-Bi alloy and maintain it in liquid status, I designed and built a water bath device as shown in Fig. 2-10. Liquid metal is enclosed inside the syringe surrounded by warm water. The heater bead attached on the container has a feedback sensor that can control the temperature of the water as needed. For my experiments, the temperature of water is 60°C(140°F) to 70°C(158°F). This temperature is verified that is high enough to ensure the metal in liquid status during the whole impact process.

As stated in Section 2.1, the size of droplets generated from syringe has a limitation. The minimum diameter of water droplets is about 2.7 mm, while the minimum diameter of metal droplets is about 4.0 mm, because the surface tension of Pb-Bi alloy is greater than water. Referring to Section 2.1.2, the DoD device is needed to generate smaller droplets. For DoD device introduced in Chapter 2, a heater attached on the nozzle plate can keep the temperature of the Pb-Bi alloy hot enough to prevent solidification. Another problem that needs to be solved is oxidation. The melted metal is very easy to oxidize when surrounded by air. Hence, a layer of oxide will cover the generated droplet. The oxide layer will prevent the droplet deformation, especially for small droplets generated from DoD device. To solve this problem, I smeared oil around the nozzle plate and the needle to cover the generated droplet with a layer of oil. This layer of oil isolates the metal droplet from the air, realizing the target of preventing oxidation.

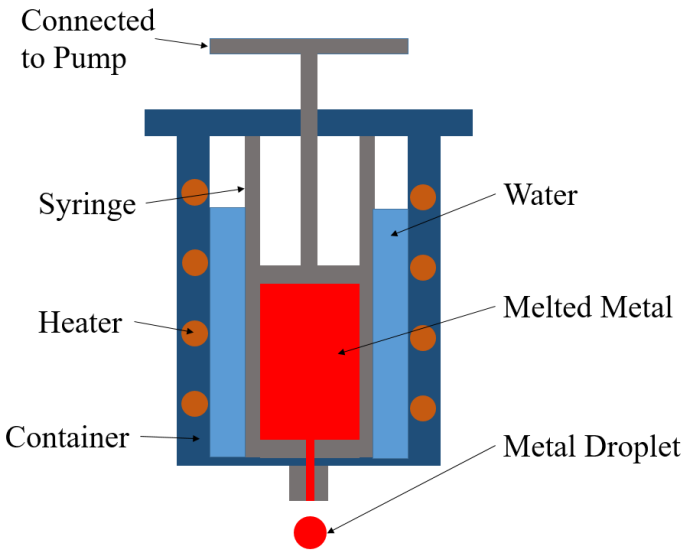

Figure 2-10. Water bath device to melt metal

2.4 Charge Measurement

When doing the experiments and analyzing data based on experimental results, it is very important to know the exact charge amount the droplet carries. Hence, I need a method or a measurement to measure the charge amount in a droplet. I used two experimentally methods to measure it and used the software COMSOL Multiphysics to verify the results numerically.

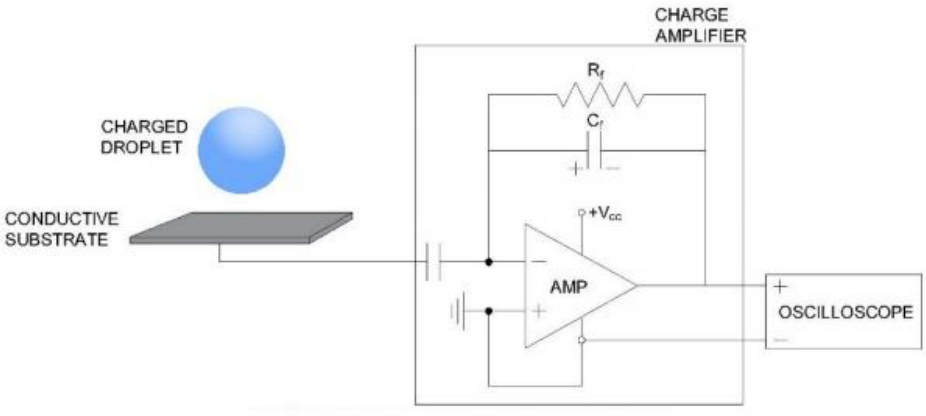

Figure 2-11. Schematic of the charge measurement with a charge amplifier

The first method is to use the charge amplifier to measure the charge amount directly. The model of the charge amplifier used to measure the charge amount in the droplet is HAMAMATSU H4083. The setup is shown in Fig. 2-11. The gain of this charge amplifier is 0.5V/pC. Every time a charged droplet impact on the conductive substrate, a pulse signal will be shown on the oscilloscope. The amount of charge is proportional to the peak of the pulse recorded.

Another method to measure the charge amount is an indirect measurement. Firstly, the droplet impact process can be considered vertical movement so that there is no horizontal displacement. After applying a parallel electrical field like Fig. 2-12, the impact location of a charged droplet will be influenced. The impact time *t* can be considered unchanged because adding horizontal electric field does not influence the impact movement on vertical direction.

$$\boldsymbol{F = Eq} \qquad \text{Eq. 2-1}$$

$$\boldsymbol{x = \frac{1}{2}at^2 = \frac{1}{2}\frac{Eq}{m}t^2} \qquad \text{Eq. 2-2}$$

where *F* is the electrical force, *E* is the electric field, *q* is the charge amount in the droplet, *m* is the mass of the droplet, and *x* is the horizontal displacement. Hence, the displacement of the impact location is proportional to the electric field and the charge amount the droplet carries. If the electric field is the same, the displacement is only proportional to the charge amount. This reveals the method of measuring charge amount via measuring the displacement on substrate.

The experimental results of these two measurements are comparable to each other. For example, for a 1kV charged droplet with a standoff distance of 8mm, the amount of charges

measured directly from the charge amplifier is 1.10×10^{-11} C, while the amount measured indirectly from the displacement is 1.08×10^{-11} C.

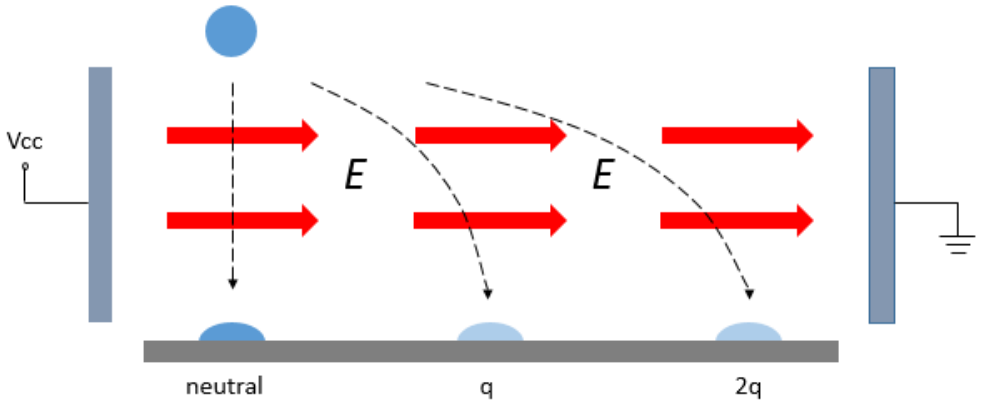

Figure 2-12. Schematic of the charge measurement with the horizontal electric field. The displacement of droplet impact position on horizontal direction is proportional to the charge amount the droplet carries if the external electric field Vcc is unchanged.

I also used COMSOL to calculate the charge amount numerically. An example of the COMSOL simulation is shown in Fig. 2-13. Two-phase flow model and electrostatics model are coupled in COMSOL for this case. An initial voltage is applied to the droplet, which equals to the electric potential applied on the droplet generator. After setting the meshing method and mesh size, the charge carried by the droplet can be calculated. For the same case mentioned above(1kV voltage with a standoff distance of 8mm), the charge amount calculated from the simulation is 0.9×10^{-11}C, which is comparable to two results measured from the experiments. Repeated experiments were done to check the reliability of these three methods. The results from charge amplifier measurement and the horizontal displacement measurement are very close to each. However, the difference between experimental and numerical is noticeable. Table 2-2 shows an

example of charge measurement for millimeter-sized water droplet with 10 mm standoff distance. The results of numerical simulation are about half of the value measured in experiments. This is because the droplet is considered as a perfect conductor, which does not match the real situation. Even though there is some difference between experimental measurement and numerical measurement, it is still within the range of our tolerance for further analysis. The COMSOL model is also used to calculate the local electric field and Maxwell's stress in the later analysis (details introduced in Chapter 3).

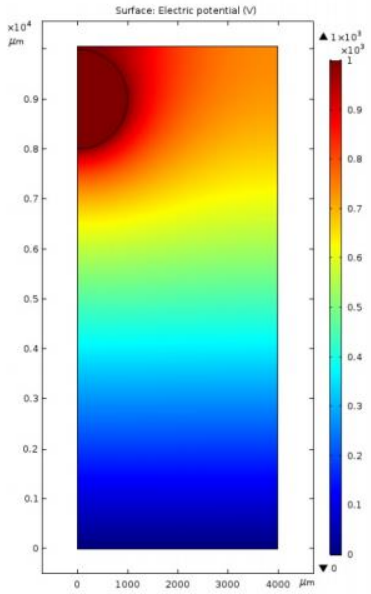

Figure 2-13. COMSOL simulation of the electric potential. Here, the droplet with 2mm diameter is 8 mm away from the shielding electrode. The droplet is charged with 1kV voltage. The simulation also provides information on electric field strength, the charge density, and the total charge amount the droplet carries.

Table 2-2. Experimental data of charge measurement

Voltage(V)	500	1000	2000	3000	4000	4700
Experimental(C)	1.10×10^{-12}	3.56×10^{-12}	6.01×10^{-12}	6.90×10^{-12}	9.30×10^{-12}	1.01×10^{-11}
Numerical(C)	5.3×10^{-13}	1.06×10^{-12}	2.12×10^{-12}	3.18×10^{-12}	4.24×10^{-12}	4.98×10^{-12}

Chapter 3 Weakly Charged Droplets Fundamentally Change Impact Dynamics on Flat Surfaces

Most of the results presented in this chapter were published in Fan Gao, Hao Yi, Rui Qiao, Lehua Qi, and Weiwei Deng. "Weakly charged droplet fundamentally changes impact dynamics on flat surfaces." Soft Matter, 2019, **15**(28), 5548-5553.

3.1 Introduction

The impact of droplets on a solid substrate is a ubiquitous and intriguing phenomenon that draws sustained research interests, with recent intensified studies motivated by numerous conventional and emerging applications such as bioaerosol generation[78], additive manufacturing[79, 80], spray coating[81, 82], pesticide applications[83], and material depositions[84]. At the early stage of droplet impact on a flat and smooth solid surface, the air pressure underneath the droplet increases rapidly as the thin layer of air is being squeezed out before the droplet wets the surface. This buildup of air pressure flattens or even dents the droplet, forming a nonequilibrium convex lens shaped air film that involves multiple length scales. The interplay of the delicate gas film structure and drainage flow critically influences the subsequent outcomes such as contact time[41, 85], splashing[4, 76, 86-89], rebound[85, 90-94], and bubble entrapment[4, 95, 96].

On the other hand, electric charges are often found in naturally or artificially formed droplets. Lord Kelvin's water dropper showed spontaneous charging of droplets occurs when they pinch-off from the bulk liquid[97]. Smith[98] found that the millimeter-sized raindrops in London

carry negative or positive charges up to about 1.0×10^{-10} C. Certain inkjet printers rely on charges to select and steer droplets. Those charged droplets would eventually impact on some substrates, but the impact dynamics of charged droplets remains poorly understood.

In this chapter, it is introduced that even modest charge levels can characteristically change the outcome of the whole impact event because the Maxwell stress induced by surface charges alters the air film structure formed before contact. The Maxwell stress overcomes gas pressure and promptly deforms the droplet bottom into a conical tip to make a center touchdown, forming a circular contact line moving outwards that does not trap any gas. I further show that the center touchdown happens when the charge level is above a critical value, which only depends on the capillary number based on the gas viscosity. The critical charge level is as low as about 1% of the maximum charge the droplet can carry, a result due to the local surface charge intensification. The finding provides new insights into several applications such as mitigating pinhole defects in droplet-based additive manufacturing.

3.2 Neutral Liquid Droplet Impact

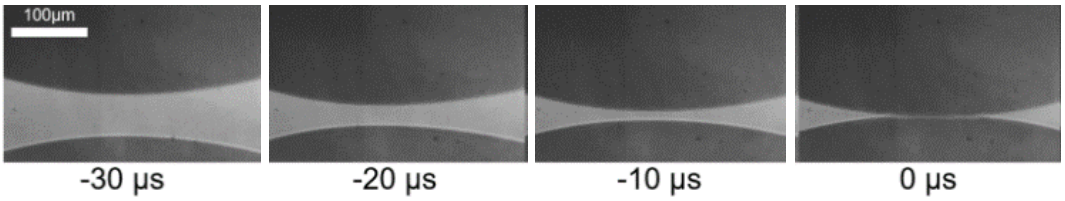

Figure 3-1. Side-view of neutral droplet impact process. The impact velocity is 0.6m/s, the local curvature of the droplet is 1.25 mm.

Firstly, I repeated the experiments have been done before to verify the robustness of the experimental setup as well as the reliability of the measurements and methods. Hence, I started the

experiments from observing the impact of neutral liquid droplet. In the experiments, I used tape water and ethanol (200 proof) to generate droplet because these two kinds of liquids were used before so that it is easy to compare the results to verify the reliability of my experimental setup.

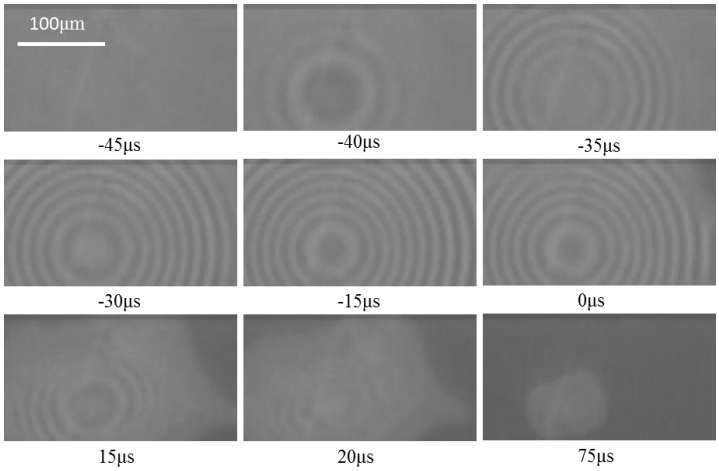

Figure 3-2. Bottom-view of neutral droplet impact process.

As introduced in Chapter 1, previous research[9, 16, 18, 19, 91, 92] has stated that a droplet will form a strong air pressure build-up between the droplet and the substrate during the impact process, which will cause a dimple at the bottom of the droplet. This dimple allows air to stay in the gap forming an air film. After droplet touching the substrate, the whole air film is entrapped between the droplet and the substrate. Due to the surface tension of the liquid/gas interface, the air film will retract and contract in a very short time, usually takes less than 100 μs, and eventually contract into an air bubble. The diameter of this air bubble is dependent on the size of the droplet. Many different models have been established based on different conditions, but all of them reached the same conclusion that larger droplet can entrap larger air bubble. They also reached agreement in the distance that droplet start to deform. For water droplet with about 3.0 mm diameter, the

distance that the droplet starts to deform is 3-5 μm [14]. The distance is dependent on the impact velocity.

Using the droplet generator and the high-speed visualization technique, the side view camera and the bottom view camera can observe and record images simultaneously. Fig. 3-1 shows an example of the images captured from the side view camera. The impact velocity is about 0.6m/s and the local curvature of the droplet is 1.25mm. The reflection of glass makes it looks like two droplets move towards each other, but it is actually only one droplet impact on glass. There is a little bit deformation can be observed in the last two frames, especially the last one. The bright gap between the two dark areas proves the air film has already formed because of lubrication pressure. The droplet bottom appears to be flattened into an about 100μm diameter disk by the thin air cushion beneath. However, the exact air film profile is hard to distinguish from the side view images. On the other hand, the bottom view images in Fig. 3-2 shows how the air film develops clearly by showing the evolution of the fringes. It is can be learned from the fringes that the droplet deformation starts from the center, where is also the lowest position of the droplet. Then the deformation expands outward until the droplet touches the substrate somewhere at the outer fringe. The wetting moves radial towards the center, and eventually forms a bubble as shown in the last frame of Fig. 3-2.

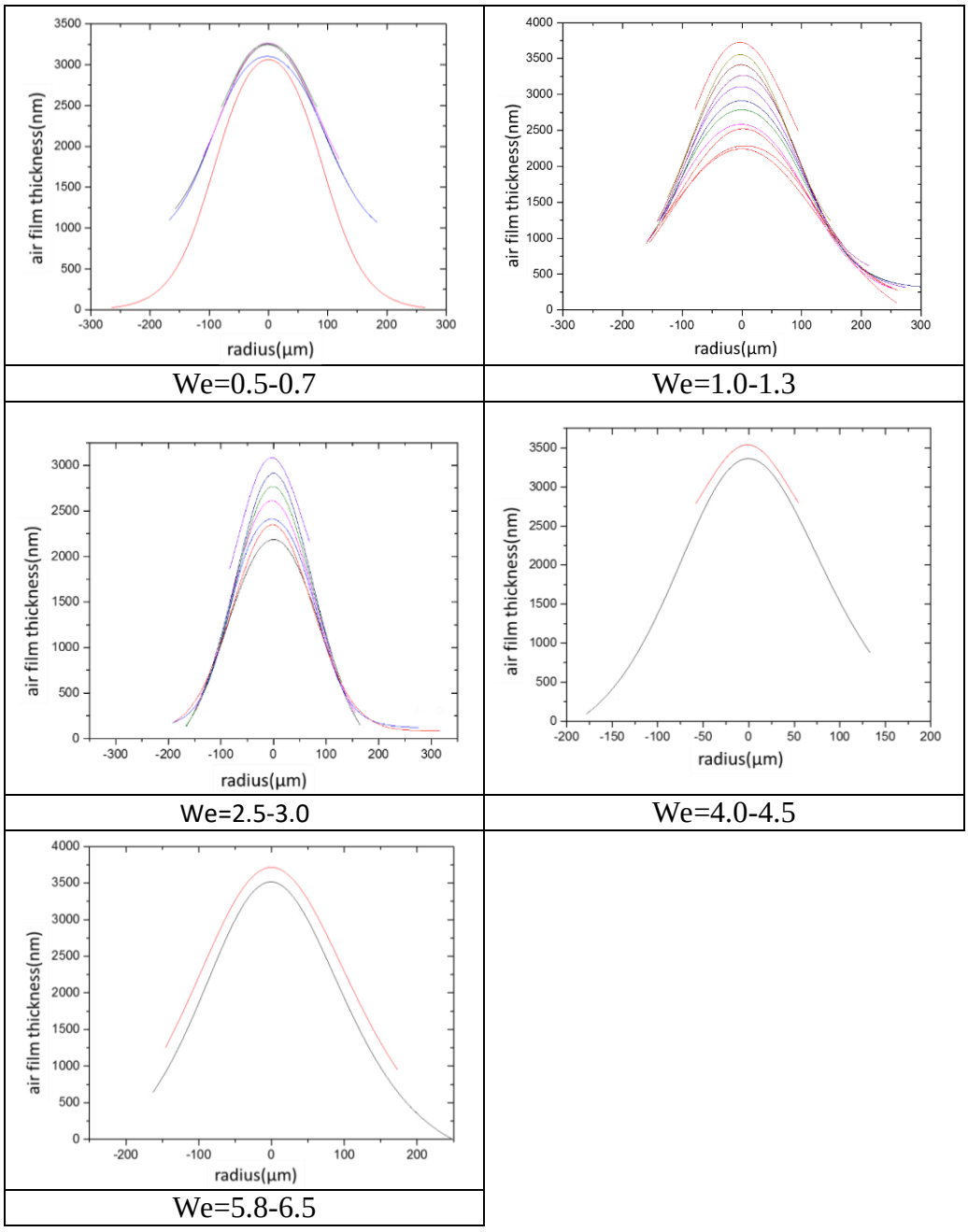

Figure 3-3. Different Weber numbers result in the formation of different air film profiles. The figures shows the evolution of air film versus time. The curves are plotted every 10μs based on bottom view images when Weber number is different.

Based on the fringes during droplet impact, the air film profiles can be plotted by using dual-wavelength measurement. Here in Fig. 3-3, the evolutions of air film profiles with different Weber numbers are plotted. For each case, the impact velocity and radius are measured directly from the side view images. The observation shows that the droplet always deform, but the shape of air films may differ when the Weber number changes. Some of the plots are not symmetric, because the images captured from the bottom view camera are not symmetric. To compare the profiles among different cases, the profiles of the last moment before wetting are plotted together in Fig. 3-4. It is surprising that the thickness of air film is not proportional to the impact velocity, but the results actually shows decent agreement with the work of Bouwhuis et al. [17].

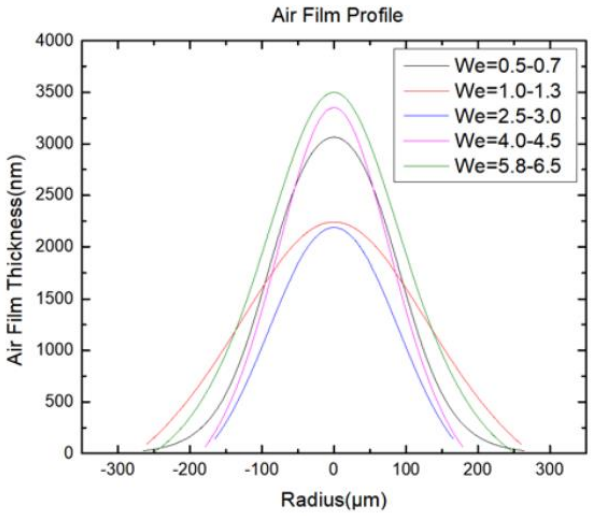

Figure 3-4. Air film profiles measured by using the dual-wavelength with different Weber numbers.

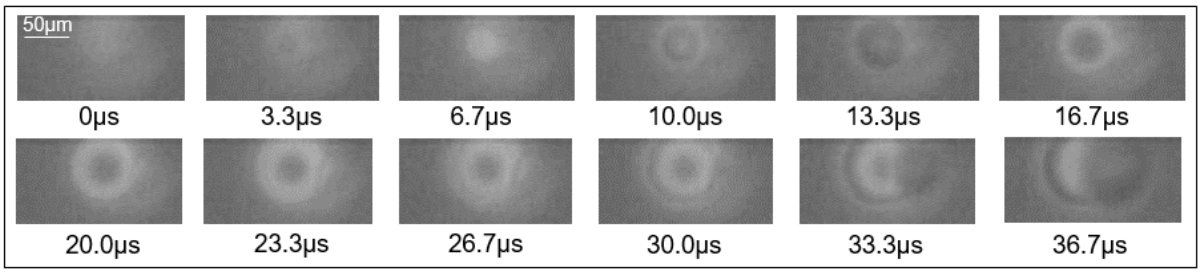

Figure 3-5. Fringes of air film under 280μm neutral droplet. The impact velocity is 0.22 m/s.

The impact of smaller droplets generated from DoD device was also observed. Smaller droplets will form relative smaller deformation when the impacting velocity is the same with large droplet, because the Laplace pressure of smaller droplets is larger. As a result, the deformation might be too small to be noticed from side view. However, from bottom view, the deformation can still be observed. As shown in Fig. 3-5, there are fringes observed before the droplet touches the substrate (wetting starts from 30.0μs). There are only two dark fringes observed, which means the thickness of air film is about 300nm for a 280μm diameter droplet with 0.22m/s impact velocity.

When the impact velocity is extremely low (We< 0.5 in our experiments), there is no air bubble formation. Nevertheless, the interference fringes are still visible before the droplet touches the substrate, which means the droplet still would deform before touching the substrate. This is because when the impact velocity is slow, the pressure build-up of the air film is also so weak that any small disturbance may break the balance. Instead of concentrating to the center, the wetting process sweeps from one side to the other as shown in Fig. 3-6. For Weber number ranging from 0.5 to 1.0, the bubble formation is still not a guarantee. Sometimes the air bubble is observed while sometimes not. This is still mainly because the pressure under droplet is not strong enough. When Weber number is greater than 1.0, the air bubble entrapment under droplet is observed every time.

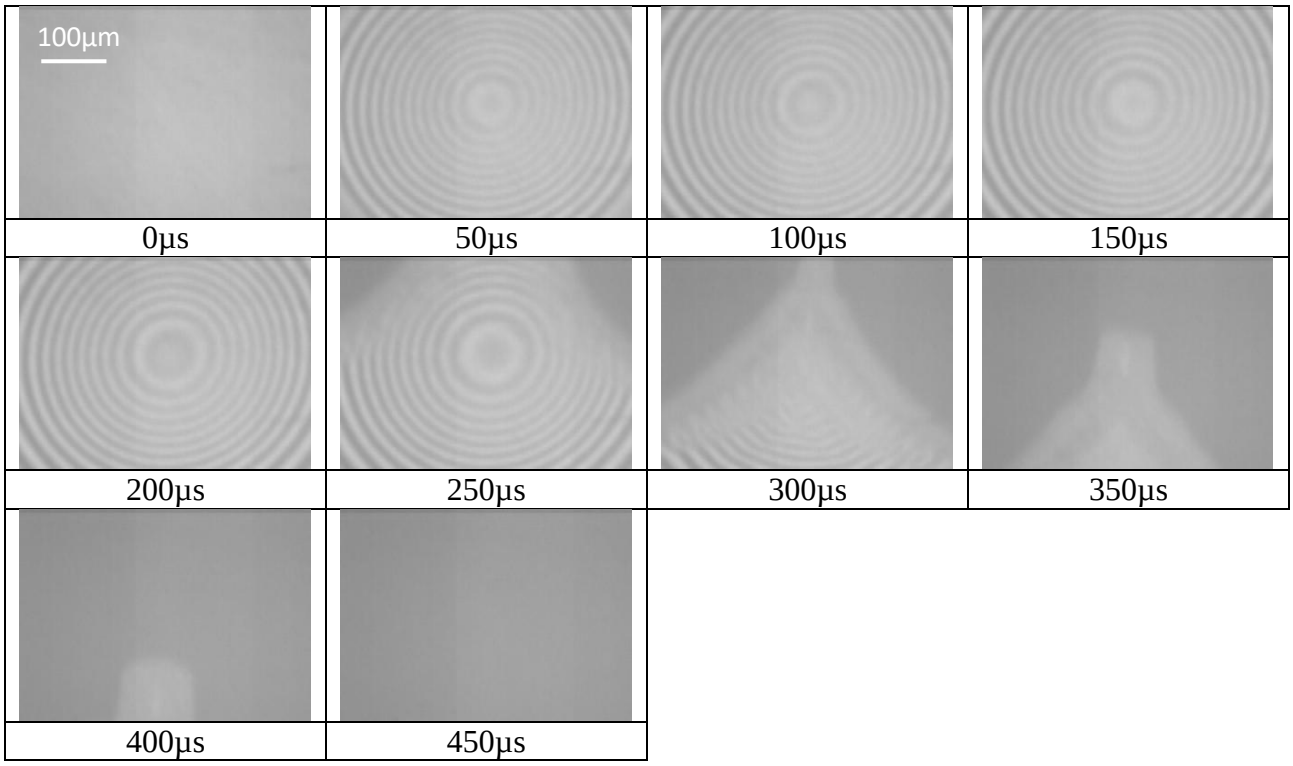

Figure 3-6. No bubble is trapped under the droplet when impact velocity is too slow. The droplet diameter is about 2.9mm. Weber number is 0.5.

Another very interesting phenomenon was noticed when doing the experiments. When the Weber number is around 2.0, a wide air disk is observed, as shown in Fig. 3-7. Based on the dual-wavelength measurement, the air film profile can be plotted. From the air film plot, the edge of the air film is very broad compared to other cases, and the thickness of this broad edge does not change a lot. In the meantime, the center part of the air film keeps falling down to squeeze the air out. This air disk is also observed before by Van der Veen et al.[16]. It is believed that there must be some pressure balance specific for this case to hold the air disk at the same distance. However, there is no reasonable explanation about the formation of the air disk yet. None of the current mathematical models could quantitatively explain this case. This is still an open question waiting to be solved.

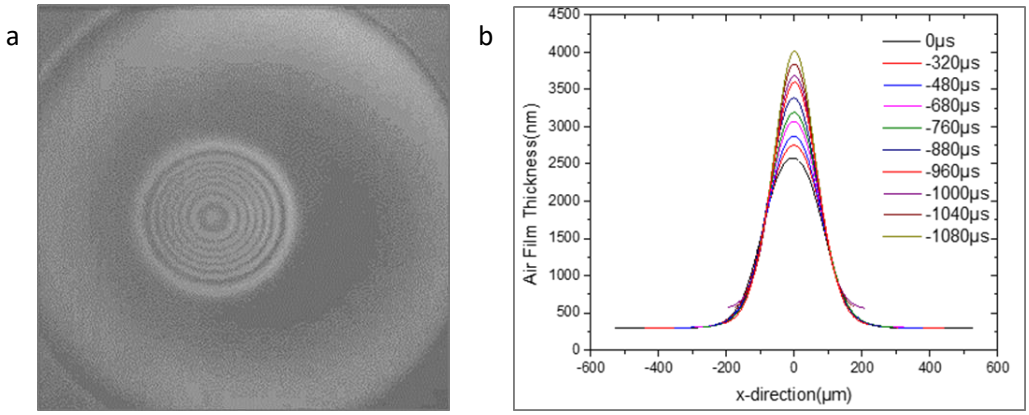

Figure 3-7. Air disk when the Weber number is about 2.0. a) Air disk observed from the bottom view camera. b) Profile of air disk evolution.

This section shows the experimental results of the neutral liquid droplets impact on the flat smooth surface. The results show decent agreement with previous research. This means that our experimental setup and measurements are reliable and accurate enough. The droplet deformation before impact has been verified from both side view camera and bottom view camera. To further understand the deformation during impact process, the impact dynamics of the metal droplets will be discussed in the next section.

3.3 Neutral Metal Droplet Impact

The deformation of the liquid droplet has been verified in Section 3.2, which shows agreement with previous research. For the melted metal, which has larger surface tension, viscosity and density, the impact dynamics might be different. I used the Pb-Bi alloy and two kinds of metal droplet generators introduced in Chapter 2 to generate droplets. The high-speed visualization method and experimental setup are the same with neutral liquid droplet impact.

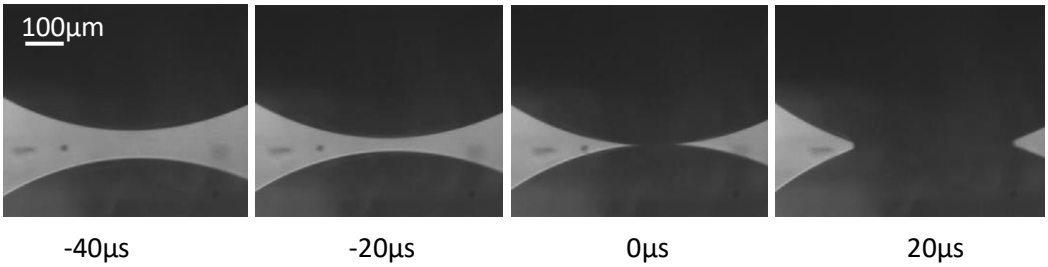

Figure 3-8. Side-view of metal droplet impact. The diameter is about 4.2mm and the impact velocity is 0.45 m/s.

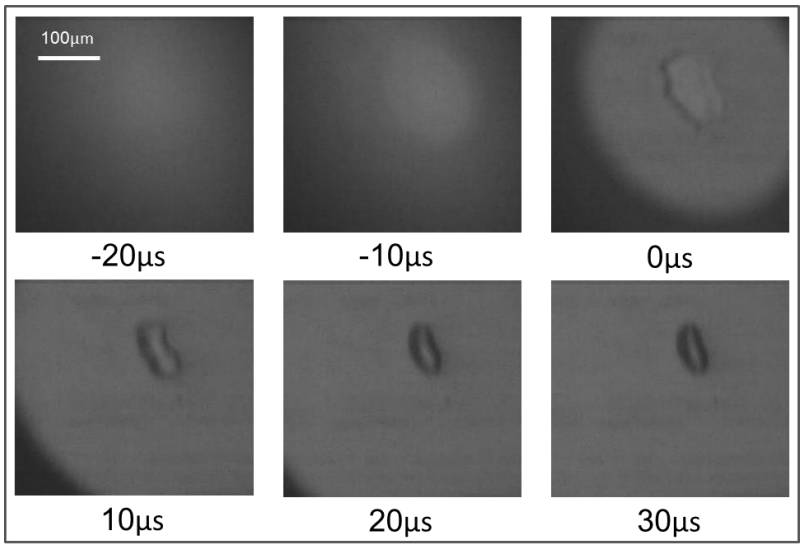

Figure 3-9. Bottom-view of neutral metal droplet impact on glass.

Due to the higher surface tension and larger viscosity of liquid metal, the deformation of metal should be more difficult than water or ethanol. The density of the Pb-Bi alloy that I used is about $\mathbf{8.86 \times 10^3}$ kg/m^3, and the surface tension is 0.42 N/m. From Fig. 3-8, there is no obvious deformation observed from side view camera. Based on previous experimental experience, fringes captured from bottom view is more accurate to determine the deformation. However, bottom view images of the metal droplet do not show any fringes. This is caused by the high reflection of metal droplet surface. For common light interference fringes, the reflected lights on different surfaces

need to be comparable with each other to form the bright and dark fringes. If one of the reflection is much greater than the other, there will be no fringes anymore. For the metal droplet, the liquid surface can be considered as complete reflection. The reflected light is much greater than the light reflected from glass. As a result, it is hard to observe any interference fringes under the metal droplet. Even though the deformation on metal droplet can not be confirmed with interference fringes, the air bubble can still be captured from bottom view images. It can be noticed that the air bubble retract slightly from 0 μs to 30 μs. During the 30 μs, the metal droplet is also solidifying, preventing further retraction. The solidification also makes the air pressure under the droplet a little lower than ambient pressure. When trying to peel off the solidified droplet from the substrate, the resistance caused by the pressure difference can be obviously felt.

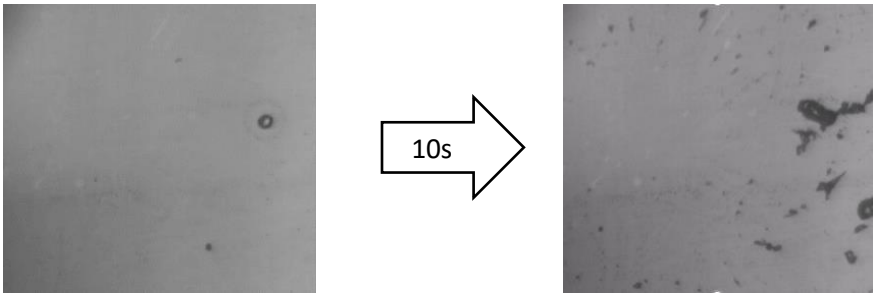

Figure 3-10. Cracking observed during the solidification of the Pb-Bi alloy on glass.

Initially, I expected to be able to peel the solidified droplet off the substrate and see a single pinhole at the center of the bottom surface. However, the bottom surface is actually very rough. By using the camera observing from the bottom view, I recorded the cracking of bottom surface during the process of solidification, as shown in Fig. 3-10. I believe that this problem is related to the structure of the atomic crystal, which is difficult to avoid. Although the cracking makes it

difficult to verify the air bubble after solidification, Fig. 3-9 & 3-10 have already shown clearly that an air bubble is entrapped under metal droplet.

3.4 Charged Liquid and Metal Droplet Impact

In Section 3.2 & 3.3, air bubble entrapment is observed during the droplet impact process, no matter the droplet is liquid droplet or metal droplet. The only exception that no bubble is observed is when impact velocity is very low ($We < 0.5$). Even for the low impact velocity case, the droplet deformation is still confirmed via fringes captured from the bottom view camera. In this section, the dynamics of the charged droplet will be demonstrated in detail. The air film profile under impacting charged droplet will be the focus in this section.

With the experimental setup introduced in Chapter 2, the droplet can be charged with the desired charge amount, and the charge amount can be measured and verified in three ways. The substrate is ITO coated glass to provide both conductivity and transparency. The charge amount in the droplet is increased gradually to study the influence of the charge amount until the change of air film profile can be obviously observed from side view.

The sizes and impact velocities of charged droplets are the same with neutral droplet shown in Section 3.2 to compare the difference. As shown in Fig. 3-11, there is a very obvious cone in the frame of -10 μs. Before contact to the substrate, the droplet bottom surface gains an additional speed of about 1 m/s compared with its neutral counterpart. This value is consistent with the pre-coalescence of two oppositely charged droplets being brought together[69]. More importantly, the charged droplet bottom surface forms a cusp and makes center touchdown without trapping any gas, in direct contrast to the flattened neutral droplet.

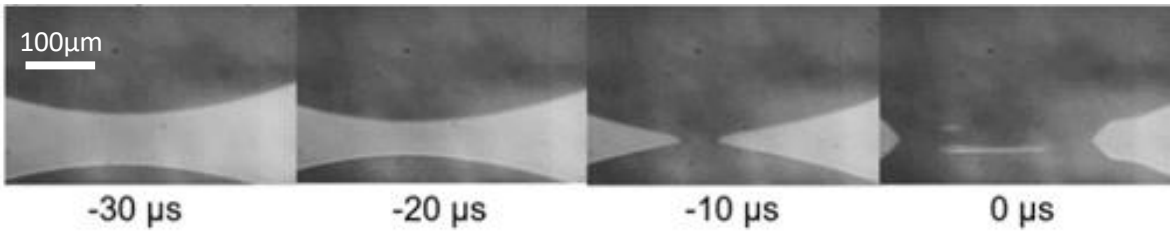

Figure 3-11. Side-view images of typical impact behavior of charged droplet with a charge of 6.3×10^{-11} C. The droplets have the same impacting velocity of 0.6 m/s and the radius of curvature of 1.25 mm before impact**.**

The images captured from the bottom view camera is also different from the neutral droplet. The light interference fringes could not be observed under highly charged droplet. For charged droplet, the bottom view images show the expansion from a dark point to the entire observation area, as shown in Fig. 3-12. The expansion of the dark area indeed represents the wetting process that starts from the center point and the contact line moves outwards. Both the side view images and bottom view images indicate that enough charge level in droplets can prevent the entrapment of air bubble.

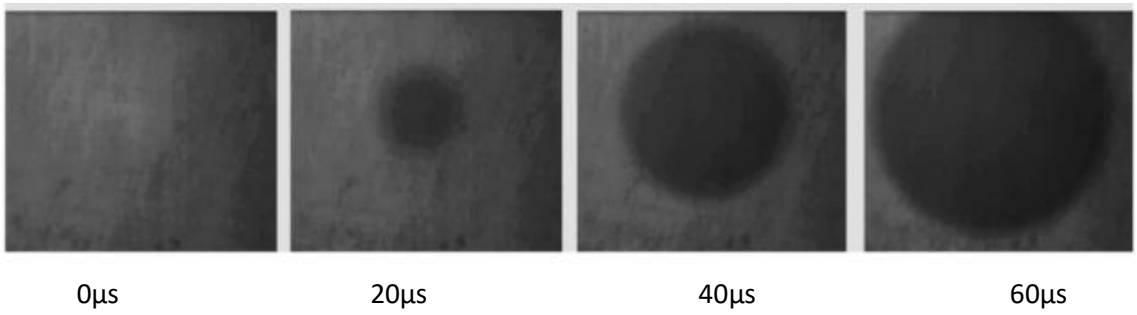

Figure 3-12. Bottom-view images of typical impact behavior of charged water droplet with a charge of 6.3×10^{-11} C. The droplets have the same impacting velocity of 0.6 m/s and the radius of curvature of 1.25 mm prior to impact.

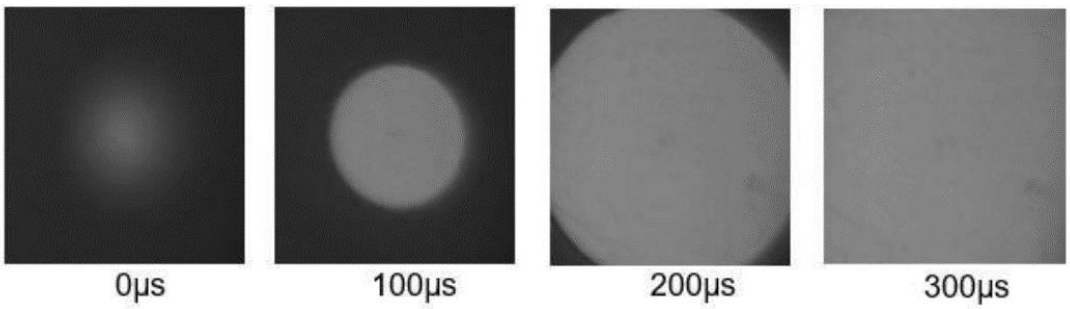

Figure 3-13. Bottom-view images of typical impact behavior of charged metal droplet with a charge of 1.4×10^{-10} C. The droplets have the same impacting velocity of 0.8 m/s and the radius of curvature of 1.75 mm before impact.

Similar cone-shape wetting expansion can also be observed when charged metal droplets carry enough charges. Like neutral metal droplet, due to the reflection of the metal surface, the bright area indicates the wetting area in Fig. 3-13. Clearly, there is no air bubble entrapped when the charged metal droplet impacts the ITO glass.

Fig. 3-12 & 3-13 have shown that the electric stress can fundamentally change the air film upon millimeter droplet impact on a flat surface. The question is whether electric stress can have a similar influence on smaller droplets. Hence, droplets generated from DoD device are also charged to figure out the influence of charges. The bottom view of a small charged water droplet impact on a flat surface is shown below in Fig. 3-14. The diameter of the small droplet is about 280μm. Similar to the large droplet, the droplet wetting starts from a small dark point and moves outwards, showing no evidence that there is an air bubble. However, unlike large droplet, fringes can also be noticed for the small charged droplet surrounding the wetting area, which means the displacement of deformation is relatively small compared to millimeter droplets.

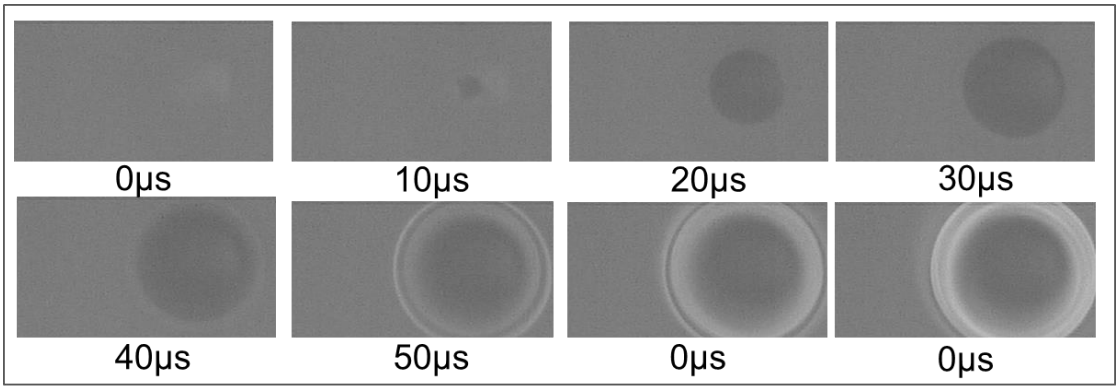

Figure 3-14. Bottom-view of charged droplet impact on ITO glass. The diameter of the droplet is 280 μm, the impact velocity is 0.89m/s.

As discussed in this section, charged droplets might form cone-shape deformation due to Maxwell stress. Sufficient charges carried by a droplet can result in electric stress overcoming lubrication pressure and Laplace pressure, forcing the droplet to deform. The cone-shape deformation makes the wetting process start from the center of the droplet, ensuring that no air be entrapped under the droplet.

3.5 Neutral and Charged Droplet Impact Model

The impact dynamics of neutral and charged droplets has been introduced from Section 3.2 to Section 3.4. The main reason causing the different deformations of neutral and charged droplets is believed as the competition of Maxwell stress and lubrication pressure. To fully verify and explain the physics behind the deformation, mathematical equations are derived to express the Maxwell stress and lubrication pressure in this section.

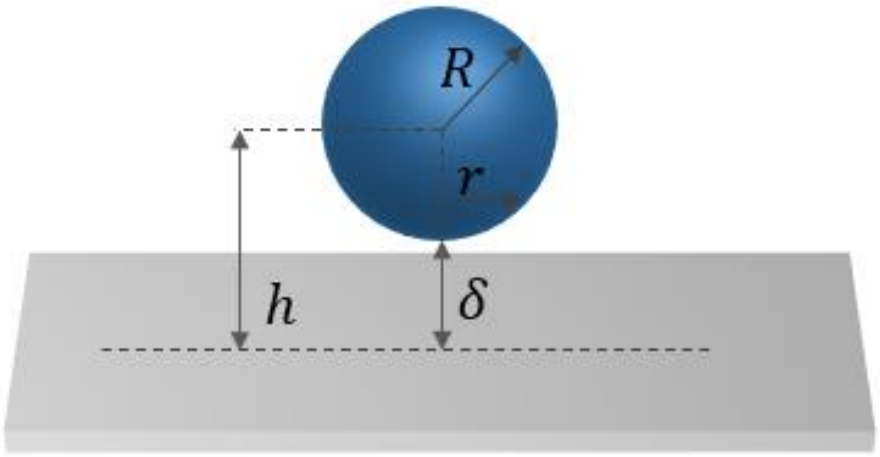

Figure 3-15. Schematic of neutral droplet impact on solid surface.

When droplet impact on the flat smooth surface, the air gap between them can be considered as a lubrication film with little variance in film thickness. The pressure distribution within the lubricating film can be obtained from the Reynolds equation for squeeze conditions, written in dimension form as

$$\frac{\partial}{\partial \mathrm{x}}\left(\frac{\rho h^3}{12\mu}\frac{\partial p}{\partial x}\right)+\frac{\partial}{\partial \mathrm{y}}\left(\frac{\rho h^3}{12\mu}\frac{\partial p}{\partial y}\right)=\frac{\partial(\rho h)}{\partial t} \qquad \text{Eq. 3-1}$$

where h is the distance from the substrate to the sphere, μ is the dynamic viscosity, p is the air pressure. The last term in the Eq. 3-1 represents the time dependent portion of the Reynolds equation. Since the droplet impact problem is an axisymmetric problem, the cylinder form of the Reynolds equation can be used

$$\boldsymbol{\frac{1}{r}\frac{\partial}{\partial r}\left(\frac{\rho h^3}{12\mu}r\frac{\partial p}{\partial r}\right)+\frac{1}{r}\frac{\partial}{\partial \theta}\left(\frac{\rho h^3}{12\mu}\frac{\partial p}{\partial \theta}\right)=\frac{\partial(\rho h)}{\partial t}} \qquad \text{Eq. 3-2}$$

For our experimental conditions, it is reasonable to assume the gas is incompressible. Hence, the gas density does not change. Also, the whole model is axisymmetric, the second term on the left of Eq. 3-2 can be ignored:

$$\frac{1}{r}\frac{\partial}{\partial r}\left(\frac{h^3}{12\mu}r\frac{\partial p}{\partial r}\right)=\frac{\partial h}{\partial t} \;\Rightarrow\; \frac{1}{r}\partial\left(\frac{h^3}{12\mu}r\frac{\partial p}{\partial r}\right)=\partial r\frac{\partial h}{\partial t} \qquad \text{Eq. 3-3}$$

Integrate both sides to get rid of the differentiation:

$$\frac{h^3}{12\mu}r\frac{\partial p}{\partial r}=\frac{1\partial h}{2\partial t}r^2 \;\Rightarrow\; \frac{\partial p}{\partial r}=\frac{6r\mu}{h^3}\frac{\partial h}{\partial t} \qquad \text{Eq. 3-4}$$

Here *h* is a function of *r*: $h=\delta+R-\sqrt{R^2-r^2}$, where *R* is the radius of the sphere. Substitute *h* into Eq. 3-4, the relationship between pressure *P(r)* and radius *r* can be calculated after integration:

$$P(r)=-3\mu\cdot\frac{\delta+R-2\sqrt{R^2-r^2}}{\left(\delta+R-\sqrt{R^2-r^2}\right)^2}\cdot\frac{\partial h}{\partial t}+C \qquad \text{Eq. 3-5}$$

where *C* is a constant depends on the boundary condition. If assume $P(r=R)=0$, the constant in Eq. 3-5 can be determined as

$$P(r)=-3\mu\cdot\frac{\delta+R-2\sqrt{R^2-r^2}}{\left(\delta+R-\sqrt{R^2-r^2}\right)^2}\cdot\frac{\partial h}{\partial t}-3\mu\frac{1}{R}V \qquad \text{Eq. 3-6}$$

For the case of a water droplet with 3.0 mm diameter and 1 m/s impact vlocity, the droplet will start to deform when the droplet is about 5μm away from the substrate [14]. As shown in the plot (Fig. 3-16), the highest pressure located at the center of the droplet. The maximum value is about 150 Pa, which is comparable to Laplace pressure of the droplet. The plot indicates that when

the droplet is 5μm away from the substrate, the lubrication pressure is capable of overcoming Laplace pressure to deform the droplet

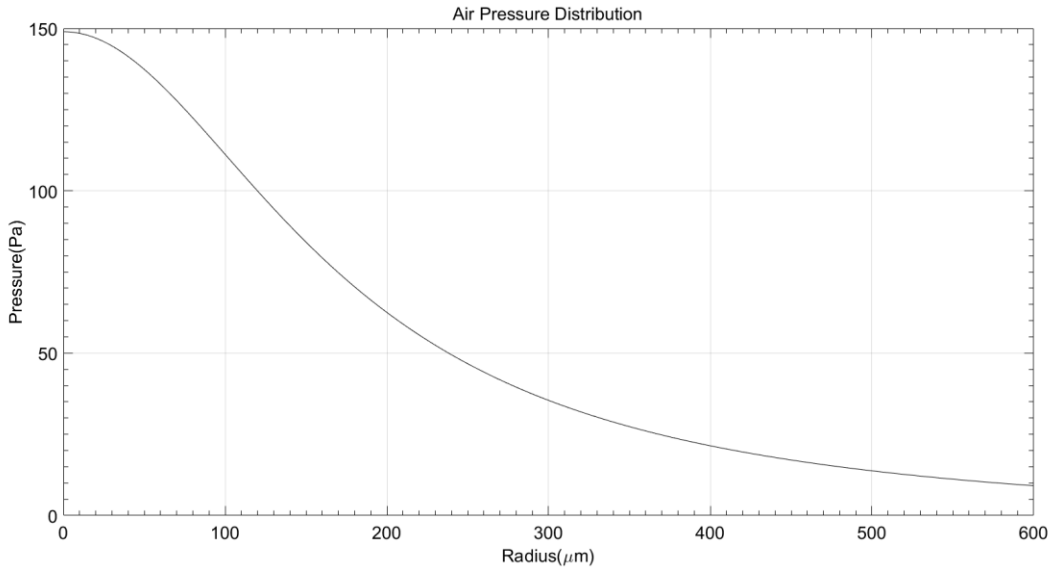

Figure 3-16. Example of the plot of pressure distribution along the direction of radius. The radius is 1.5 mm, impact velocity is 1m/s, and the distance between droplet and substrate is 5μm.

The method of mirror charges is used to calculate the electrical stress problem. Considering the liquid used in experiments, the droplet can be considered as a conductor. Charges can move freely and immediately if the external electric field is changed. When a charged droplet getting closer to the conductive substrate, the electric field comes from the charged droplet will induce charges to accumulate at the surface of the substrate. The induced charges form a new electric field that can affect the charge distribution in the droplet. Eventually, the electric balance between droplet and substrate will be reached. This method assumes that there is an image charge at the location of induction. This induced electric field makes the electrical potential of the droplet surface to be zero.

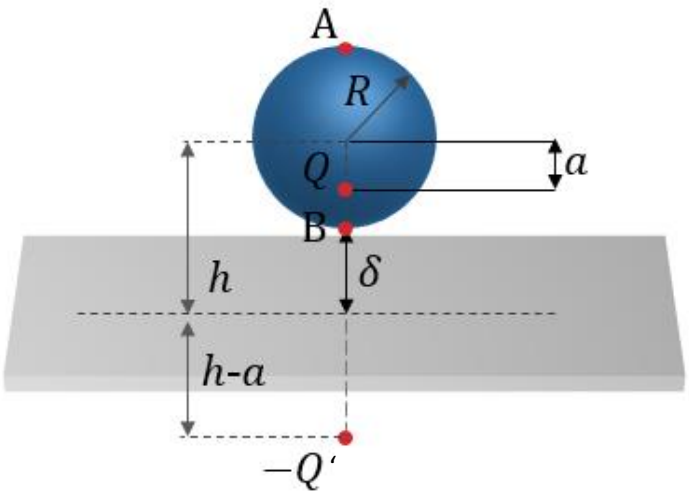

Figure 3-17. Schematic of mirror charge model for droplet.

A charged droplet can be considered as a whole body that charges concentrate at one point *Q*. In the mirror charge method, it is assumed there is a negative charge *–Q'* located at the symmetric location. Firstly, the electric potential at point A is:

$$\frac{1}{4\pi\varepsilon}\left(\frac{-Q\prime}{2h-R-a}+\frac{Q}{R-a}\right)=0 \qquad \text{Eq. 3-7}$$

While the electric potential at point B is:

$$\frac{1}{4\pi\varepsilon}\left(\frac{-Q\prime}{2h+R-a}+\frac{Q}{R-a}\right)=0 \qquad \text{Eq. 3-8}$$

Solving Eq. 3-7 & 3-8 together, the location of charge center is

$$a=\frac{2h-\sqrt{4h^2-4R^2}}{2}=h-\sqrt{h^2-R^2} \qquad \text{Eq. 3-9}$$

The distance between droplet and substrate can be expressed by $\boldsymbol{\delta = h - R}$. Hence, the charge center location can be calculated by:

$$\boldsymbol{a = h - \sqrt{h^2 - R^2} = h - \sqrt{R^2 + 2R\delta + \delta^2 - R^2} = h - \sqrt{2R\delta}} \quad \text{Eq. 3-10}$$

The location of droplet charge center and mirror charge center are all determined by the parameter of *a*. The electric potential for any point between the droplet and ground should be:

$$\boldsymbol{\varphi(D) = \frac{1}{4\pi\varepsilon}\left(\frac{-Q}{2h-D-a} + \frac{Q}{D-a}\right)} \quad \text{Eq. 3-11}$$

Based on the electric potential equation, the potential at the droplet surface is expressed by

$$\boldsymbol{\varphi(R) = \frac{1}{4\pi\varepsilon}\left(\frac{-Q}{2h-R-a} + \frac{Q}{R-a}\right) = 0} \quad \text{Eq. 3-12}$$

The electric field is the derivative of electric potential:

$$\boldsymbol{E(R) = \varphi'(R) = \frac{1}{4\pi\varepsilon}\left(\frac{-Q}{(2h-R-a)^2} - \frac{Q}{(R-a)^2}\right)} \quad \text{Eq. 3-13}$$

To substitute the parameter with the expression, the electric field is:

$$\boldsymbol{E(R) = \frac{-Q}{4\pi\varepsilon}\left(\frac{1}{\left(2h-h+\sqrt{2R\delta}-R\right)^2} + \frac{1}{\left(R-h+\sqrt{2R\delta}\right)^2}\right)}$$

$$\boldsymbol{= \frac{-Q}{4\pi\varepsilon}\left(\frac{1}{\left(\delta+\sqrt{2R\delta}\right)^2} + \frac{1}{\left(\delta+\sqrt{2R\delta}\right)^2}\right) = \frac{-Q}{4\pi\varepsilon R}\cdot\frac{1}{\delta}} \quad \text{Eq. 3-14}$$

The Maxwell stress based on the electric field can be calculated by:

$$\boldsymbol{\tau_{es} = \frac{1}{2}\varepsilon E^2(R) = \frac{Q^2}{32\pi^2\varepsilon R^2\delta^2}} \quad \text{Eq. 3-15}$$

At the center point of the droplet, where both the lubrication pressure and electric stress reach their maximum value, the lubrication pressure is expressed by

$$\boldsymbol{P_{air} = P(r = 0) = -3\mu \cdot \frac{\delta + R - 2\sqrt{R^2 - r^2}}{\left(\delta + R - \sqrt{R^2 - r^2}\right)^2} \cdot \frac{\partial h}{\partial t} = -3\mu \cdot \frac{\delta - R}{\delta^2} \cdot \frac{\partial h}{\partial t} = 3\mu \frac{R}{\delta^2} \cdot \frac{\partial h}{\partial t}} \qquad \text{Eq. 3-16}$$

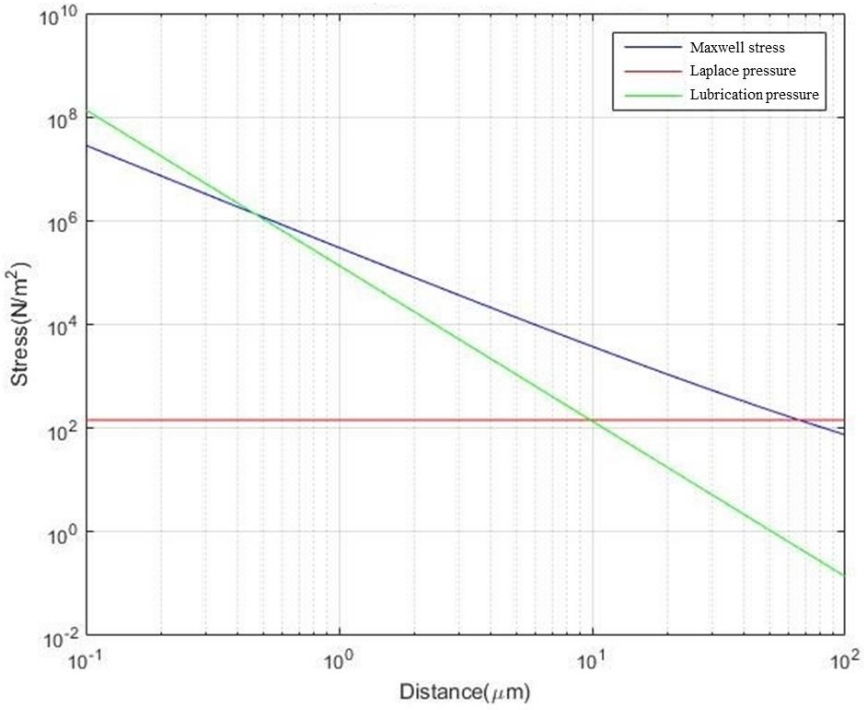

Figure 3-18. Example of the relationship between Maxwell stress, lubrication pressure, and Laplace pressure. The diameter of the droplet is 3 mm, impact velocity is 1 m/s, and the charge level is 2.0×10^{-11}C.

To compare the Maxwell stress and lubrication pressure, plot(Fig. 3-18) based on one of the experimental data was used. The diameter of the charged water droplet is about 3.0 mm. The impact velocity is about 1.0 m/s, the charge amount is about 2×10^{-11}C. In the plot, the Maxwell stress overcoming the Laplace pressure happens when the droplet is about 50 μm away from the

substrate, where the lubrication pressure can still be ignored. As a result, the droplet will deform into a cone-shape at the bottom. If the charge level is decreased to about 4×10^{-11} C and all the other parameters are kept the same as shown in Fig. 3-19, the lubrication pressure dominates the deformation by overcoming Laplace pressure, forcing the droplet to form a "dent"

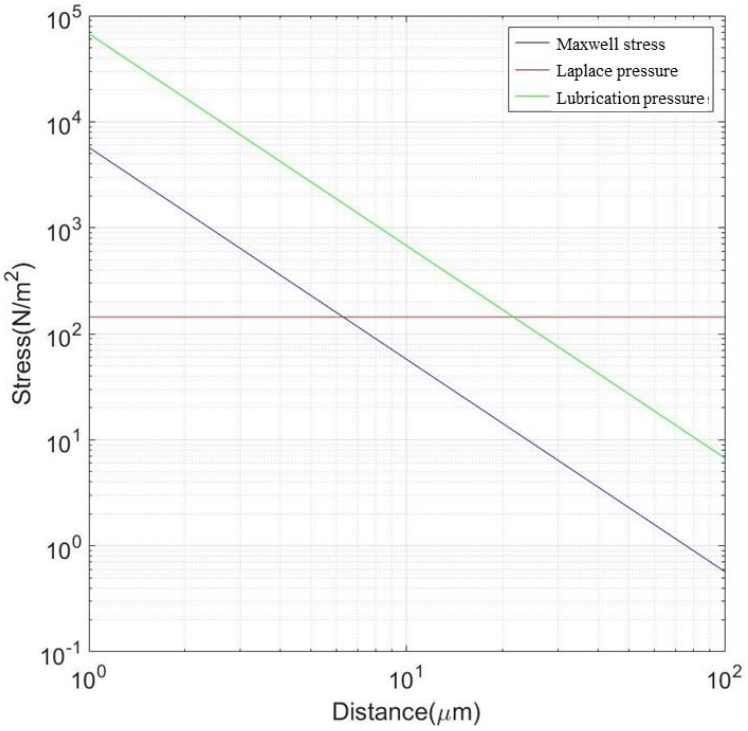

Figure 3-19. Example of the relationship between Maxwell stress, lubrication pressure, and Laplace pressure. The diameter of the droplet is 3 mm, the impact velocity is 1 m/s, and the charge level is 4.0×10^{-11} C.

3.6 Critical Charge Model

The dimple deformation under impacting neutral droplets and the cone-shape deformation under impacting charged droplet has been experimentally observed and numerically explained. As stated in Section 3.5, for the neutral droplet impact, the profile of the droplet bottom surface is

governed by a balance between droplet inertia and lubrication pressure[53, 99, 100]. For charged droplets, the additional Maxwell stress may become comparable to the lubrication pressure. The droplet would deform in different ways, depending on the charge level. In this section, the influence of the charge level on droplet deformation will be investigated and discussed.

To quantify the amount of charge, a dimensionless charge level is defined $\Gamma = q/qR$ as the ratio of actual charge q over the Rayleigh limit q_R, which describes the maximum charge a droplet can carry before the electric stress overcomes surface tension:

$$\boldsymbol{q_R = \pi\sqrt{64\varepsilon\sigma R^3}}, \qquad \text{Eq. 3-17}$$

where $\boldsymbol{\varepsilon}$ is the gas permittivity, $\boldsymbol{\sigma}$ is the surface tension, and $\boldsymbol{R}$ is the droplet radius.

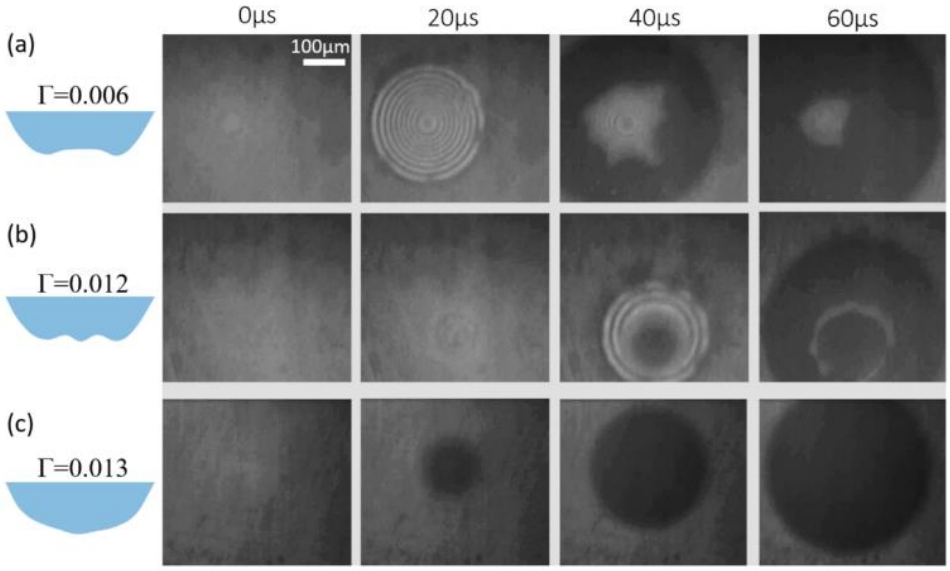

Figure 3-20. Bottom-view images for representative impacting conditions of different charge levels Γ. (a) Γ=0.006; (b) Γ=0.012; and (c) Γ=0.013. The shape of the droplet bottom surface is schematically illustrated on the left.

By changing the droplet charge level, three representative yet distinct air film structures are suggested by the bottom view of the impact process by varying charge levels (Fig. 3-15). At Γ = 0.006, the concentric circular interference fringes appear, and they are indistinguishable from the interference pattern of the typical impact of neutral droplets, suggesting that the air film is convex lens shape. At Γ = 0.013, the center contact appears, and the wetting area expands from the central spot to a growing dark circular disk. Notably, there exists a critical charge level (Γ = 0.012), at which an intermediate state can be observed: both the central dark wetted spot and circular fringes (40 μs in Fig. 3-15) are visible, and two concentric circular contact lines move toward each other.

Next, the amount of charge required to induce sufficient Maxwell stress to counter gas lubrication pressure is quantified. As discussed in Section 3.5, the curvature of the bottom surface of the droplet is determined by the competition between the Maxwell stress τ_M and the air film pressure P_g caused by the creeping gas flow. The charge relaxation time of the liquids tested is less than 1 μs, which is much shorter than the about 10 μs impacting event considered here, indicating the charge redistributes quickly enough prior to contact to maintain the droplet equipotential. Using the mirror charge model, the electric field at the bottom of the droplet is obtained:

$$\boldsymbol{E} = \frac{\boldsymbol{R}}{\boldsymbol{\delta}} \frac{\boldsymbol{q}}{\boldsymbol{4\varepsilon\pi R^2}} = \frac{\boldsymbol{R}}{\boldsymbol{\delta}} \boldsymbol{E_0} \qquad \text{Eq. 3-18}$$

where δ is the gap between the droplet bottom surface and the substrate, and E_0 is the surface electric field on a droplet with evenly distributed charge q. Eq. 3-18 suggests that as the charged droplet approaches a conducting plane, the electric charge is redistributed and becomes more concentrated on the droplet bottom surface. Therefore the electric field is locally intensified at the

bottom of the droplet by a factor of R/δ. For millimeter-sized droplet that is about 10 μm away from the substrate, this factor could be as large as about 100. As introduced in Chapter 1 and the derivation in Section 3.5, the Maxwell stress is:

$$\boldsymbol{\tau_M = \frac{1}{2}\varepsilon E^2 = \frac{1}{32\varepsilon}\frac{q^2}{\pi^2 R^2 \delta^2}} \qquad \text{Eq. 3-19}$$

Eq. 3-19 shows that Maxwell stress increases rapidly as the gap between the droplet bottom surface and the substrate decreases.

On the other hand, the air pressure buildup P_g tends to flatten the droplet and form a dimple. To analyze the lubrication pressure P_g, the air flow is assumed as incompressible because the luabrication pressure(about 10^5 Pa) is much smaller than the ambient pressure of 10^5 Pa. As the discussion in Section 3.5, the lubrication pressure can be expressed by

$$\boldsymbol{P_g = \frac{3\mu_g R}{\delta^2} U}, \qquad \text{Eq. 3-20}$$

Eqs. 3-17 and 3-20 suggest that both gas pressure buildup P_g and the Maxwell stress τ_M scale with the inversed square of gas film thickness $\delta(t)$. The critical charge q_c of the droplet is obtained by equating P_g and τ_M:

$$\boldsymbol{q_c = \pi\sqrt{96\mu_g \varepsilon R^3 U}}, \qquad \text{Eq. 3-21}$$

Hence the critical dimensionless charge level Γ_c is expressed by:

$$\boldsymbol{\Gamma_c = \sqrt{\frac{3}{2}Ca_g}}, \qquad \text{Eq. 3-22}$$

where $\boldsymbol{Ca_g = \mu_g gU/\gamma}$ is the capillary number based on the gas viscosity of μ_g, the impact velocity is $\boldsymbol{U}$ and the surface tension is $\boldsymbol{\gamma}$.

The impact dynamics is often characterized by the Weber number, which is a ratio between inertia and surface tension: $\boldsymbol{We = \rho U^2 D/\sigma}$, where ρ is the liquid density and D is the droplet diameter. For a representative case (impacting velocity: 0.25 m/s, droplet diameter: 3 mm, surface tension: 0.07 N/m, air viscosity: 1.8×10^{-5} Pa·s), We = 2.7, $Ca_g = 6.3\times10^{-5}$ and Γ_c is calculated to be only 0.01, or 1% of the Rayleigh limit. In other words, Eq. 3-8 suggests that a weakly charged droplet could overcome the gas film pressure buildup and change the gas film shape from convex into concave.

3.7 Discussion

One practical application closely related to this work is the droplet-based additive manufacturing, in which the air entrapment and bubble formation of the impacting droplet are often found but should be avoided[101]. For example, the gas entrapment of the deposition of molten aluminum is responsible for the pin-hole defect of the 3D printed parts[77]. The test of the impact of droplets of the Pb-Bi alloy shows that the neutral molten alloy droplet entraps gas and forms a pin-hole similar to that found in solidified aluminum droplet[77]. Once the molten alloy droplet is charged, center touchdown happens, and no gas entrapment is observed (Fig. 3-21). It suggests that charging the droplet may be an effective way to mitigate gas entrapment and pin-hole formation for 3D printing based on molten metals.

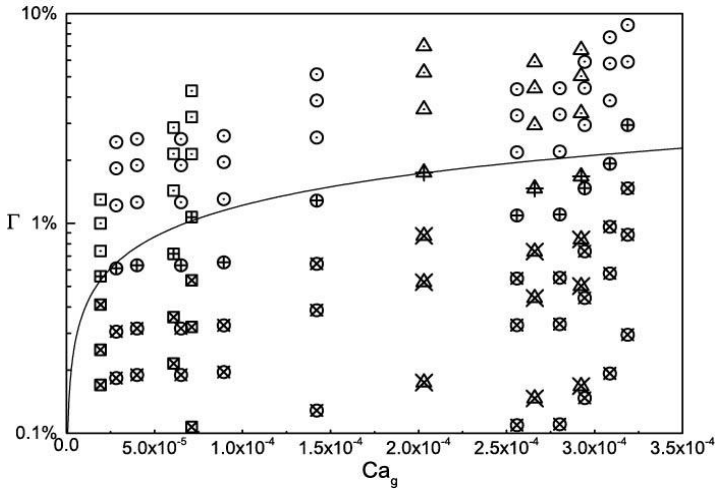

Figure 3-21. Experimental data vs. the critical charge level. The solid curve is the dimensionless critical charge level predicted by Eq.(8). Experimental data are obtained by impacting water, ethanol or Pb-Bi alloy droplets with different charge levels onto the ITO substrate. See Table 3-1 for data symbols.

Eq. 3-22 indicates that the critical dimensionless charge level is independent of droplet size. Using the DoD device, the size of the droplet is able to be changed by order of 10. I plot the data in Fig. 3-21, together with the critical dimensionless charge level (black solid curve) predicted by Eq. 3-22. The data are in quantitative agreement with Eq. 3-22 in the following ways: (i) the data points for the intermediate state are located near the solid curve; (ii) impacting droplets with center touchdown have charge levels higher than Γ_c predicted by Eq. 3-22; and (iii) the circular disk-shaped air film occurs for droplets charged below Γ_c. The detailed experimental data are shown in Table. 3-2. All the parameters are kept unchanged except charge amount in the drop to find the transient status between center conical and circular gas disk, which is called the critical charge level. The size of the droplet is also varied to verify that the critical charge level is not related to

the droplet diameter. Three different droplet sizes are tried, and they all show agreement with $\boldsymbol{\Gamma_c = \sqrt{3\,Ca_g/2}}$.

Table 3-1. Liquids used and some of their physical properties at room temperature (for water and ethanol) and 60 °C (for Pb-Bi alloy). Also given, the symbols used in FIG.5. (C.T.: center contact, I.S.: intermediate state, C.G.: circular gas disk).

Liquid	ρ (kg/m^3)	σ (N/m)	Symbols		
			C.T.	I.S.	C.G.
Ethanol	799	0.022	△	⟡	⧓
Water	1000	0.07	⊙	⊕	⊠
Pb-Bi alloy	8858	0.42	⊡	⊞	⊠

Further, because for a specific fluid Ca_g is proportional to $We^{1/2}$. Hence Eq. 3-22 suggests that Γ_c is proportional to $We^{1/4}$, indicating the critical charge level is a weak function of the Weber number. This was experimentally confirmed by varying Weber number by about 120 folds (from 0.5 to 62.9), and the critical charge level only varies by a factor of about 3.

Table 3-2. Experimental data of Figure 3-21.

	Diameter (mm)	Ca_g	Γ for disk-shaped gas film			Γ_c for transient gas film	Γ for conical contact		
water	2.8	2.82E-05	6.11E-04	1.83E-03	3.05E-03	6.11E-03	1.22E-02	1.83E-02	2.44E-02
	2.8	4.00E-05	6.32E-04	1.90E-03	3.16E-03	6.32E-03	1.26E-02	1.90E-02	2.53E-02
	2.8	6.50E-05	6.32E-04	1.90E-03	3.16E-03	6.32E-03	1.26E-02	1.90E-02	2.53E-02
	2.8	8.93E-05	6.53E-04	1.96E-03	3.27E-03	6.54E-03	1.31E-02	1.96E-02	2.61E-02
	2.8	1.42E-04	1.29E-03	3.86E-03	6.43E-03	1.29E-02	2.57E-02	3.86E-02	5.14E-02
	0.3	2.56E-04	1.09E-03	3.28E-03	5.46E-03	1.09E-02	2.19E-02	3.28E-02	4.37E-02
	0.3	2.80E-04	1.10E-03	3.31E-03	5.52E-03	1.10E-02	2.21E-02	3.31E-02	4.41E-02
	0.3	2.94E-04	1.47E-03	4.42E-03	7.37E-03	1.47E-02	2.95E-02	4.42E-02	5.89E-02
	0.3	3.09E-04	1.93E-03	5.79E-03	9.64E-03	1.93E-02	3.86E-02	5.79E-02	7.71E-02
	0.3	3.19E-04	2.95E-03	8.84E-03	1.47E-02	2.95E-02	5.89E-02	8.84E-02	1.18E-01
	0.3	3.50E-04	3.83E-03	1.15E-02	1.91E-02	3.83E-02	7.65E-02	1.15E-01	1.53E-01
Liquid eutectic alloy	4.2	6.09E-05	7.16E-04	2.15E-03	3.58E-03	7.16E-03	1.43E-02	2.15E-02	2.87E-02
	4.2	7.11E-05	1.07E-03	3.21E-03	5.36E-03	1.07E-02	2.14E-02	3.21E-02	4.29E-02
ethanol	0.3	2.03E-04	3.49E-02	5.24E-02	6.99E-02	1.75E-02	3.49E-02	5.24E-02	6.99E-02
	0.3	2.66E-04	2.94E-02	4.40E-02	5.87E-02	1.47E-02	2.94E-02	4.40E-02	5.87E-02
	0.3	2.92E-04	3.35E-02	5.03E-02	6.71E-02	1.68E-02	3.35E-02	5.03E-02	6.71E-02

It is worth noticing that most research efforts[67, 69, 77, 102-104] on regulating the impact dynamics and outcomes are focused on adjusting the surrounding gas pressure or by introducing micropatterns on substrates. For example, splashing suppression has been achieved by either

reducing air pressure[104] or using arrays of micro holes on substrates[103]; asymmetric microstructures are found to trigger directional splashing[76, 105-107], while hydrophobic micropillars cause discretely pinned contact lines and wetting[108]. In this work, the impact dynamics is fundamentally changed by altering the droplet charge level, without changing the substrate properties or gas environment. Moreover, I show that the small amount of charge at the droplet is sufficient to make the difference in impact dynamics. The weakly charged droplets studied here is different from the "self-explosion" of a suspended droplet, where either the charge is approaching the Rayleigh limit[109], nor the entire droplet is subject to intense external electric field[102], or the combination of significant charge level (13% of the Rayleigh limit) and strong electric field (about 10^6 V/m) [102]. It is also noticed that the studies on electrostatic suppression of Leidenfrost state[110-114] bear certain similarities with the present work because both phenomena involve the interaction of electrostatic stress and a thin gas layer. The key difference is that in the electrostatic suppression of Leidenfrost state, the lubrication pressure is sustained by the vapor flux from the rapidly evaporating drop, while in our work the lubrication pressure is due to impact. Such difference may become blurry for charged droplet impacting a substrate that is heated above the boiling point of the liquid. This would be an interesting topic for further investigation.

3.8 Conclusions

In summary, I found that a weakly charged droplet can entirely change the gas film structure during droplet impact on a flat smooth surface. As the charge level is raised above a critical level of about 1% of the Rayleigh limit for representative impact conditions, the Maxwell stress overcomes gas pressure buildup to deform the droplet bottom surface. A conical liquid tip

forms and pierces through the gas film, leading to a circular contact line moving outwards that does not trap any gas. The critical charge level only depends on the capillary number based on the gas viscosity. This new finding brings insights to practical applications such as eliminating gas entrapment for liquid droplet based material deposition, printing, and pesticide applications.

Chapter 4 Charged Droplet Impact on Special Surfaces

4.1 Introduction

The dynamics of neutral and charged droplets impacting on the flat smooth surface has been studied in Chapter 3. Experimental results indicate that a small amount of charges in a droplet (about 1% of Rayleigh limit) can fundamentally change the whole impact dynamics[115]. For neutral droplets, lubrication pressure under the impacting droplet can be strong enough to overcome Laplace pressure to deform the droplet when the distance between droplet and substrate is very small. As a result, a convex lens shape of air film is formed under the droplet. However, if a droplet carrying a little amount of charges impacts on a conductive surface, the convex lens shaped air film might be alternated to a concave shape. It is confirmed that the deformation of a charged droplet is the competition of Maxwell stress and lubrication pressure. Maxwell stress is caused by the interaction between the charges inside the droplet and induced charges in the substrate. In the discussion (Section 3.7), the conductivity of the substrate plays an important role during the droplet impact process. In this chapter, the influence of the substrate will be discussed. In contrast to the charged droplet impacting conductive and hydrophilic surface, the dynamics of droplet impact on dielectric surface and the hydrophobic surface is studied and discussed.

The phenomenon that charged droplets impact on dielectric surface actually happens in daily life because the electric charges are often found in naturally or artificially formed droplets. Lord Kelvin found out that spontaneous charging of droplets happens when water droplets pinch-off from liquid, such as waterfall[97]. Millimeter-sized raindrops in nature can carry up to about 1.0×10^{-10} C of positive or negative charges is discovered by Smith[98]. These naturally

generated charged droplets will eventually impact on conductive or dielectric natural substrates. Some inkjet printers also rely on charges to select and steer droplets to the desired location on paper or poster, which is an example of artificial charged droplet impact on dielectric surfaces.

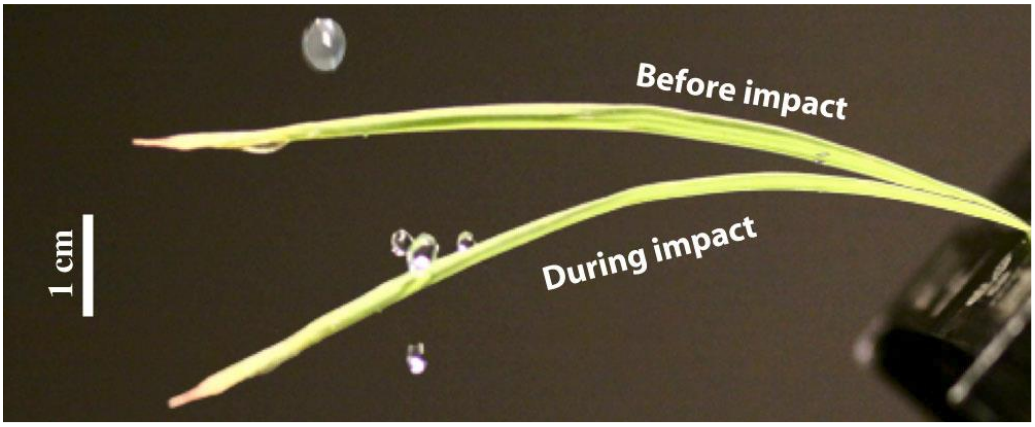

Figure 4-1. Side view of the water drop impact on a natural leaf in the lab. The figure is reproduced from Reference[116] with permission from APS.

On the other hand, droplets impact on the hydrophobic surface is also an interesting phenomenon that happens in real life. A typical example is water droplets impact on natural leaves (Fig. 4-1). Since the surfaces of most leaves in nature are more or less hydrophobic and flexible, impact droplets will bounce and splash away from the leaves. Just a very little amount of droplets can incidentally stay on the surfaces of leaves. The bad wettability of leaves can result in waste when pesticide spraying. It is reported that more than 50% of agrochemicals are lost because of undesired bouncing and splashing when pesticide spraying[117]. The bouncing and splashing of pesticide droplet can even affect the soil quality as well. As shown in Fig. 4-2, droplet would bounce or splash on hydrophobic surfaces. It is very difficult to avoid the bounce or splash.

However, considering charges in droplets can affect the impact dynamics, it is highly possible that charges can also influence the impact dynamics of droplets on hydrophobic surfaces.

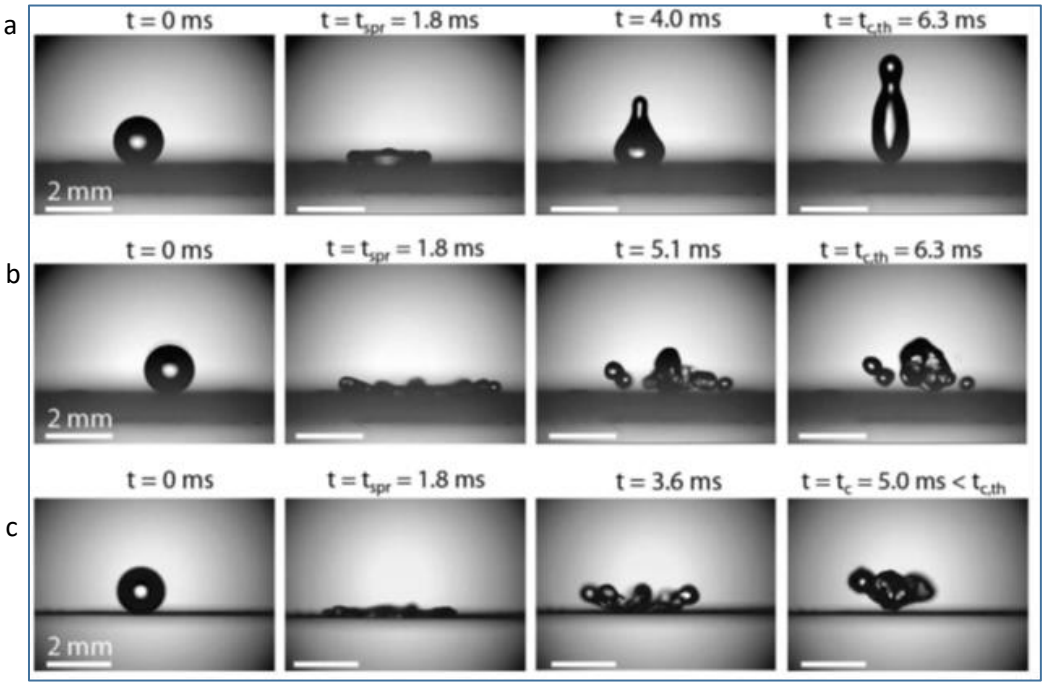

Figure 4-2. Side view of water drop bounce and splash on different surfaces. a) low velocity droplet(v=0.68m/s) impacting rigid superhydrophobic surface, b) higher impact speeds (v=1.58m/s) impacting rigid superhydrophobic surface c) higher impact speeds (v=1.57m/s) impacting elastic superhydrophobic surface. The figure is reproduced from Reference[118] with open access from Nature Research.

In this chapter, the electrical effect of the droplet on dielectric surfaces and hydrophobic surface are experimentally investigated separately.

4.2 Charged Droplet Impact on Dielectric Substrate

To study the dynamics of charged droplet impact on the dielectric substrate, both experimental and numerical research has been done and the results are shown in this section.

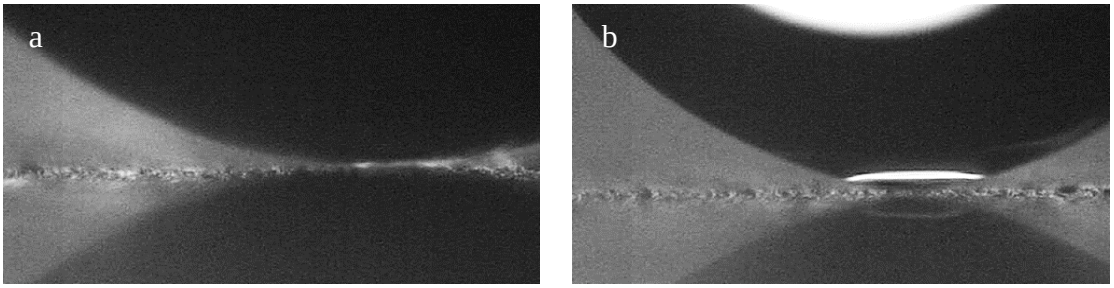

Figure 4-3. Side view of water drop impact on a 200μm thick glass slide. a) neutral droplet b)charged droplet with 2% dimensionless charge level.

Firstly, the dynamics of a charged droplet impact on dielectric surface was studied. Both the droplet generator and high-speed visualization are the same as introduced in Chapter 2. ITO glass covered by a dielectric layer is used as the substrate. The dielectric layer could be 2 μm thick SU-8 photoresist, 50 μm thick Kapton tape, 100 μm thick bare glass cover slid, 200 μm thick glass slide, or a 1mm thick bare glass slide. Counterintuitively, the dielectric layer does not change the impact behavior, i.e. the bottom of the droplet is still able to deform into a Taylor cones shape. Fig. 4-3 shows clearly the deformation of the neutral and charged droplet, very similar to Fig. 3-1 & 3-11. Images from the bottom view (Fig. 4-4 & 4-5) also indicate that the deformation is similar with the cases that the substrate is conductive.

Figure 4-4. Bottom view of neutral droplet impact on a 200μm thick glass slide.

Figure 4-5. Bottom view of charged droplet impact on a 200μm thick glass slide. The charge level Γ=2%.

The only difference is that for the dielectric layer, a higher charge level is required to form Taylor cones. This can be explained by the polarization effect induced by the approaching charged droplet, which is stated in Chapter 1. The polarization is a rapid process with a characteristic time of <0.01 μs[119], much faster than the impact process. Besides, the electric charge density is far less than the saturation limit of typical dielectric media [120]. The quantitative explanation is too complicated to develop. Instead, a simplified numerical simulation in COMSOL is developed to validate the experimental results. Fig. 4-6 shows an example of the COMSOL simulation results. The droplet diameter is 3.0 mm, the substrate thickness is 100 μm. Based on the experimental results, the droplet forms cone-shape above 100 μm thick Kapton when the charge level is as large

as 7 to 10 times greater as above ITO coated glass. The charge level is also dependent on the electrical permittivity of the substrate. The results show agreement with the experimental results.

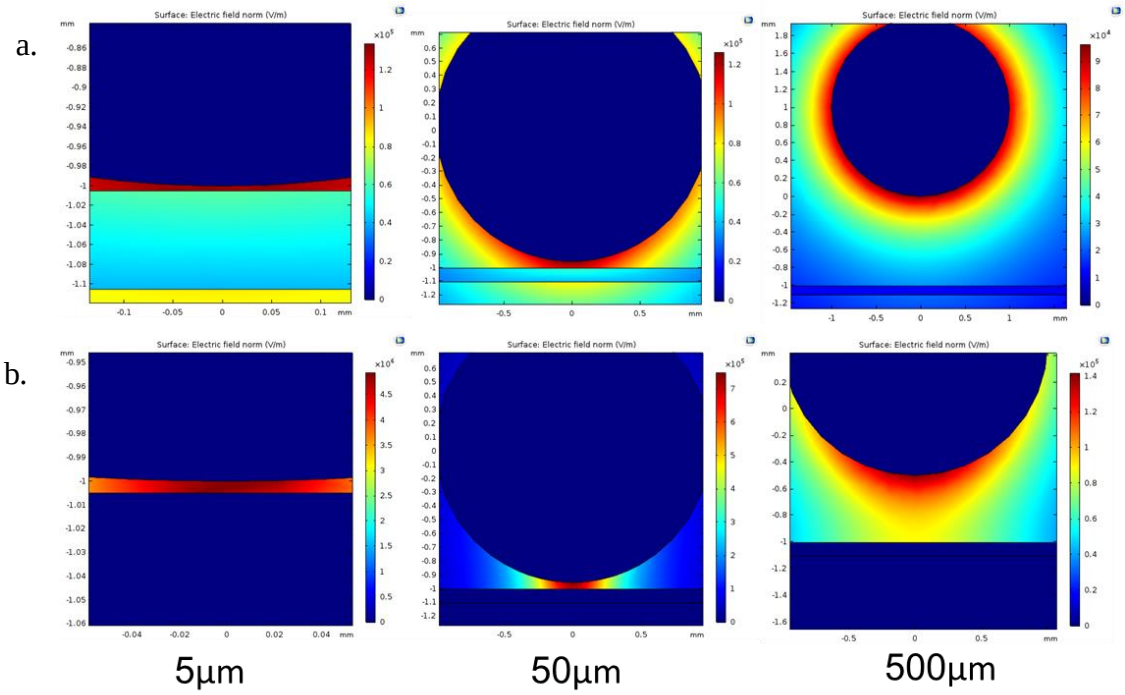

Figure 4-6. COMSOL simulation of the electric field of different distances while water droplet impact on a 100μm thick substrate. a) Substrate is dielectric glass. b) Substrate is conductive glass.

To quantitively study the strength of the electric field and the Maxwell stress induced by the electric field, I used a simplified mirror charge model to analyze. Similar to the mirror charge method used in a conductive substrate, a charge center is assumed at the other side of the substrate surface with the opposite charges. For a conductive surface, the charge amount induced in the mirror equals to the charge amount carried by the droplet. However, for dielectric substrate, the mirror charge on the substrate surface induced by polarization is[120]:

$$q' = q(1 - k)/(1 + k) \qquad \text{Eq. 4-1}$$

where k is permittivity ratio of $\boldsymbol{\varepsilon_s/\varepsilon}$, $\boldsymbol{\varepsilon}$ is the permittivity of air, $\boldsymbol{\varepsilon_s}$ is the permittivity of the substrate, and q is the charge amount inside the droplet. According to the charge amount and location, the induced electric field E' is expressed by:

$$\boldsymbol{E' = E \cdot k/(1+k)} \qquad \text{Eq. 4-2}$$

Maxwell stress $\boldsymbol{\tau'_M}$ caused by the electric field can be calculated by:

$$\boldsymbol{\tau'_M = \frac{1}{2}\varepsilon E'^2 = (\frac{k}{1+k})^2 \tau_M} \qquad \text{Eq. 4-3}$$

Eq. 4-3 shows that Maxwell stress induced from the dielectric surface only has an extra coefficient compared to conductive surface. For Kapton film, the permittivity ratio k is about 3. If the substrate is glass, the permittivity ratio of k is about 10. Therefore, the Maxwell stress over Kapton is about half of the Maxwell stress over ITO glass. For glass, the value of $\boldsymbol{(\frac{k}{1+k})^2}$ is about 1. This means that when the droplet is close to the glass, the value of Maxwell stress should be almost the same.

Considering a charged droplet impact on a dielectric surface, the charges inside the droplet would not be relaxed immediately after the droplet touches the substrate. Instead, the droplet may even carry the charges for a long time during the spreading. The charges carried inside the droplet maybe could affect the wetting speed. To verify this assumption, the wetting speeds of charged water droplets on ITO coated glass and on a standard glass are measured. The data are recorded in Table. 4-2. As shown in the table, for the same charge level, wetting speed of charged droplet on glass is faster than on ITO as expected. Also, after 40μs spreading, the speed loss on glass is significantly less than ITO-glass. This difference can be explained by the influence of the charges

carried by the droplet. The electric stress can keep attracting the droplet to wet the surface. Moreover, this can also be considered as a kind of electrowetting. The charges in droplet might change the surface tension of the droplet, leading the droplet to wet the surface.

Table 4-1. Simulation results of electric field over substrates with different conductivity.

$Q = 1.0 \times 10^{-11} C$	Glass substrate			Conductive substrate
	substrate thickness	$\varepsilon = 4.3$	$\varepsilon = 10$	
0μm distance between substrate and droplet	50μm	$9.4 \times 10^5 V/m$	$1.3 \times 10^6 V/m$	$1.75 \times 10^6 V/m$
	100μm	$6.9 \times 10^5 V/m$	$1.1 \times 10^6 V/m$	
	500μm	$3.4 \times 10^5 V/m$	$6.8 \times 10^5 V/m$	
	1000μm	$2.9 \times 10^5 V/m$	$6.1 \times 10^5 V/m$	
50μm distance between substrate and droplet	50μm	$3.9 \times 10^5 V/m$	$4.3 \times 10^5 V/m$	$4.61 \times 10^5 V/m$
	100μm	$3.5 \times 10^5 V/m$	$4.0 \times 10^5 V/m$	
	500μm	$2.3 \times 10^5 V/m$	$3.2 \times 10^5 V/m$	
	1000μm	$1.9 \times 10^5 V/m$	$3.0 \times 10^5 V/m$	
100μm distance between substrate and droplet	50μm	$2.5 \times 10^5 V/m$	$2.6 \times 10^5 V/m$	$2.68 \times 10^5 V/m$
	100μm	$2.3 \times 10^5 V/m$	$2.5 \times 10^5 V/m$	
	500μm	$1.7 \times 10^5 V/m$	$2.2 \times 10^5 V/m$	
	1000μm	$1.5 \times 10^5 V/m$	$2.0 \times 10^5 V/m$	

Table 4-2. Comparison of wetting speed between the conductive surface and dielectric surface.

	ITO-substrate			Glass substrate	
Charge Level	1%	2%	3%	2%	3%
Wetting Speed (0-10μs)	1.94m/s	2.36m/s	2.20m/s	2.37m/s	3.14m/s
Wetting Speed (10-20μs)	1.90m/s	1.29m/s	1.67m/s	2.62m/s	2.17m/s
Wetting Speed (20-30μs)	1.63m/s	1.52m/s	1.44m/s	1.71m/s	2.22m/s
Wetting Speed (30-40μs)	1.25m/s	1.14m/s	0.65m/s	1.82m/s	1.88m/s
Speed Loss	36%	52%	70%	23%	40%

According to the discussion above, as long as the droplet carries enough charges, the droplet would always deform into a cone shape at the bottom when a droplet impact on a solid substrate, no matter the conductivity of the surface. I would like to further explore the charged droplet impact on the liquid surface. For droplet impact into surface pool, the bottom view high-speed camera could not capture any images. However, the side view can still capture the droplet impact process. As shown in Fig. 4-7, although the water layer is dielectric, the impact of charged droplets can still form a Taylor cone. Moreover, in the last 2 frames (60 μs & 80μs), the liquid pool also deforms to a little cone shape. The dynamics of charged droplet impact into the liquid pool is similar to the coalescence of two conical droplets[69].

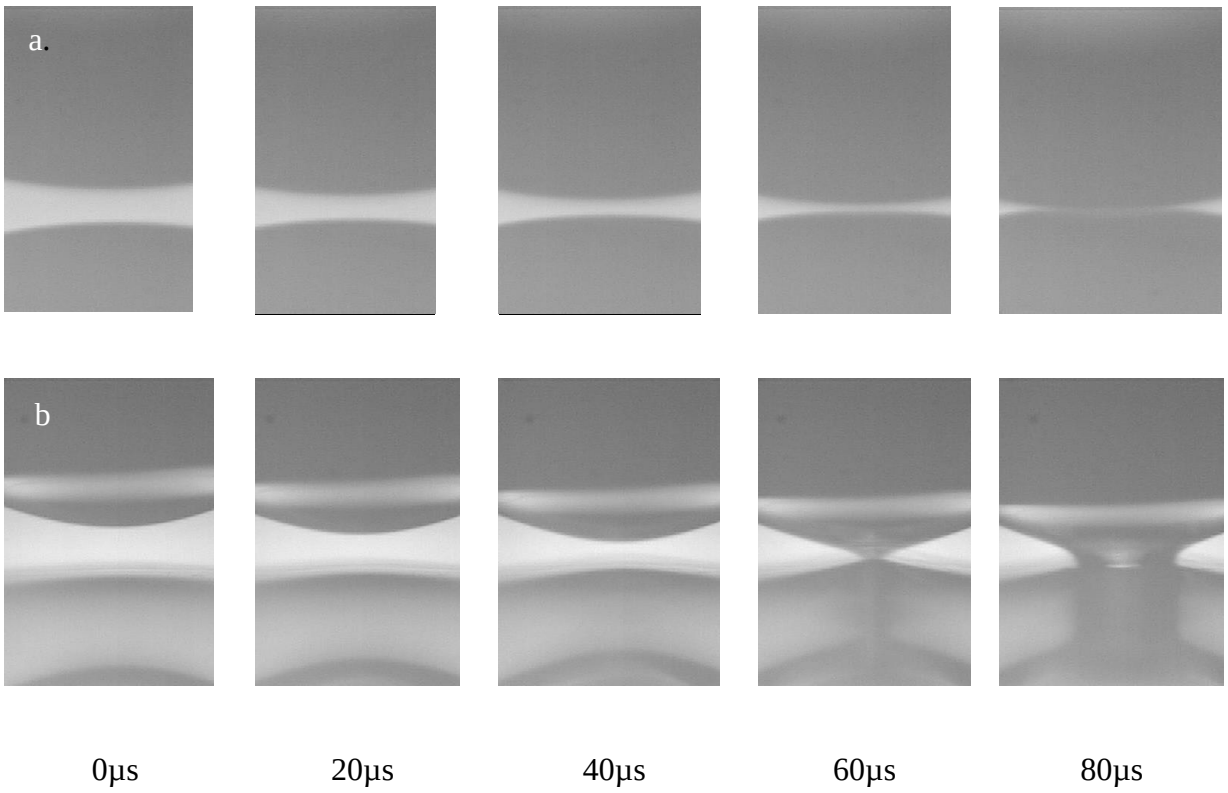

Figure 4-7. Neutral and charged droplet impact into a liquid pool. a) A bright gap observed when neutral droplet impact into liquid pool. b) A cone shape observed when charged droplet impact into liquid pool.

4.3 Charged Droplet Impact on Hydrophobic Surface

Since the conductivity of the substrate does not affect the deformation of droplets. I would like to further explore the influence of substrate wettability. Fluoro-polymer (FluoroPel PFC M1604V) spin-coated glass slide are used as the substrate. The contact angle can be adjusted up to 168° by adjusting the parameters of spin coater. As a contrast, the lotus leaf is the most hydrophobic leaf in nature that the contact angle is about 149°. The spin-coated superhydrophobic surface is shown in Fig. 4-8. In the experiments, when charge level is greater than the critical value,

the droplet would still deform when the impact on a hydrophobic surface. This is easy to understand. Droplet deformation happens before wetting starts. Surface wettability does not have any influence on the electric field or air pressure. As a result, as long as the electric stress is strong enough to overcome the surface tension and air pressure, the droplet will deform to a cone shape..

a. b.

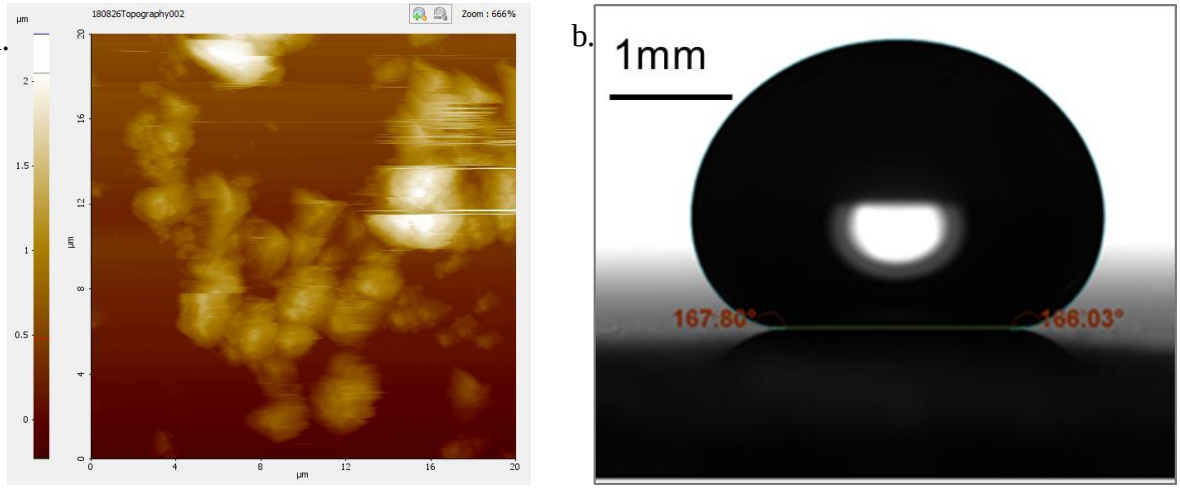

Figure 4-8. Spin-coated superhydrophobic surface. a) Hydrophobic surface under AFM. b) 168° contact angle is measured.

As stated in Section 4.1, the bouncing and splashing on hydrophobic surfaces are very difficult to prevent. To further study the electric effect on bouncing, contact time can be used to quantify. Typical bounce includes the whole process of impacting, spreading, recoil, and lift-off (Fig. 4-9). This mechanism is governed by the inertial-capillary-scaled contact time (so-called the theoretical contact time)[118]:

$$t_{c,th} = 2.6\sqrt{\frac{\rho D_0^3}{8\gamma}} \qquad \text{Eq. 4-4}$$

where ρ is the droplet density, D_0 is the diameter of the droplet, and γ is the surface tension of droplet. It is surprising that the contact time is not related to impact velocity, but this has been experimentally proved to be correct. Current research related to contact time mostly focuses on reducing contact time [118, 121], the only method reported to increase the contact time is to add a small amount of a double-chain vesicle surfactant[117].

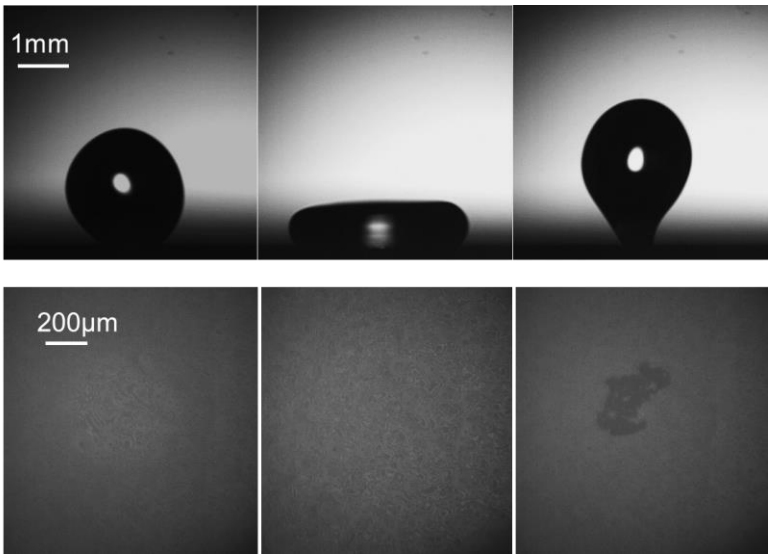

Figure 4-9. Droplet impact on a hydrophobic surface. The droplet diameter is 2.66 mm, the impact velocity is 0.46m/s.

To observe the contact, side view and bottom view high-speed visualization technology can also be utilized (Fig. 4-9). As shown, because the surface is superhydrophobic, the bottom view could not clearly show the contact status of the droplet. Hence, during the experiments, contact time is measured by using side view images. When impact velocity is relatively fast, the charges in a droplet can increase the contact time. Table 4-3 shows that 10% charge level can increase about 40% of contact time.

Table 4-3. Comparison of wetting speed between the conductive surface and dielectric surface. Droplet diameter is 2.80 mm, impact velocity is 1.0 m/s.

Charge level($\times \mathbf{10^{-10}}\boldsymbol{C}$)	0	0.40	1.12	1.73
Dimensionless charge level	0	2.7%	5.7%	16.1%
Diameter(mm)	2.80	2.84	2.78	2.82
Contact time(ms)	22.1	22.4	24.0	26.4

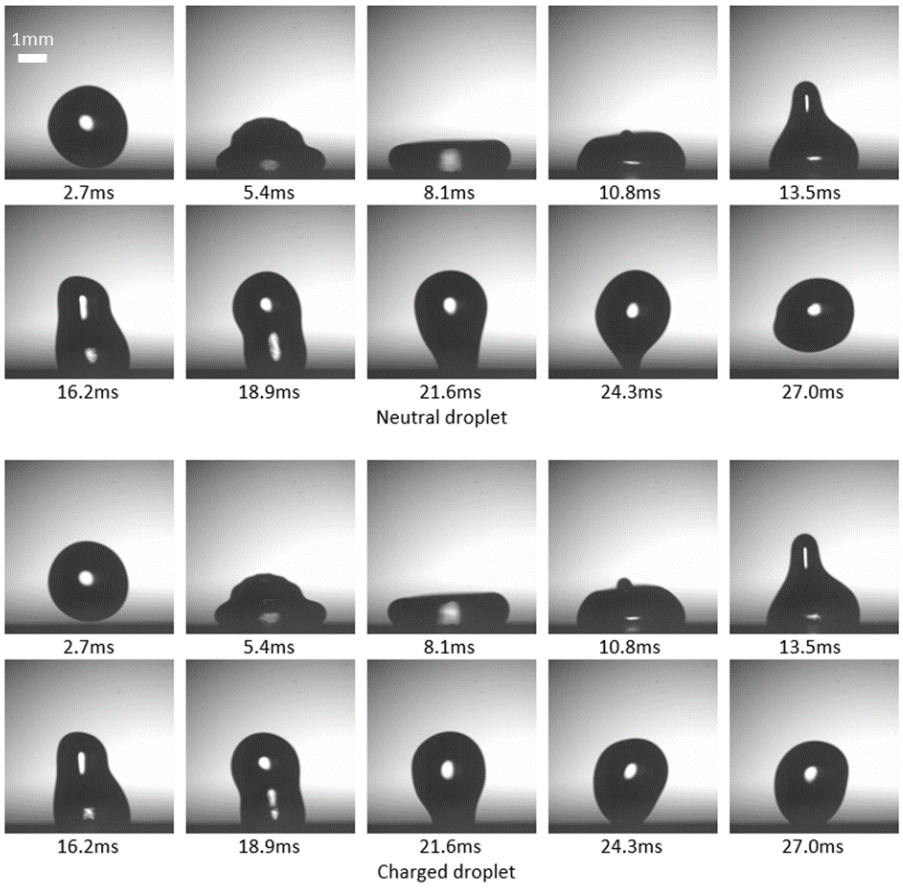

Figure 4-10. Neutral and charged droplet impact on the hydrophobic surface. The droplet diameter is 2.65 mm, and the impact velocity is 0.46m/s. Droplet is charged with 10% Rayleigh limit.

A significant influence of charges in droplets was observed when impact velocity is slow. As shown in Fig. 4-10, under some circumstances, bouncing and splashing on the hydrophobic surface can be totally avoided when the droplet carry enough charges. 10% of Rayleigh limit charge can hold the droplet on the hydrophobic surface without bouncing or splashing

4.4 Conclusions

In summary, it is found that the electric stress can also influence the impact dynamics when the substrate is a dielectric material. It is verified that the dielectric substrate requires a higher charge level to deform compared to the conductive substrate. Because for dielectric surface, electric field and the electric stress are induced by polarization. The charge density induced from polarization is much less than charge density induced from a conductor. A theoretical equation to explain the electric effect is also provided.

On the other hand, charges in a droplet can alter the bouncing and splashing when droplet impact on hydrophobic surfaces. 10% charge level can significantly increase the contact time. For slow motion droplets, charges can even totally prevent the bouncing.

Chapter 5 Numerical Simulations

5.1 Introduction

In Chapter 3, I have experimentally studied the dynamics of neutral and charged droplet impact on a flat surface. The images captured from side view and bottom view cameras show that neutral droplets form convex lens shaped air film during the impact process. This deformation is caused by lubrication pressure of the air layer. Upon the droplet start to wet, the air film is entrapped and eventually retracts to a bubble. However, the impact dynamics can be fundamentally changed when the droplets are weakly charged. Sufficient charges in the droplet result in Maxwell stress overcoming the lubrication pressure, forcing the droplet to form a Taylor cone. Moreover, the critical charge level determines the deformation was discovered experimentally and analyzed theoretically.

The competition between Maxwell stress and lubrication pressure is concluded as the main cause of the deformation of charged droplets. To further verify this theory and further investigate the impact dynamics with different conditions, a numerical program is developed. The dynamics of droplet impact on solid surfaces has been numerically investigated before. There are basically two types of simulations of droplet impact. One of them is based on Navier-Stokes equations of two-phase flows, considering liquid and gas are fluids with different physical properties. They used methods like VOF model(Volume of Fluid method) [31], level set model[122, 123], moving mesh[124], or coupled of them[125] to track the interface between droplet and gas. This kind of simulations calculate the whole liquid-gas system to get more accurate results, but it requires to very long time and very powerful computational performance. The other kind of simulation pays

all attention to the air film layer instead of the whole system. The droplet is assumed to be an elastic sphere with no internal effects on the air film. This kind of method is easier to be solved by a computer, but only suitable for problems just care about the air film.

In this chapter, I choose the latter method because I just want to study the impact of droplet deformation under different circumstances. The algorithm will be discussed in detail, and the simulation results of the neutral and charged droplets impact on a flat surface will be compared to previous research and experimental results from Chapter 3.

5.2 Simulation of Neutral Droplet Impact

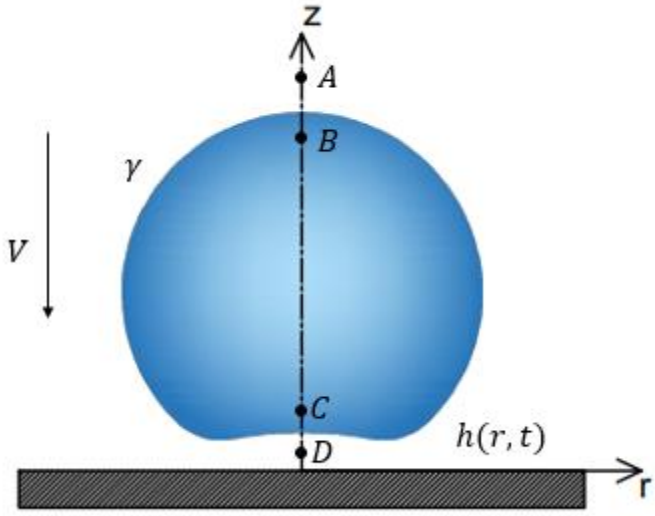

Figure 5-1. Schematic of the neutral droplet impacting on a rigid flat surface.

Neutral droplets impact on a rigid flat surface would result in a dimple deformation at the bottom. The deformation of impact neutral droplet has been introduced in detail in Chapter 3, which is caused by the air lubrication pressure overcoming Laplace pressure. Based on this theory,

Evert[126] built a simplified model to simulate the deformation during droplet impact. The method introduced in this section and the following is adapted from his work.

Firstly, the air film profile is defined by the cylinder form of the Reynolds lubrication equation (Eq. 3-4):

$$\frac{\partial h(r,t)}{\partial t} = \frac{1}{r}\frac{\partial}{\partial r}\left[\frac{r h(r,t)^3}{12\mu_g}\frac{\partial p(r,t)}{\partial r}\right] \quad \text{Eq. 5-1}$$

where $\boldsymbol{h(r,t)}$ is the air film profile, $\boldsymbol{\mu_g}$ is the viscosity of the gas, and *p(r,t)* is the pressure in the air film. Considering the air film is usually very thin (about 5μm), the pressure can be assumed to be consistent along the vertical direction. In Fig. 5-1, the *p(r,t)* refers to P_D. If P_A is the ambient pressure of p_0, the pressure at point be can be expressed by

$$\boldsymbol{p_B = p_A + \frac{2\gamma}{R} = p_0 + \frac{2\gamma}{R}} \quad \text{Eq. 5-2}$$

Because the top part of the droplet can still be considered as an ideal sphere. The pressure at point C can be calculated from pressure at point B by

$$\boldsymbol{p_C = p_B + \rho_{droplet} g h_{B-A} + \frac{\rho_{droplet} V^2}{2} = p_0 + \frac{2\gamma}{R} + \rho_{droplet} g h_{B-A} + \frac{\rho_{droplet} V^2}{2}} \quad \text{Eq. 5-3}$$

The stagnation pressure of $\boldsymbol{\rho_{droplet} g h_{B-A}}$ and the inertial item of $\frac{\rho_{droplet} V^2}{2}$ is reported to be negligible for water droplets. As a result, the pressure at point C can be simplified to

$$\boldsymbol{p_C = p_0 + \frac{2\gamma}{R}} \quad \text{Eq. 5-4}$$

Accordingly, the pressure at point D, which is also the *p(r,t)* in Eq. 5-1 can be expressed by

$$p_D = p_C + \frac{2\gamma}{R_{local}} = p_0 + \frac{2\gamma}{R} + \frac{2\gamma}{R_{local}} \quad \text{Eq. 5-5}$$

where the local radius R_{local} is twice of the inverse of local curvature. The curvature $\kappa(r,t)$ depends on the shape of the air film profile[17]:

$$\kappa(r,t) = \frac{\frac{\partial^2 h(r,t)}{\partial r^2}}{\left[1+\left(\frac{\partial h(r,t)}{\partial r}\right)^2\right]^{3/2}} + \frac{\frac{\partial h(r,t)}{\partial r}}{r\left[1+\left(\frac{\partial h(r,t)}{\partial r}\right)^2\right]^{1/2}} \quad \text{Eq. 5-6}$$

The radius of deformed part at the bottom is about 10% of the droplet original radius, so $\frac{\partial h(r,t)}{\partial r}$ is much smaller than 1. Eq. 5-6 can be simplified to:

$$\kappa(r,t) = \frac{\partial^2 h(r,t)}{\partial r^2} + \frac{1}{r}\frac{\partial h(r,t)}{\partial r} = \frac{1}{r}\frac{\partial}{\partial r}\left(r\frac{\partial h(r,t)}{\partial r}\right) \quad \text{Eq. 5-7}$$

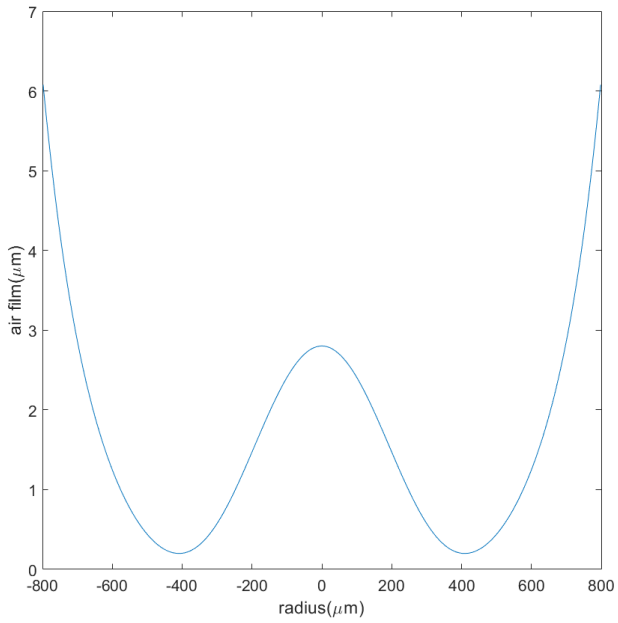

Figure 5-2. Numerical simulation of the impact of neutral droplet. Water droplet with impact velocity of 0.3m/s and diameter of 3.0mm.

Coupling Eq. 5-7 & 5-5, the air film pressure is expressed by

$$\boldsymbol{p(r,t) = p_0 + \frac{2\gamma}{R} + \frac{\gamma}{r}\frac{\partial}{\partial r}\left(r\frac{\partial h(r,t)}{\partial r}\right)} \qquad \text{Eq. 5-8}$$

Eq. 5-8 is solved to give the air film pressure $\boldsymbol{p(r,t)}$ that can be used in the cylinder form of the Reynolds lubrication equation Eq. 5-1 to time step the air film profile $\boldsymbol{h(r,t)}$ forward with the boundary condition of the initial impact velocity V_0.

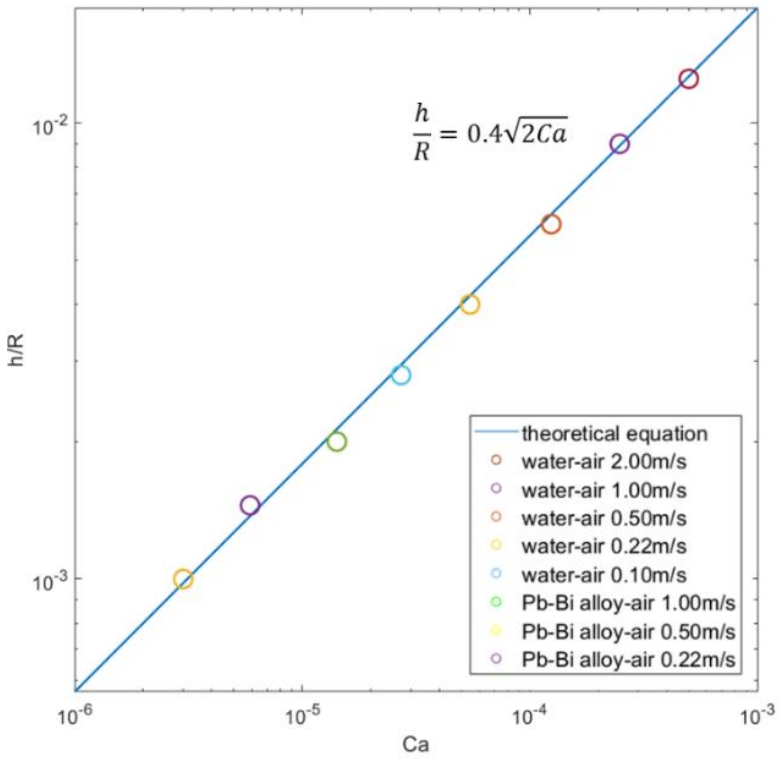

Figure 5-3. Comparison between numerical simulation with theoretical equations on neutral droplet deformation.

The simulation results are plotted in Fig. 5-2 as an example. The figures show that the thickness of air film is about 3μm for 3.0 mm diameter water droplet with 0.3m/s impact velocity.

The plots shown here are in agreement with previous work[126] and the experimental results in chapter 3. Fig.5-3 shows the simulated results of air film thickness with difference parameters. The figure indicates the numerical simulation shows agreement with theoretical equations in literature. [126]

5.3 Simulation of Charged Droplet Impact

The numerical simulation of neutral droplet impact has been introduced in Section 5.2, showing decent agreement with experiments. The main governing equation used is the Reynolds lubrication equation, with some assumptions and simplifications. For the charged droplet impacts on rigid the substrate, even though the air film profile looks different, the Reynolds lubrication (Eq. 5-1) still works, because there are nothing change in the air film.

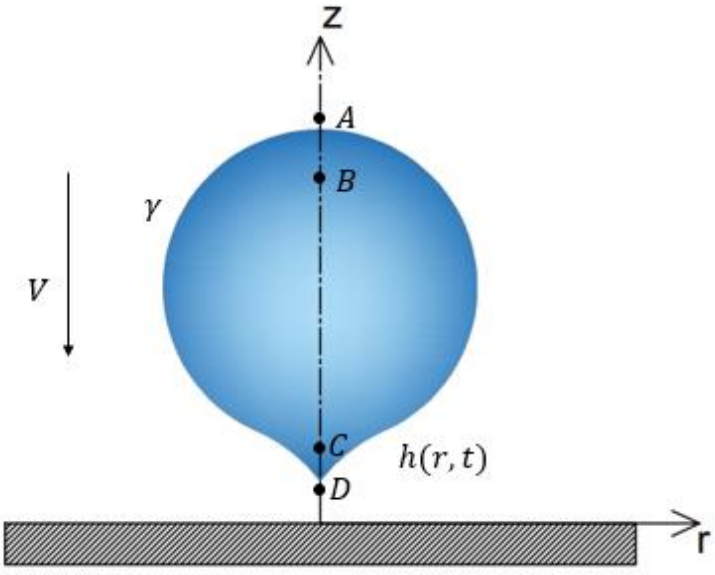

Figure 5-4. Schematic of the charged droplet impacting on a rigid flat surface.

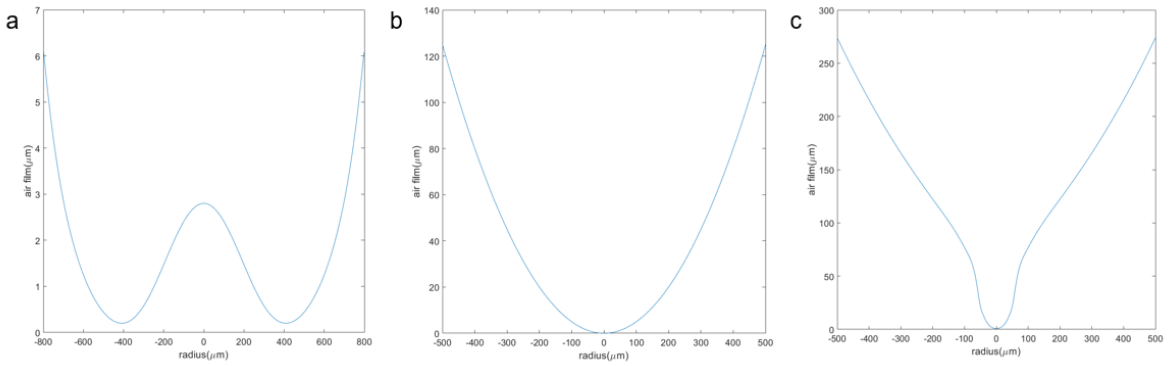

Figure 5-5. Three different types of droplet impact dynamics from numerical simulation. a) Charge level smaller than the critical charge level. b) Charge level equals to critical charge level. c) Charge level greater than critical charge level.

For the expression of $\boldsymbol{p(r,t)}$, the effect of Maxwell stress needs to be taken into consideration:

$$\boldsymbol{p(r,t) = p_0 + \frac{2\gamma}{R} + \frac{\gamma}{r}\frac{\partial}{\partial r}\left(r\frac{\partial h(r,t)}{\partial r}\right) + \tau_M} \qquad \text{Eq. 5-9}$$

where $\boldsymbol{\tau_M}$ is Maxwell stress. According to Eq. 3-3 & 3-4, for an perfect conductive sphere, the Maxwell stress can be expressed by

$$\boldsymbol{\tau_M = \frac{1}{2}\varepsilon E^2 = \frac{1}{32\varepsilon}\frac{q^2}{\pi^2 R^2 \delta^2}} \qquad \text{Eq. 5-10}$$

For an elastic conductive body, the charges will accumulate together in a small range to ensure the conductive boday a equipotential body. Eq. 5-10 should be rewritten into:

$$\boldsymbol{\tau_M = \frac{1}{2}\varepsilon E^2 = \frac{1}{32\varepsilon}\frac{q^2}{\pi^2 R_{local}^2 \delta^2}} \qquad \text{Eq. 5-11}$$

Hence, the air film pressure can be concluded to:

$$\boldsymbol{p(r,t) = p_0 + \frac{2\gamma}{R} + \frac{\gamma}{r}\frac{\partial}{\partial r}\left(r\frac{\partial h(r,t)}{\partial r}\right) + \frac{1}{128}\frac{q^2}{\pi^2\delta^2}\left(\frac{1}{r}\frac{\partial}{\partial r}\left(r\frac{\partial h(r,t)}{\partial r}\right)\right)^2} \qquad \text{Eq. 5-12}$$

Similar to neutral droplet impact, Eq. 5-12 is solved to give the air film pressure $\boldsymbol{p(r,t)}$ that can be used in Eq. 5-1 to time step the air film profile $\boldsymbol{h(r,t)}$ forward with the boundary condition of the initial impact velocity V_0.

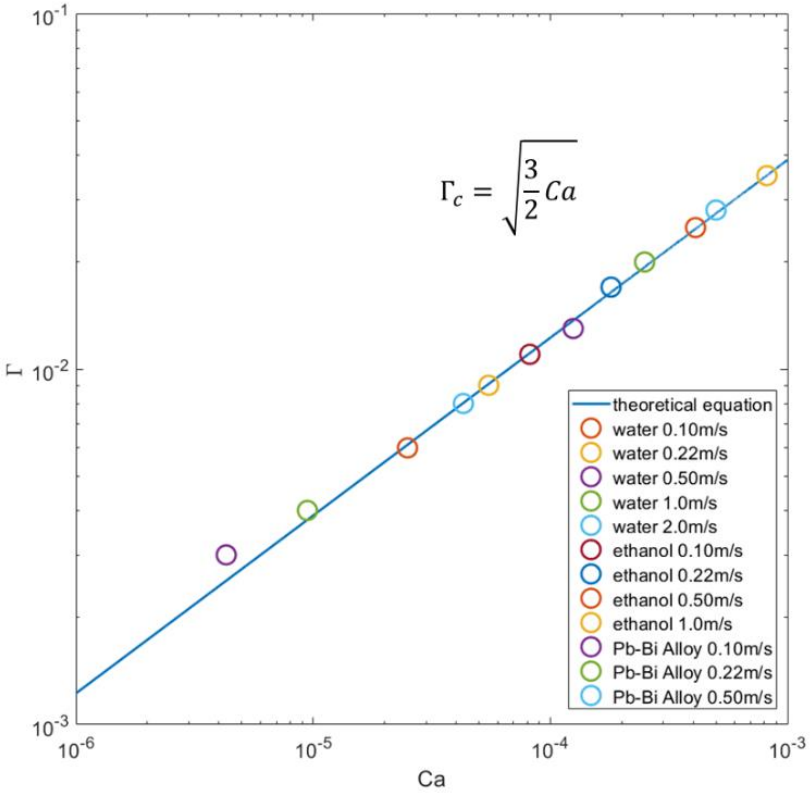

Figure 5-6. Comparison of the critical charge level predicted numerically and theoretically.

The simulation shows an obvious Taylor cone deformation as assumed when the droplet is charged with high charge level(Fig. 5-5), which numerically verify the theory in Chapter 3 that the Maxwell stress can totally alter the droplet deformation. Droplets with different charge levels can deform into different shapes. This shows agreement with the theory of ciritical charge level. In

experiments, droplet charged with critical charge level shows the transient status between convex lens shape deformation and cone shape deformation, with both light interference fringes and center wetting expansion together. In the numerical simulation, the transient status indicates the ideal situation that the droplet remains the initial shape during the whole impact process. To further verify the numerical model, repeated simulations with different liquids and different impact velocities were conducted to be compared with the equation of $\boldsymbol{\Gamma_c = \sqrt{3Ca_g/2}}$. As shown in Fig. 5-6, the numerical results show decent agreement with the critical charge level equation. This agreement verifies the theory that the competition between Maxwell stress and lubrication pressure results in the deformation of droplets during impact. The simulation also shows that once the Maxwell stress or lubrication pressure dominates the deformation, the deformation would further enhance the influence of the domination, causing more obvious deformation. The deformed droplet would stay in the same shape until touches the substrate.

5.4 Conclusions

In summary, a simplified numerical model was built based on the Reynolds lubrication equation. The numerical model only focuses on the air film profile under droplet. By using the model, the air film evolution of both neutral and charged droplet can be simulated. The simulation results show decent agreement with experiments, verifying the theory that weak charges can change the droplet impact dynamics. Moreover, this model can be used to anticipate air film development under some special conditions that are not easy to do experiments. Also, the numerical model can be modified to be utilized in other related thin film calculation and prediction.

Chapter 6 Summary and Outlook

6.1 Summary of Contributions

The goal of this dissertation is to investigate the impact dynamics of weakly charged droplets and the influence of droplet's charge level on the deformation. Experiments involving high-speed visualization is used for observing the droplet deformation, and a numerical model is built to simulate the process.

The first part of this dissertation focused on experimentally studying the impact dynamics of the weakly charged droplets. It was found that a weakly charged droplet could alter the gas film structure during the droplet impact on a flat surface. A critical charge level of about 1% of the Rayleigh limit was identified. If the charge level is greater than the critical value, the Maxwell stress will overcome the lubrication pressure to deform the droplet bottom surface in another way. The liquid cone results in a circular contact moving line that does not trap any gas. The critical charge level was also found only depend on the capillary number.

The second part of the dissertation continues to study the impact dynamics of a weakly charged droplet on dielectric surfaces and hydrophobic surfaces. It was discovered that weakly charged droplet could induce the polarization of dielectric surfaces, leading the droplet to deform into a conical shape. After touching the solid surface, due to the electric effect, wetting speed on the dielectric surfaces is faster than on the conductive surfaces. For hydrophobic surfaces, the weakly charged droplet was found to reduce the contact time. Under certain circumstances, the electric effect can even avoid the bouncing of droplets impacting on hydrophobic surfaces.

The last part of the dissertation is the numerical simulation of droplet impacts. A simplified model based on the Reynolds lubrication equation was developed. The impact of both neutral and charged droplet was successfully simulated. The numerical results are consistent with the results observed from experiments.

The main contributions of this dissertation include the followings:

- Discovered that sufficient charge level would alter gas film structure and eliminate air bubble. A concave shape air film ensures the droplet wetting starts from the center.
- Discovered that electrical effect can influence liquid metal droplet deformation during impact.
- Developed a mathematical model for the impact of charged droplet impact and developed an equation for computing a droplet's critical charge level; validating the model predictions experimentally.
- Discovered that droplet deformation on dielectric substrates is similar to that on conductive substrates because of polarization and derived mathematical model
- Discovered that electrical effect influences the contact time of droplet impacting a hydrophobic surface.
- Developed codes to numerically study the dynamics of neutral and charged droplets impacting solid substrates.

6.2 Outlook

In this dissertation, almost all experiments and analysis focus on the dynamics before the charged droplets touch flat smooth substrates. The electrical effect should also affect the dynamics after wetting. For example, one of the popular topics related to droplets is bouncing and splashing. The charge in droplet has been shown to affect the droplet bouncing on hydrophobic surfaces. It is reasonable to assume that the dynamics of splashing could also be significantly changed by the charge in the droplets.

There are also some open questions observed in experiments that need to be further studied. The wide air disk observed when Weber number is in the range of 2.0 to 3.0 is thought to be caused by force balance. However, the quasi-stationary air films still need a more thorough theoretical explanation to help better understand the physics governing these films.

One interesting issue is the cracking during solidification of droplets, which can have some applications in metal 3D printing. Even though the weakly charges could eliminate the air bubble, the cracks generated during solidification will ruin the entire printed sample. The mechanism behind the cracking can be complicated, partly because of the coupling between phase change, fluid flow, and mechanical deformation during the solidification process.

Another direction is more elaborate numerical simulations of droplet impact. The model used in the dissertation is relatively simple, with many simplifications and assumptions. This model can be enhanced to help understand similar cases related to a thin film of fluids. A more elaborate model can help to better understand the droplet impact dynamics.

References

1. Worthington, A.M., *XXVIII. On the forms assumed by drops of liquids falling vertically on a horizontal plate.* Proceedings of the Royal Society of London, 1877. **25**(171-178): p. 261-272.

2. Thoroddsen, S.T., T.G. Etoh, and K. Takehara, *High-speed imaging of drops and Bubbles.* Annual Review of Fluid Mechanics, 2008. **40**(1): p. 257-285.

3. Chen, X., S. Mandre, and J.J. Feng, *Partial coalescence between a drop and a liquid-liquid interface.* Physics of Fluids, 2006. **18**(5).

4. Xu, L., W.W. Zhang, and S.R. Nagel, *Drop splashing on a dry smooth surface.* Physical Review Letter, 2005. **94**(18): p. 184505.

5. Thoroddsen, S.T., T.G. Etoh, and K. Takehara, *Crown breakup by Marangoni instability.* Journal of Fluid Mechanics, 2006. **557**: p. 63-72.

6. Burton, J.C., R. Waldrep, and P. Taborek, *Scaling and instabilities in bubble pinch-off.* Physical Review Letters, 2005. **94**(18): p. 184502.

7. Thoroddsen, S.T., T.G. Etoh, and K. Takehara, *Experiments on bubble pinch-off.* Physics of Fluids, 2007. **19**(4): p. 042101.

8. Josserand, C., P. Ray, and S. Zaleski, *Droplet impact on a thin liquid film: anatomy of the splash.* Journal of Fluid Mechanics, 2016. **802**: p. 775-805.

9. Li, E.Q. and S.T. Thoroddsen, *Time-resolved imaging of a compressible air disc under a drop impacting on a solid surface.* Journal of Fluid Mechanics, 2015. **780**: p. 636-648.

10. Visser, C.W., et al., *Dynamics of high-speed micro-drop impact: numerical simulations and experiments at frame-to-frame times below 100 ns.* Soft Matter, 2015. **11**(9): p. 1708-1722.

11. Agbaglah, G., et al., *Parallel simulation of multiphase flows using octree adaptivity and the volume-of-fluid method.* Comptes Rendus Mécanique, 2011. **339**(2): p. 194-207.

12. Villermaux, E., *Fragmentation.* Annual Review of Fluid Mechanics, 2007. **39**(1): p. 419-446.

13. Yarin, A.L., *Drop impact dynamics: Splashing, spreading, receding, bouncing...* Annual Review of Fluid Mechanics, 2006. **38**(1): p. 159-192.

14. Josserand, C. and S.T. Thoroddsen, *Drop impact on a solid surface.* Annual Review of Fluid Mechanics, Vol 48, 2016. **48**(1): p. 365-391.

15. Lee, J.S., et al., *How does an air film evolve into a bubble during drop impact?* Physical Review Letters, 2012. **109**(20): p. 204501.

16. van der Veen, R.C., et al., *Direct measurements of air layer profiles under impacting droplets using high-speed color interferometry.* Physical Review E, 2012. **85**(2 Pt 2): p. 026315.

17. Bouwhuis, W., et al., *Maximal air bubble entrainment at liquid-drop impact.* Physical Review Letter, 2012. **109**(26): p. 264501.

18. de Ruiter, J., et al., *Dynamics of collapse of air films in drop impact.* Physical Review Letter, 2012. **108**(7): p. 074505.

19. de Ruiter, J., F. Mugele, and D. van den Ende, *Air cushioning in droplet impact. I. Dynamics of thin films studied by dual wavelength reflection interference microscopy.* Physics of Fluids, 2015. **27**(1).

20. Smith, F.T., L. Li, and G.X. Wu, *Air cushioning with a lubrication/inviscid balance.* Journal of Fluid Mechanics, 2003. **482**: p. 291-318.

21. Klaseboer, E., et al., *Film drainage between colliding drops at constant approach velocity: experiments and modeling.* Journal of Colloid and Interface Science, 2000. **229**(1): p. 274-285.

22. Riboux, G. and J.M. Gordillo, *Experiments of drops impacting a smooth solid surface: a model of the critical impact speed for drop splashing.* Physical Review Letter, 2014. **113**(2): p. 024507.

23. Bartolo, D., C. Josserand, and D. Bonn, *Retraction dynamics of aqueous drops upon impact on non-wetting surfaces.* Journal of Fluid Mechanics, 2005. **545**: p. 329-338.

24. Hicks, P.D., et al., *Air trapping at impact of a rigid sphere onto a liquid.* Journal of Fluid Mechanics, 2012. **695**: p. 310-320.

25. Marston, J.O., I.U. Vakarelski, and S.T. Thoroddsen, *Bubble entrapment during sphere impact onto quiescent liquid surfaces.* Journal of Fluid Mechanics, 2011. **680**: p. 660-670.

26. Chandra, S. and C. Avedisian, *On the collision of a droplet with a solid surface.* Proceedings of the Royal Society of London. Series A: Mathematical and Physical Sciences, 1991. **432**(1884): p. 13-41.

27. Pasandideh-Fard, M., et al., *Capillary effects during droplet impact on a solid surface.* Physics of Fluids, 1996. **8**(3): p. 650-659.

28. Range, K. and F. Feuillebois, *Influence of surface roughness on liquid drop impact.* Journal of Colloid and Interface Science, 1998. **203**(1): p. 16-30.

29. Rioboo, R., M. Marengo, and C. Tropea, *Time evolution of liquid drop impact onto solid, dry surfaces.* Experiments in Fluids, 2002. **33**(1): p. 112-124.

30. Roisman, I.V., R. Rioboo, and C. Tropea, *Normal impact of a liquid drop on a dry surface: model for spreading and receding.* Proceedings of the Royal Society of London. Series A: Mathematical, Physical and Engineering Sciences, 2002. **458**(2022): p. 1411-1430.

31. Clanet, C., et al., *Maximal deformation of an impacting drop.* Journal of Fluid Mechanics, 2004. **517**: p. 199-208.

32. Fedorchenko, A.I., A.-B. Wang, and Y.-H. Wang, *Effect of capillary and viscous forces on spreading of a liquid drop impinging on a solid surface.* Physics of Fluids, 2005. **17**(9): p. 093104.

33. Ukiwe, C. and D.Y. Kwok, *On the maximum spreading diameter of impacting droplets on well-prepared solid surfaces.* Langmuir, 2005. **21**(2): p. 666-673.

34. Roisman, I.V., E. Berberović, and C. Tropea, *Inertia dominated drop collisions. I. On the universal flow in the lamella.* Physics of Fluids, 2009. **21**(5): p. 052103.

35. Vadillo, D., et al., *Dynamic contact angle effects onto the maximum drop impact spreading on solid surfaces.* Physics of Fluids, 2009. **21**(12): p. 122002.

36. Eggers, J., et al., *Drop dynamics after impact on a solid wall: Theory and simulations.* Physics of Fluids, 2010. **22**(6): p. 062101.

37. Rioboo, R., C. Tropea, and M. Marengo, *Outcomes from a drop impact on solid surfaces.* Atomization and Sprays, 2001. **11**(2).

38. Bayer, I.S. and C.M. Megaridis, *Contact angle dynamics in droplets impacting on flat surfaces with different wetting characteristics.* Journal of Fluid Mechanics, 2006. **558**: p. 415-449.

39. Yokoi, K., et al., *Numerical studies of the influence of the dynamic contact angle on a droplet impacting on a dry surface.* Physics of Fluids, 2009. **21**(7): p. 072102.

40. Richard, D., C. Clanet, and D. Quéré, *Contact time of a bouncing drop.* Nature, 2002. **417**(6891): p. 811-811.

41. Bird, J.C., et al., *Reducing the contact time of a bouncing drop.* Nature, 2013. **503**: p. 385.

42. Stow, C.D., M.G. Hadfield, and J.M. Ziman, *An experimental investigation of fluid flow resulting from the impact of a water drop with an unyielding dry surface.* Proceedings of the Royal Society of London. A. Mathematical and Physical Sciences, 1981. **373**(1755): p. 419-441.

43. Mundo, C., M. Sommerfeld, and C. Tropea, *Droplet-wall collisions: Experimental studies of the deformation and breakup process.* International Journal of Multiphase Flow, 1995. **21**(2): p. 151-173.

44. Xu, L., W.W. Zhang, and S.R. Nagel, *Drop splashing on a dry smooth surface.* Physical Review Letters, 2005. **94**(18): p. 184505.

45. Tsai, P., et al., *Microscopic structure influencing macroscopic splash at high Weber number.* Soft Matter, 2011. **7**(24): p. 11325-11333.

46. Tsai, P., et al., *Drop impact upon micro- and nanostructured superhydrophobic surfaces.* Langmuir, 2009. **25**(20): p. 12293-12298.

47. Tsai, P., et al., *How micropatterns and air pressure affect splashing on surfaces.* Langmuir, 2010. **26**(20): p. 16090-16095.

48. Chou, F.-C., T.S. Zen, and K.-W. Lee, *An experimental study of a water droplet impacting on a rotating wafer.* Atomization and Sprays, 2009. **19**(10): p. 905-916.

49. Bird, J.C., S.S. Tsai, and H.A. Stone, *Inclined to splash: triggering and inhibiting a splash with tangential velocity.* New Journal of Physics, 2009. **11**(6): p. 063017.

50. Bouwhuis, W., et al., *Maximal air bubble entrainment at liquid-drop impact.* Physical Review Letters, 2012. **109**(26): p. 264501.

51. Mandre, S., M. Mani, and M.P. Brenner, *Precursors to splashing of liquid droplets on a solid surface.* Physical Review Letters, 2009. **102**(13): p. 134502.

52. Mani, M., S. Mandre, and M.P. Brenner, *Events before droplet splashing on a solid surface.* Journal of Fluid Mechanics, 2010. **647**: p. 163-185.

53. Hicks, P.D. and R. Purvis, *Air cushioning and bubble entrapment in three-dimensional droplet impacts.* Journal of Fluid Mechanics, 2010. **649**: p. 135-163.

54. Hicks, P.D. and R. Purvis, *Air cushioning in droplet impacts with liquid layers and other droplets.* Physics of Fluids, 2011. **23**(6): p. 062104.

55. Tran, T., et al., *Air entrainment during impact of droplets on liquid surfaces.* Journal of Fluid Mechanics, 2013. **726**: p. R3.

56. Castellanos, A., *Basic concepts and equations in electrohydrodynamics.* Courses and Lectures-International Centre for Mechanical Sciences, 1998. **1**(380): p. 1-82.

57. Castellanos, A., *Electrohydrodynamics*. Vol. 380. 2014: Springer.

58. Rayleigh, L., *XX. On the equilibrium of liquid conducting masses charged with electricity.* The London, Edinburgh, and Dublin Philosophical Magazine and Journal of Science, 1882. **14**(87): p. 184-186.

59. Gomez, A. and K. Tang, *Charge and fission of droplets in electrostatic sprays.* Physics of Fluids, 1994. **6**(1): p. 404-414.

60. Li, K.-Y., H. Tu, and A.K. Ray, *Charge limits on droplets during evaporation.* Langmuir, 2005. **21**(9): p. 3786-3794.

61. Novo, C. and P. Mulvaney, *Charge-induced Rayleigh instabilities in small gold rods.* Nano letters, 2007. **7**(2): p. 520-524.

62. Morad, M.R., et al., *A very stable high throughput Taylor cone-jet in electrohydrodynamics.* Scientific Reports, 2016. **6**: p. 38509.

63. J R Melcher, a. and G.I. Taylor, *Electrohydrodynamics: a review of the role of interfacial shear stresses.* Annual Review of Fluid Mechanics, 1969. **1**(1): p. 111-146.

64. Taylor, G.I., *Disintegration of water drops in an electric field.* Proceedings of the Royal Society of London. Series A. Mathematical and Physical Sciences, 1964. **280**(1382): p. 383-397.

65. Taylor, G.I., A.D. McEwan, and L.N.J.d. Jong, *Studies in electrohydrodynamics. I. The circulation produced in a drop by an electric field.* Proceedings of the Royal Society of London. Series A. Mathematical and Physical Sciences, 1966. **291**(1425): p. 159-166.

66. Cloupeau, M. and B. Prunet-Foch, *Electrostatic spraying of liquids in cone-jet mode.* Journal of Electrostatics, 1989. **22**(2): p. 135-159.

67. Collins, R.T., et al., *Electrohydrodynamic tip streaming and emission of charged drops from liquid cones.* Nat. Phys., 2007. **4**(2): p. 149-154.

68. Grimm, R.L. and J.L. Beauchamp, *Dynamics of field-induced droplet ionization: Time-resolved studies of sistortion, jetting, and progeny formation from charged and neutral*

methanol droplets exposed to strong electric fields. The Journal of Physical Chemistry B, 2005. **109**(16): p. 8244-8250.

69. Bird, J.C., et al., *Critical angle for electrically driven coalescence of two conical droplets.* Physical Review Letter, 2009. **103**(16): p. 164502.

70. Tipler, P.A. and G. Mosca, *Physics for scientists and engineers*. 2007: Macmillan.

71. Rapp, B.E., *Chapter 21 - Capillarity*, in *Microfluidics: Modelling, Mechanics and Mathematics*, B.E. Rapp, Editor. 2017, Elsevier: Oxford. p. 445-451.

72. Yarin, A. L., and D. A. Weiss. *Impact of drops on solid-surfaces-self-similar capillary waves and splashing as a new-type of kinematic discontinuity.* Journal of Fluid Mechanics, 1995. **283**(-1): p. 141.

73. Thoroddsen, S.T., T.G. Etoh, and K. Takehara, *Air entrapment under an impacting drop.* Journal of Fluid Mechanics, 2003. **478**.

74. Mehdi-Nejad, V., J. Mostaghimi, and S. Chandra, *Air bubble entrapment under an impacting droplet.* Physics of Fluids, 2003. **15**(1): p. 173-183.

75. Šikalo, Š., C. Tropea, and E. N. Ganić. *Impact of droplets onto inclined surfaces.* Journal of Colloid Interface Science, 2005. **286**(2): p. 661.

76. Tsai, P., et al., *How micropatterns and air pressure affect splashing on surfaces.* Langmuir, 2010. **26**(20): p. 16090-5.

77. Yi, H., et al., *Pinhole formation from liquid metal microdroplets impact on solid surfaces.* Applied Physics Letter, 2016. **108**(4).

78. Joung, Y.S., Z. Ge, and C.R. Buie, *Bioaerosol generation by raindrops on soil.* Nature Communication, 2017. **8**: p. 14668.

79. Wang, C.-H., et al., *Investigation of molten metal droplet deposition and solidification for 3D printing techniques.* Journal of Micromechanics and Microengineering, 2016. **26**(9).

80. Saleh, M.S., C. Hu, and R. Panat, *Three-dimensional microarchitected materials and devices using nanoparticle assembly by pointwise spatial printing.* Science Advances, 2017. **3**(3): p. e1601986.

81. DeMuth, P.C., et al., *Polymer multilayer tattooing for enhanced DNA vaccination.* Nature Materials, 2013. **12**(4): p. 367-76.

82. Krogman, K.C., et al., *Spraying asymmetry into functional membranes layer-by-layer.* Nature Materials, 2009. **8**(6): p. 512-8.

83. Smith, D.B., et al., *Droplet size and leaf morphology effects on pesticide spray deposition.* Transactions of the ASAE, 2000. **43**(2): p. 255-259.

84. Damak, M., et al., *Enhancing droplet deposition through in-situ precipitation.* Nature Communication, 2016. **7**: p. 12560.

85. Richard, D., C. Clanet, and D. Quéré, *Contact time of a bouncing drop.* Nature, 2002. **417**: p. 811.

86. Howland, C.J., et al., *It's harder to splash on soft solids.* Physical Review Letter, 2016. **117**(18): p. 184502.

87. Pepper, R.E., L. Courbin, and H.A. Stone, *Splashing on elastic membranes: The importance of early-time dynamics.* Physics of Fluids, 2008. **20**(8).

88. Liu, J., et al., *Splashing phenomena during liquid droplet impact.* Atomization and Sprays, 2010. **20**(4): p. 297-310.

89. Bird, J.C., S.S.H. Tsai, and H.A. Stone, *Inclined to splash: triggering and inhibiting a splash with tangential velocity.* New Journal of Physics, 2009. **11**(6).

90. Bartolo, D., C. Josserand, and D. Bonn, *Singular jets and bubbles in drop impact.* Physical Review Letter, 2006. **96**(12): p. 124501.

91. Hung, Y.-L., et al., *A study on the impact velocity and drop size for the occurrence of entrapped air bubbles – Water on parafilm.* Experimental Thermal and Fluid Science, 2013. **48**: p. 102-109.

92. Pittoni, P.G., et al., *Bubbles entrapment for drops impinging on polymer surfaces: The roughness effect.* Experimental Thermal and Fluid Science, 2015. **62**: p. 183-191.

93. Renardy, Y., et al., *Pyramidal and toroidal water drops after impact on a solid surface.* Journal of Fluid Mechanics, 2003. **484**: p. 69-83.

94. Jowkar, S. and M.R. Morad, *Rebounding suppression of droplet impact on hot surfaces: effect of surface temperature and concaveness.* Soft Matter, 2019. **15**(5): p. 1017-1026.

95. Che, Z. and O.K. Matar, *Impact of droplets on immiscible liquid films.* Soft Matter, 2018. **14**(9): p. 1540-1551.

96. Langley, K.R., et al., *The air entrapment under a drop impacting on a nano-rough surface.* Soft Matter, 2018. **14**(37): p. 7586-7596.

97. Thomson, S.W., *XVI. On a self-acting apparatus for multiplying and maintaining electric charges, with applications to illustrate the voltaic theory.* Proceedings of the Royal Society of London, 1868. **16**: p. 67-72.

98. Smith, L.G., *The electric charge of raindrops.* Quarterly Journal of the Royal Meteorological Society, 1955. **81**(347): p. 23-47.

99. Smith, F.T., L. Li, and G.X. Wu, *Air cushioning with a lubricationinviscid balance.* Journal of Fluid Mechanics, 2003. **482**: p. 291-318.

100. Mandre, S., M. Mani, and M.P. Brenner, *Precursors to splashing of liquid droplets on a solid surface.* Physical Review Letter, 2009. **102**(13): p. 134502.

101. Thoroddsen, S.T., et al., *The air bubble entrapped under a drop impacting on a solid surface.* Journal of Fluid Mechanics, 2005. **545**: p. 203–212.

102. Grimm, R.L. and J.L. Beauchamp, *Dynamics of field-induced droplet ionization: time-resolved studies of distortion, jetting, and progeny formation from charged and neutral methanol droplets exposed to strong electric fields.* The Journal of Physical Chemistry B, 2005. **109**(16): p. 8244-50.

103. Liu, Y., P. Tan, and L. Xu, *Kelvin-Helmholtz instability in an ultrathin air film causes drop splashing on smooth surfaces.* Proceedings of the National Academy of Sciences of the United States of America, 2015. **112**(11): p. 3280-4.

104. Zhang, G., et al., *Droplet impact dynamics on textiles.* Soft Matter, 2018. **14**(40): p. 8182-8190.

105. Xu, L., *Liquid drop splashing on smooth, rough, and textured surfaces.* Physical Review E, 2007. **75**(5): p. 056316.

106. Reyssat, M., et al., *Dynamical superhydrophobicity.* Faraday Discussions, 2010. **146**.

107. Tsai, P., et al., *Microscopic structure influencing macroscopic splash at high Weber number.* Soft Matter, 2011. **7**(24).

108. van der Veen, R.C., et al., *How microstructures affect air film dynamics prior to drop impact.* Soft Matter, 2014. **10**(21): p. 3703-7.

109. Achtzehn, T., et al., *The Coulomb instability of charged microdroplets: dynamics and scaling.* European Physical Journal D, 2005. **34**(1-3): p. 311-313.

110. Shahriari, A., et al., *Analysis of the instability underlying electrostatic suppression of the Leidenfrost state.* Physical Review Fluids, 2017. **2**(3).

111. Celestini, F. and G. Kirstetter, *Effect of an electric field on a Leidenfrost droplet.* Soft Matter, 2012. **8**(22).

112. Wildeman, S. and C. Sun, *Electric field makes Leidenfrost droplets take a leap.* Soft Matter, 2016. **12**(48): p. 9622-9632.

113. Shahriari, A., O. Ozkan, and V. Bahadur, *Electrostatic suppression of the Leidenfrost state on liquid substrates.* Langmuir, 2017. **33**(46): p. 13207-13213.

114. Ozkan, O., A. Shahriari, and V. Bahadur, *Electrostatic suppression of the Leidenfrost state using AC electric fields.* Applied Physics Letters, 2017. **111**(14).

115. Gao, F., et al., *Weakly charged droplets fundamentally change impact dynamics on flat surfaces.* Soft Matter, 2019. **15**(28): p. 5548-5553.

116. Gart, S., et al., *Droplet impacting a cantilever: A leaf-raindrop system.* Physical Review Applied, 2015. **3**(4): p. 044019.

117. Song, M., et al., *Controlling liquid splash on superhydrophobic surfaces by a vesicle surfactant.* Science Advances, 2017. **3**(3): p. e1602188.

118. Weisensee, P.B., et al., *Water droplet impact on elastic superhydrophobic surfaces.* Scientific Reports, 2016. **6**: p. 30328.

119. McHale, J.L., *Molecular spectroscopy*. 2017: CRC Press.

120. Kwon, S., et al., *Nonlinear dielectric ceramics and their applications to capacitors and tunable dielectrics.* IEEE Electrical Insulation Magazine, 2011. **27**(2): p. 43-55.

121. Pepper, R.E., L. Courbin, and H.A. Stone, *Splashing on elastic membranes: The importance of early-time dynamics.* Physics of Fluids, 2008. **20**(8): p. 082103.

122. Choi, M., G. Son, and W. Shim, *A level-set method for droplet impact and penetration into a porous medium.* Computers & Fluids, 2017. **145**: p. 153-166.

123. Patil, N.D., A. Sharma, and R. Bhardwaj. *Level set method based simulations on impact-dynamics of bouncing and non-bouncing droplet on super-hydrophobic substrates.* 2017. New Delhi: Springer India.

124. Hasan, M.N., A. Chandy, and J.-W. Choi, *Numerical analysis of post-impact droplet deformation for direct-print.* Engineering Applications of Computational Fluid Mechanics, 2015. **9**(1): p. 543-555.

125. Hong, W. and Y. Wang, *A coupled level set and volume-of-fluid simulation for heat transfer of the double droplet impact on a spherical liquid film.* Numerical Heat Transfer, Part B: Fundamentals, 2017. **71**(4): p. 359-371.

126. Klaseboer, E., R. Manica, and D.Y.C. Chan, *Universal behavior of the initial stage of drop impact.* Physical Review Letters, 2014. **113**(19): p. 194501.